DIFFRACTION WAVEFRONT ANALYSIS OF COMPUTER-GENERATED HOLOGRAMS

by

Yu-Chun Chang

A Dissertation Submitted to the Faculty of the

COMMITTEE ON OPTICAL SCIENCES (GRADUATE)

In Partial Fulfillment of the Requirements

For the Degree of

DOCTOR OF PHILOSOPHY

In the Graduate College

THE UNIVERSITY OF ARIZONA

1999

STATEMENT BY THE AUTHOR

This dissertation has been submitted in partial fulfillment of requirements for an advanced degree at The University of Arizona and is deposited in the University Library to be made available to borrowers under rules of the Library.

Brief quotations from this dissertation are allowable without special permission, provided that accurate acknowledgment of source is made. Requests for permission for extended quotation from or reproduction of this manuscript in whole or in part may be granted by the head of the major department or the Dean of the Graduate College when in his or her judgment the proposed use of the material is in the interests of scholarship. In all other instances, however, permission must be obtained from the author.

SIGNED:_________________________

ACKNOWLEDGEMENTS

This work has been supported in part by the Eastman Kodak Company project number: 98Z900031461. Special thanks go to Dr. Steve Arnold at Diffraction International for his technical support on grating sample making.

I would like to express my sincere gratitude to my advisor, Prof. Jim Burge, for introducing me into the exciting world of CGHs and optical metrology. Jim has been a terrific mentor as well as a friend. His guidance and support let the completion of this dissertation. Working with Jim has been a delightful experience; and I'm proud to be his first Ph.D. student. I am also grateful to the committee members, Prof. Jack Gaskill and Prof. Lifeng Li, for taking time reading my dissertation and providing valuable suggestions. I want to thank Jack for introducing Fourier optics to me. The knowledge I acquired from him has helped me tremulously during my research. Many thanks also go to Lifeng for his help on rigorous diffraction data simulation, which is the foundation of the theoretical analysis presented in the second half of my dissertation.

I want to thank my colleagues in the past and current: Dave Baiocchi, Tom Roberts, Roland Sarlot, Erin Sabatke, Brian Stamper, Gordon Tang and Chunyu Zhao, for their friendship and support.

Finally, I want to contribute my deepest appreciation to my parents, Dorothy and Ming-Wen, to my brothers, Kuan and Amos, and to my beloved soon-to-be husband, Tong, for their love and support over all these years. They have been a great influence of my life; and their constant encouragement and patience have let me pursue my dream.

To My Mother and Father

Dorothy & Ming-Wen Chang

TABLE OF CONTENTS

LIST OF FIGURES………………………………………………………...………..10

LIST OF TABLES………………………………………………………………...21

ABSTRACT……………………………………………………………………..22

1. INTRODUCTION…………………………………………………………….24

2. APPLICATION OF COMPUTER-GENERATED HOLOGRAMS IN OPTICAL TESTING……………………………………………………………29

2.1 Principles of Holography………………….……..………………………….29

2.1.1 Holographic Recording………………………………………..30

2.1.2 Wavefront Reconstruction…………………………………….33

2.2 Computer-Generated Holograms…………….…………………………..36

2.2.1 Computer-Generated Hologram: General Description…………..37

2.2.2 Different Types of CGHs………………...………………………39

2.2.3 Separation of Multiple Diffraction Orders……………………….47

2.3 CGH Fabrications……………………………….…………..………51

2.4 CGH Modeling Theory…….……………………………………………….55

2.5 Applications of Computer-Generated Holograms in Optical Testing………58

2.5.1 Optical Interferometric Systems…..………………..…………59

2.5.2 CGHs in Optical Testing………..……………………..……61

TABLE OF CONTENTS – *Continued*

3. WAVEFRONT PHASE ERRORS PRODUCED BY CGHS FABRICATION UNCERTAINTIES……………………………………………………………68

3.1 CGH Fabrication Errors……………….…………..…………………..69

3.2 Binary Linear Grating Model….………..………………………….…...70

3.2.1 Binary Linear Grating……………………………………………70

3.2.2 Diffraction Efficiency……………………………………………75

3.2.3 Wavefront Phase…………………………………………………76

3.3 Wavefront Phase Errors…………………………………………………….77

3.3.1 Substrate Figure Errors…………………..…..…………………...77

3.3.2 CGH Pattern Distortion……………………………………………..81

3.3.3 CGH Duty-Cycle Errors…………………………………………84

3.3.4 CGH Etching Depth Errors………………………………………85

3.4 Numerical Simulation of Phase Grating…………….………..…………..87

3.4.1 Diffraction Efficiency……………………………………………88

3.4.2 Wavefront Phase…………………………………………………91

3.5 Graphical Representation of Diffraction Fields...…………………………100

3.6 Numerical Simulation of Chrome-on-Glass Grating…………...…………105

3.6.1 Diffraction Efficiency…………………………………………..107

3.6.2 Wavefront Phase………………………………………………..109

TABLE OF CONTENTS – *Continued*

4. DIFFRACTION WAVEFRONT PHASE MEASUREMENTS OF BINARY GRATINGS……………………………………………………………..………118

4.1 Phase Grating……………….…………………………………………..119

4.1.1 Design of the Sample Phase Grating…………………….……..119

4.1.2 Procedure…………………………………………………….122

4.1.3 Results and Analysis………..…………………………………...125

4.2 Chrome-On-Glass Grating……..………..………………………………133

4.2.1 Design of the Sample Chrome-on-Glass Grating………………133

4.2.2 Procedure…………………………………………………….135

4.2.3 Results and Analysis……………………………………………135

5. EXAMPLES OF CGH ERROR ANALYSIS FOR OPTICAL TESTS………..145

5.1 Phase CGH…..……………..…………………………………………146

5.2 Chrome CGH..……………………………………………………..149

6. VALIDITY OF SCALAR DIFFRACTION MODEL IN CGH ANALYSIS….156

6.1 Rigorous Analysis of Grating Diffraction………………………………...157

6.2 Binary Linear Grating…………………..……………………………….162

6.3 Binary Zone Plate……………………..……………………………...167

6.3.1 Modeling Scheme……………………………………………168

6.3.2 Computer Simulation…………………………………………...172

TABLE OF CONTENTS – *Continued*

7. POLARIZATION SENSITIVITIES OF CGHS WITH ANNULAR RING PATTERNS……………………………………………………………………..180

7.1 Hologram Description……………………………………………………….180

7.2 Computer Simulation………………….……………….…………………...183

7.3 Experimental Procedures and Results……….……….…………………..186

7.3.1 Measurement Procedures……………..…..….………………….186

7.3.2 Experimental Results…………………...……………..……..187

8. DISCUSSIONS AND CONCLUSIONS……………………….…………………192

REFERENCES……………………………………………………………………...196

LIST OF FIGURES

Figure 2.1: Holographic recording process...…………………………………………….33

Figure 2.2: Wavefront reconstruction from a hologram. Reconstructing a virtual image of the object ……………………………………………………………...35

Figure 2.3: Wavefront reconstruction from a hologram. Reconstructing a real image of the object………………………..……………………………………..…35

Figure 2.4: CGH generation flow chart………………………………………….……38

Figure 2.5: Detour phase from unequally spaced grating slits…………………………..40

Figure 2.6: Detour phase hologram………………………………………………..…..41

Figure 2.7: Cell structure in a detour phase hologram……………….…………………41

Figure 2.8: Structure of a Fresnel lens…………………………………………………...44

Figure 2.9: Binary CGH encoding process………………………..…………………..46

Figure 2.10: A linear CGH with 1 λ Zernike spherical and 32 waves of tilt…………….48

Figure 2.11: Spot diagram showing multiple diffraction orders with orders overlapping.49

Figure 2.12: Wavefront aberration plot for +1 diffraction order…………..…………….50

Figure 2.13: Ray aberration plot for +1 diffraction order…………..……………………51

Figure 2.14: Schematic drawings show the processes of micro-lithography…………..…53

Figure 2.15: Geometry for Rayleigh-Sommerfeld diffraction integral……….…..……...56

LIST OF FIGURES - *Continued*

Figure 2.16: Schematic drawing of a Twyman-Green interferometer……………..…….60

Figure 2.17: Modified Twyman-Green interferometer for asphere testing using CGHs...63

Figure 2.18: Interferometer configuration with CGH in the reference arm ……………..64

Figure 2.19: Interferometer configuration with CGH in the test arm……………………65

Figure 2.20: Using CGHs as beam splitting elements…………………….………..…66

Figure 3.1: Surface relief profile of a binary grating…………………..………………71

Figure 3.2: Output complex wavefront function at the diffraction grating………………72

Figure 3.3: Spatial filtering using a 4-F configuration………………………………..74

Figure 3.4: Wavefront deviations due to substrate surface defects for both reflective and transmissive type holograms……………………………………………..78

Figure 3.5: 1-D grating profile with sinusoidal substrate figure errors………………….79

Figure 3.6: Schematic drawing of a linear diffraction grating…………………….…..82

Figure 3.7: Schematic drawing of a phase grating surface profile………………………87

Figure 3.8: Diffraction efficiency of phase grating as a function of grating duty-cycle and phase depth for zero-order diffraction beam…………………………..……88

Figure 3.9: Diffraction efficiency of a phase grating as a function of phase depth for the zero-order diffraction beam for nine duty-cycle values……………………89

Figure 3.10: Diffraction efficiency of a phase grating as a function of duty-cycle for the zero-order diffraction beam for five phase depth values………………….89

LIST OF FIGURES - *Continued*

Figure 3.11: Diffraction efficiency of a phase grating as a function of duty-cycle for non-zero order diffraction beams with 0.5λ phase depth……………….…..….…90

Figure 3.12: Diffraction efficiency of phase grating as a function of phase depth for non-zero order diffraction beams at 50% duty-cycle…………………....…..…91

Figure 3.13: Diffraction wavefront phase values of phase grating as a function of grating phase depth and duty-cycle for zero-order diffraction beam in 3-D coordinate……………………………………………………..…………92

Figure 3.14: Wavefront phase vs. phase depth for a phase grating in the zero diffraction order..………………………………………………………………..……93

Figure 3.15: Wavefront phase deviation of a phase grating to grating phase depth variation for the zero-order beam for various duty-cycle values…....…..…94

Figure 3.16: Phase depths and duty-cycle(s) combinations of phase gratings that are not sensitive to phase depth variations ($d\Psi_{m=0}/d\phi = 0$) for the zero-order beam..………………………….………………………………...…95

Figure 3.17: Diffraction efficiency values for phase gratings given in Figure 3.16 that are not sensitive to phase depth errors for the zero-order beam.……..……..….96

Figure 3.18: Wavefront phase vs. duty-cycle for the zero-order diffraction beam of a phase grating…………………..………………………………..……..…97

LIST OF FIGURES - *Continued*

Figure 3.19: Wavefront phase sensitivity of a phase grating to grating duty-cycle variation for the zero-order beam for various phase depth values......….…97

Figure 3.20: Wavefront phase vs. grating phase depth for the 1st-order and the 2nd-order diffraction beam for all grating duty-cycle values from phase grating.……98

Figure 3.21: Wavefront phase vs. grating duty-cycle for non-zero diffraction orders at 0.5 waves phase depth from phase grating.……..…………..…………………99

Figure 3.22: Graphical representation of the complex diffraction wavefront produced by a phase grating with 40% duty-cycle for the zero-order beam……………..101

Figure 3.23: Graphical representation of the complex diffraction fields in the zero diffraction order produced by a phase grating with nine duty-cycle values……………………………………………………………………. 102

Figure 3.24: Graphical representation of the complex diffraction fields in the zero diffraction order produced by a phase grating with 50% duty-cycle…..…103

Figure 3.25: Graphical representation of the complex diffraction fields at various diffraction orders for gratings with different duty-cycles..………...……..104

Figure 3.26: 3-D complex diffraction fields illustration of Figure 3.25. (from left to right: D = 60%, 50% and 40%)...……………………………………...……..105

Figure 3.27: Schematic drawing of a chrome-on-glass grating………………………...106

Figure 3.28: Reflectance amplitude and phase functions calculated for multi-reflection beams from a thin chrome coating at different thickness……………..…107

LIST OF FIGURES - *Continued*

Figure 3.29: Diffraction efficiency for zero-order beam vs. duty-cycle for chrome-on-glass gratings with different chrome thicknesses…………………..……..108

Figure 3.30: Diffraction efficiency for zero-order beam vs. chrome thickness for chrome-on-glass gratings at various grating duty-cycles……………..…………...108

Figure 3.31: Diffraction efficiency for non-zero diffraction orders vs. duty-cycle for a chrome-on-glass grating with 80 nm chrome thickness.....………………109

Figure 3.32: Wavefront phase for the zero-order beam vs. duty-cycle and chrome thickness for chrome-on-glass gratings …..……………….……...…...110

Figure 3.33: Wavefront phase for the zero-order beam vs. duty-cycle for chrome-on-glass gratings with different chrome thicknesses…..……………………………110

Figure 3.34: Wavefront phase for the zero-order beam vs. chrome thickness for chrome-on-glass gratings with various duty-cycles…...…………………………...111

Figure 3.35: Wavefront phase sensitivity function to 1% duty-cycle variation in the zero-order beam for chrome-on-glass gratings...…..………...….……………..112

Figure 3.36: Wavefront phase sensitivity function to 1 nm chrome thickness variations for chrome-on-glass gratings in the zero-order beam …………………....113

Figure 3.37: Wavefront phase sensitivity function for chrome-on-glass gratings with difference chrome thickness per 1% line width variation from the nominal value in the zero-order beam…………………………………………...114

LIST OF FIGURES - *Continued*

Figure 3.38: Wavefront phase vs. chrome thickness for the 1st-order and 2nd-order diffraction beams for all duty-cycle from chrome-on-glass gratings…......115

Figure 3.39: Wavefront phase vs. grating duty-cycle for non-zero diffraction orders for chrome-on-glass gratings with 100 nm chrome thickness…………..…...116

Figure 4.1: Design layout of the sample phase grating. It is a 5 by 11 array where each cell in the array contains a linear grating……………………………..…...120

Figure 4.2: An enlarged top view of a small area on the sample grating array. Duty-cycle varies along the row direction of the grating……………………….…………...121

Figure 4.3: Cross-section view of the column #3 (50% duty-cycle) of the sample grating array. Groove depth varies along the column direction………….….....121

Figure 4.4: Sample grating array engraved on a glass substrate……………..………121

Figure 4.5: Experimental setup for sample gratings wavefronts measurements…….....122

Figure 4.6: Interferograms obtained for the sample phase grating the zero-order. (Note the phase shift around the center of the pattern)…………………………..123

Figure 4.7: Measured zero-order wavefront phase map of the sample phase grating with tilt, power and astigmatism removed……………………………….…..….124

Figure 4.8: Phase profile plots of the sample grating array with surrounding Cr coated glass substrate ………………………………………………………...125

LIST OF FIGURES - *Continued*

Figure 4.9: Diffraction wavefront phase deviations per grating etching depth variation for the zero-order beam of the sample phase grating. Experimental data vs. Theoretical results……………………..……………………………………127

Figure 4.10: Diffraction wavefront phase deviations per grating duty-cycle variation for the zero-order beam of the sample phase grating. Experimental data vs. Theoretical results …………………..………………………………..…..…...129

Figure 4.11: Wavefront phase sensitivity functions per phase depth variations for the 1st order diffraction wavefront of the sample phase grating. Experimental data (vertical line) vs. Theoretical data (solid line)……………………..……..131

Figure 4.12: Wavefront phase sensitivity functions per 1% duty-cycle variations for the 1st order diffraction wavefront of the sample phase grating. Experimental data (vertical bars) vs. Theoretical data (solid line)………………………132

Figure 4.13: Design layout of the sample chrome-on-glass grating……………………133

Figure 4.14: Microscope image of a small area on the sample chrome-on-glass grating with 50 um grating period and duty-cycle varied from 40% to 50%…......134

Figure 4.15: Interferogram obtained from the sample chrome-on-glass grating……….136

Figure 4.16: Measured index of refraction curves for chromium using ellipsometer….137

Figure 4.17: Wavefront phase sensitivity functions per 1% duty-cycle variations for the zero order diffraction wavefront for the sample chrome-on-glass grating. Experimental data (vertical bars) vs. Theoretical data (solid line)……….138

LIST OF FIGURES - *Continued*

Figure 4.18: Wavefront phase sensitivity functions per 1% duty-cycle variations for the 1st order diffraction wavefront for the sample chrome-on-glass grating. Experimental data (vertical bars) vs. Theoretical data (solid line)….……139

Figure 4.19: Interferogram indicating diffraction efficiency distribution and wavefront phase as a function of grating duty-cycle at different diffraction orders. Top chart shows the corresponding theoretical values ………………………..142

Figure 5.1: Asphere metrology using a Fizeau interferometer with a phase CGH……..146

Figure 5.2: Asphere metrology setup using Fizeau interferometer with a chrome-on-glass CGH……………………………………………….…………………..149

Figure 5.3: Schematic drawing shows the constructions of the test and the reference wavefronts…..…………………………………….……………………...150

Figure 5.4: CGH surface figure measurement………………..……………………...154

Figure 6.1: Geometry of the grating diffraction problem………………………………159

Figure 6.2: Schematic drawing of the geometry of a chrome-on-glass grating………...162

Figure 6.3: Phase values as a function of grating period for both the TE and the TM fields for a chrome-on-glass grating with 50% duty-cycle and 0.15λ chrome thickness ……………………………………………………………..164

LIST OF FIGURES - *Continued*

Figure 6.4: Phase differences between the TE and the TM fields as a function of grating period for a chrome-on-glass grating with 50% duty-cycle and 0.15λ chrome thickness…………………………………………………………...164

Figure 6.5: Diffraction efficiency as a function of grating period for both the TE and the TM fields for a chrome-on-glass grating with 50% duty-cycle and 0.15λ chrome thickness……………………………………………………165

Figure 6.6: Phase differences between the TE and TM fields as a function of grating period for a chrome-on-glass grating with 0.15l chrome thickness at different duty-cycles……..…………………………………………………………166

Figure 6.7: Phase difference between the TE and the TM fields as a function of grating period for a chrome-on-glass grating with 50% duty-cycle at different chrome thicknesses….………………………………………...……...166

Figure 6.8: A binary zone plate………………………………………………………169

Figure 6.9: Linear grating rotated by an angle θ respected to the y-axis of the zone plate…………………………………………………………………..171

Figure 6.10: Ring spacing vs. ring radius for zone plate used in the first order……..…173

Figure 6.11: Inverse ring spacing vs. ring radius for zone plate used in the first order...173

Figure 6.12: Calculated wavefront phase and diffraction efficiency function for the TE polarization wavefront with TE polarized incident field……………..…..174

LIST OF FIGURES - *Continued*

Figure 6.13: Calculated wavefront phase and diffraction efficiency function for the TM polarized wavefront with TE polarized incident field………….………..175

Figure 6.14: Profile plots of the calculated wavefront phase function for the TE polarization wavefront with TE polarized incident field..……………..….175

Figure 6.15: Profile plots of the calculated diffraction efficiency function for the TE polarization wavefront with TE polarized incident field…………………176

Figure 6.16: Calculated wavefront phase and diffraction efficiency function for the TM polarization wavefront with TM polarization incident field……………...176

Figure 6.17: Calculated wavefront phase difference between the TE and the TM polarization wavefronts……….……………………………………….……177

Figure 6.18: Profile plots of the calculated phase differences between the TE and the TM polarization wavefronts……..……………………………………………178

Figure 7.1: Direct beam writing process using thermo-chemical reaction……………..181

Figure 7.2: Surface profiles of the central area of the hologram……………….……...182

Figure 7.3: Ring spacing vs. ring radius of the hologram………………………………183

Figure 7.4: Calculated phase maps for incident beam in (a) TE mode and (b) TM mode…………………………………………………………………….184

Figure 7.5: Profile plots of phase map produced by TE incident beam………………...185

Figure 7.6: Phase difference between TE and TM fields……………………………….185

Figure 7.7: Phase difference profiles…………………………………………………...186

LIST OF FIGURES - *Continued*

Figure 7.8: Experimental setup for CGH polarization sensitivity measurement……….187

Figure 7.9: Contour plot of the diffracted wavefront for the sample CGH with TE polarized incident field…………………………………………………188

Figure 7.10: Contour plot of the diffracted wavefront for the sample CGH with TM polarized incident field…..…………………………………………….188

Figure 7.11: Wavefront phase difference map between TE and TM polarization fields……………………………………………………………………189

Figure 7.12: Phase difference map after removing tilt, power, and 3rd order spherical...189

Figure 7.13: Phase difference map after low pass filtering ……………………………190

Figure 7.14: 3-D plot of the final wavefront phase difference map…………………….190

LIST OF TABLES

Table 5.1: Phase CGH structure parameters……………………………………………147

Table 5.2: Diffraction wavefront phase errors from CGH fabrication uncertainties…...147

Table 5.3: Chrome-on-glass CGH structure parameters………………………………..151

Table 5.4: Diffraction wavefront phase errors from CGH fabrication uncertainties…...152

Table 5.5: Wavefront phase errors for CGH surface figure measurement……………..154

ABSTRACT

Computer-generated holograms (CGHs) use diffraction to create wavefronts of light with desired amplitude and phase variations. The amplitdue control is well known. But the sensitivity of phase, which is most important for some applications, such as interferometry, is less known. This dissertation studies phase errors resulted from design and fabrication limitations of CGHs.

Fabrication uncertainties of CGHs are primarily responsible for the degradation of the quality of wavefronts generated by CGHs. In this dissertation, the binary linear diffraction model is introduced to study wavefront phase errors caused by substrate figure errors, pattern distortion, grating duty-cycle and etching depth errors. Wavefront sensitivity functions derived from diffraction model provide analytical solutions to estimate phase deviations due to duty-cycle or phase depth variations. The results of the wavefront sensitivity analysis also enable us to identify hologram structures that are the most sensitive, as well as the least sensitive to fabrication uncertainties. Experiments were conducted to validate the diffraction model. Example error budgets for common CGH optical testing configurations are demonstrated. In addition, a graphical representation of the diffraction fields is introduced. It provides an intuitive way for

diffraction wavefront analysis and explains phase discontinuous observed in the diffraction model.

Scalar diffraction models are commonly used in CGH analysis and modeling due to their computational simplicity compared with rigorous diffraction models. The validity of the scalar diffraction models becomes unclear when they are used to analyze diffractive elements with wavelength-scaled features. This dissertation discusses the validity of the scalar diffraction models with giving emphasis to wavefront phase. Fourier modal method (FMM) derived from rigorous diffraction theory is used to study a binary zone plate. The result of this analysis is compared with experimental data. This study shows that polarization sensitivities of the hologram are almost negligible for the chrome-on-glass zone plate with a minimum ring spacing of 2λ. This result implies that scalar diffraction models may still be sufficient for modeling the phase from holograms with wavelength-scaled diffraction features for the case studied in this dissertation.

CHAPTER 1

INTRODUCTION

Computer-generated holograms (CGHs) are diffractive optical elements synthesized with the aid of computers, and they are capable of producing optical wavefronts with any desired shape. The high degree of flexibility in generating complex wavefronts has made computer-generated holograms extremely useful. CGHs are employed in many fields including optical data storage, laser scanning, image processing and optical testing.

In the field of optical testing and metrology, CGHs are often used in optical interferometric systems to produce reference wavefronts. The application of CGHs in optical interferometry allows complex non-spherical surfaces to be measured easily without using expensive reference surfaces or null lenses. Errors in CGHs, however, result in phase errors in the diffracted wavefront. This wavefront phase error directly affects the accuracy and validity of the interferometric measurements. Therefore, abilities to predict and correct these phase errors are essential for the applications of CGHs in optical testing.

Much research has been conducted to improve design schemes and fabrication techniques for CGHs. The majority of the work, however, has been directed toward optimizing diffraction efficiencies of the holograms. Despite the fact that wavefront phase is of most concern in optical testing, few papers have touched upon the topic of sensitivity of the diffracted phase to fabrication errors.

This dissertation addresses effects of both design and fabrication limitations on diffraction wavefront phase generated by computer-generated holograms. Both scalar diffraction models and rigorous diffraction models are reviewed. The limitations and validity of the widely employed scalar diffraction model are investigated. CGH fabrication errors and their effects on diffraction wavefront phase and efficiency functions also are studied. CGH pattern errors, especially duty-cycle and groove depth errors, are investigated in detail. Both analytical and experimental results of the studies are presented. In addition, a graphical representation of diffraction fields is introduced.

The goal of this dissertation is to obtain a thorough understanding of both the design and fabrication aspects of the computer-generated holograms. The results of this research provide guidance to the future design, analysis and fabrication of CGHs, especially in the field of optical testing and interferometry. The wavefront sensitivity analysis provides insights of CGH fabrication errors; it is a powerful reference to the error analysis and error budgeting for future CGH applications. Using the wavefront sensitivity functions, we are able to identify hologram structures that are the most sensitive, as well as, the least sensitive, to fabrication uncertainties. This information may also be used to obtain CGH designs that will reduce or eliminate effects of fabrication errors. The graphical representation provides an intuitive way for diffraction fields analysis; diffraction amplitude and phase values can be easily retrieved for complex field plot. The results from wavefront polarization sensitivity measurement implies that scalar diffraction model may still be sufficient for modeling CGHs with wavelength-scaled features.

The dissertation begins by providing an overview of the history of computer-generated holograms. Chapter 2 reviews basic principles of both conventional holography and computer-generated holography. Modern fabrication techniques for CGHs are also described. A review of optical interferometry leads to a discussion of the application of CGHs in the field of optical testing and metrology.

Fabrication errors degrade the accuracy of wavefronts created by CGHs, and uncertainties in the manufacturing processes result in errors in the finished hologram. Sensitivities of the diffracted wavefront phase function to CGH fabrication errors are studied in Chapter 3 and Chapter 4. A binary linear grating model is introduced to analyze wavefront phase dependence on CGH groove depth and duty-cycle variations in

Chapter 3. Analytical solutions for diffraction efficiency, diffracted wavefront phase functions and wavefront sensitivity functions are derived. These results are used to analyze the performance of phase gratings and chrome-on-glass gratings. In addition, a graphical representation of diffraction fields is introduced. The graphical representation provide an intuitive

The experimental results are compared with theoretical predictions in Chapter 4. A phase grating and a chrome-on-glass grating are fabricated with various groove depths and duty-cycles. Both gratings are measured using a phase shifting interferometer. The measured wavefront phase functions are used to determine their sensitivities to grating groove depth and duty-cycle variations.

To illustrate how to use the results of CGH fabrication error analysis in practical optical testing problems, two examples are given in Chapter 5. Typical CGH fabrication errors such as substrate figure errors, pattern distortions, duty-cycle and phase depth variations are considered in the analysis. Total wavefront errors from the two CGHs produced by fabrication tolerances and uncertainties are estimated from the root-sum-squared (RSS) of all error sources. The calculated wavefront errors are used to estimate errors for both interferometric measurements.

Limitations of the scalar diffraction models for hologram analysis are discussed in Chapter 6 and Chapter 7. Rigorous diffraction theory is introduced at the beginning of

Chapter 6. Fourier modal method derived from the rigorous diffraction theory is used to analyze diffractive elements with wavelength-scaled features. Linear grating models are used to analyze diffraction wavefront sensitivities to the state of polarization of the incident field. Numerical solutions obtained from the linear grating models are then used to simulate the performance of a binary zone plate with wavelength-scaled features.

In Chapter 7, a sample chrome-on-glass zone plate is fabricated and measured with both TE and TM polarized incident fields using a phase shifting interferometer. The measured wavefront phase functions are used to determine the polarization sensitivity of the zone plate. Experimental results are compared with computer simulation data at the end of the chapter. The results suggest that the scalar diffraction model may still be sufficient for modeling diffracted phase of CGH with minimum of 2λ features sizes.

Finally, we conclude the results of this research in Chapter 8. Reviews and discussion of some of the important findings are given. Suggestions to future research in this area are also provided.

CHAPTER 2

APPLICATIONS OF COMPUTER-GENERATED HOLOGRAMS IN OPTICAL TESTING

In this chapter, the principles and history of holography are briefly reviewed. Holographic recording, wavefront reconstruction and hologram fabrication processes are described. Computer-generated holography and its advantages over conventional holographic recording methods are reviewed. Different types of hologram encoding techniques and CGH fabrication methods using optical and e-beam lithography are presented. A detail discussion on the applications of computer-generated holograms in the field of optical interferometry is given at the end.

2.1. PRINCIPLES OF HOLOGRAPHY

Conventional photographic recording process records intensity variations of the subjects. A photograph contains only the amplitude information of the original incident wavefront. Phase information of the object beam is lost because of the incoherent nature of the incident wave and time averaging.

In order to preserve both amplitude and phase information of the recorded wavefront, a different recording technique was invented. To distinguish this technique from conventional photography, it was named ‘holography’, where in Greek ‘holo’ means ‘total’. Photographs produced using the means of holography are called holograms. A hologram contains the ‘entire message’, both the amplitude and the phase information, of the incident wavefronts. In addition, a hologram can be used to completely reconstruct the recorded wavefront in a later time. In short, holography provides a way of recording and reconstructing complete wavefront information. Loomis gave an interesting comparison of conventional photography and holography; he said, “If photography is compared to the art of painting, then holography can be compared to the art of sculpture.” **[Loomis 1980]**

2.1.1. Holographic Recording

Holograms may be recorded on the same type of media used for conventional photography, which respond only to the intensity variations of the incident light. In order to store wavefront phase information onto this medium, a way of converting wavefront phase variations into intensity variations is necessary. In holography, this task is accomplished through the phenomena of optical interference.

Optical interference occurs when two mutually coherent wavefronts intersect in space. Amplitude functions of the two wavefronts add or subtract depending on the phase difference between the two. The result of this interaction is a set of alternating bright and dark fringes, which are called interference fringes or an interferogram **[Born and Wolf 1980; Hecht 1987]**. Bright fringes are produced when the phase difference between the two interacting wavefront is a multiple of 2π. Dark fringes are the results of π phase difference. An interferogram can be interpreted as a map of constant phase difference between the two interfering wavefronts. Through interference, wavefront phase functions are encoded and transformed into the form of intensity variations.

Holographic recording processes can be demonstrated through a set of mathematical equations. Different from photography, a reference beam is needed for the holographic recording. Besides, the object wavefront and the reference wavefront must be mutually coherent. The interference pattern between the reference and the object wavefront is recorded as a hologram.

In Equation (2.1) and (2.2), a reference and an object wavefront are expressed as products of a real amplitude function and a phase factor. With the presumption of temporal coherency between the two wavefronts, the time harmonic factor $e^{-i\omega t}$ for both beams are suppressed in the expressions:

$$R(x,y) = R_0(x,y) \cdot e^{i\varphi(x,y)} \tag{2.1}$$

$$O(x,y) = O_0(x,y) \cdot e^{i\phi(x,y)} \tag{2.2}$$

To further simplify the derivation, the reference wavefront is chosen to be a plane wave with a constant amplitude function,

$$R(x,y) = R_0 \cdot e^{i\varphi(x,y)} \tag{2.3}$$

Interference pattern produced from the interference between the object and the reference wavefronts is then:

$$\begin{aligned} I(x,y) &= \left|R(x,y) + O(x,y)\right|^2 \\ &= \left|R(x,y)\right|^2 + \left|O(x,y)\right|^2 + R(x,y) \cdot O^*(x,y) + R^*(x,y) \cdot O(x,y) \end{aligned} \tag{2.4}$$

and $$I(x,y) = R_0^2 + O_0^2(x,y) + 2 \cdot R_0 \cdot O_o(x,y) \cdot \cos\left[\phi(x,y) - \varphi(x,y)\right] \tag{2.5}$$

The first two terms in Equation (2.5) are intensity values that are related to the amplitude functions of the object and the reference beams. It is the last term in the equation that gives the spatial modulation of the recorded intensity, which is a function of the phase difference between the object and the reference wavefronts.

A hologram is obtained by recording this intensity function (Equation 2.5) onto a photographic plate (see Figure 2.1). The exposed photographic plate, in turn, will have a transmittance function (T) that is proportional to the recorded intensity function (Equation 2.6).

$$\begin{aligned} &T(x,y) \propto I(x,y) \\ &T(x,y) \propto R_0^2 + O_0^2(x,y) + 2 \cdot R_0 \cdot O_o(x,y) \cdot \cos\left[\phi(x,y) - \varphi(x,y)\right] \end{aligned} \tag{2.6}$$

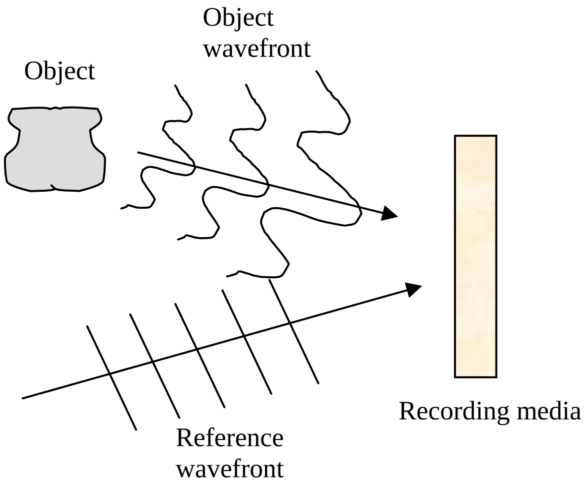

Figure 2.1. Holographic recording process.

2.1.2. Wavefront Reconstruction

The original object wavefront used during the holographic recording process can also be completely reconstructed from the recorded hologram. This is done by illuminating the hologram with a reconstructing beam C(x,y). The transmitted wavefront N(x,y) through a transmission hologram is amplitude modulated by the transmittance function of the hologram, which is described by Equation (2.6). The output wavefront function is then:

$$\begin{aligned} N(x,y) &\propto C(x,y)\cdot T(x,y) \\ &= C(x,y)\cdot R_0^2 + C(x,y)\cdot O_0^2(x,y) \\ &\quad + C(x,y)\cdot R(x,y)\cdot O^*(x,y) + C(x,y)\cdot R^*(x,y)\cdot O(x,y) \end{aligned} \tag{2.7}$$

or

$$N(x,y) \propto U_1 + U_2 + U_3 + U_4 \tag{2.8}$$

where:

$$
\begin{aligned}
U_1 &= C(x,y)\cdot R_0^2 \\
U_2 &= C(x,y)\cdot O_0^2(x,y) \\
U_3 &= C(x,y)\cdot R(x,y)\cdot O^*(x,y) \\
U_4 &= C(x,y)\cdot R^*(x,y)\cdot O(x,y)
\end{aligned}
\tag{2.9}
$$

It can be seen from Equation (2.7) that a hologram behaves just like a diffraction grating; and multiple diffractive orders may be produced. The reconstructed wavefronts from a hologram can be separated into three parts: the first two terms U_1 and U_2 represent the zero diffraction order; while the +1 and –1 diffraction orders are described by U_3 and U_4 respectively (Equation 2.8).

When the reconstruction wavefront C(x,y) is made identical to the reference wavefront R(x,y) used during the holographic recording process, U_4 becomes:

$$
\begin{aligned}
U_4 &= C(x,y)\cdot R^*(x,y)\cdot O(x,y) \\
&= R(x,y)\cdot R^*(x,y)\cdot O(x,y) \\
&= R_0^2\cdot O(x,y)
\end{aligned}
\tag{2.10}
$$

In this case, the original object wavefront O(x,y) is completely reproduced with a constant amplitude factor R_0^2. The reconstructed wavefront diverges from the position of the original object; and a virtual image of the object is formed (Figure 2.2).

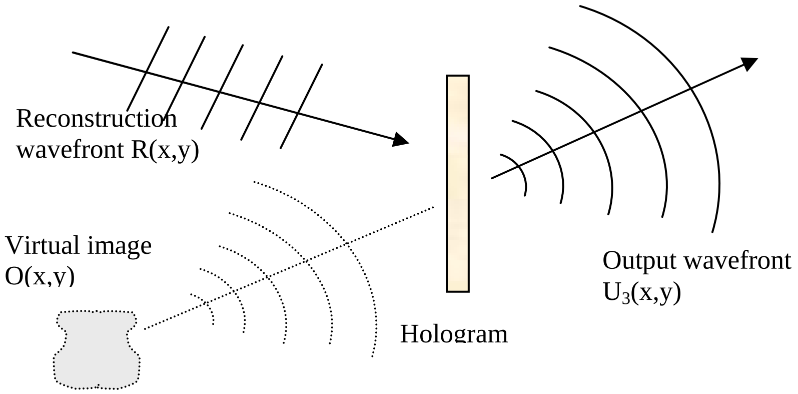

Figure 2.2. Wavefront reconstruction from a hologram. Reconstructing a virtual image of the object

When the reconstruction wavefront C(x,y) is made conjugate to the reference wavefront R(x,y), U_3 becomes:

$$\begin{aligned} U_3 &= C(x,y)\cdot R(x,y)\cdot O^*(x,y) \\ &= R^*(x,y)\cdot R(x,y)\cdot O^*(x,y) \\ &= R_0^2\cdot O^*(x,y) \end{aligned} \tag{2.11}$$

In this case, wavefront that is conjugate to the original object wavefront is produced. This reconstructed wavefront converges to the position of the original object. A real image of the object may be observed (Figure 2.3) under this condition.

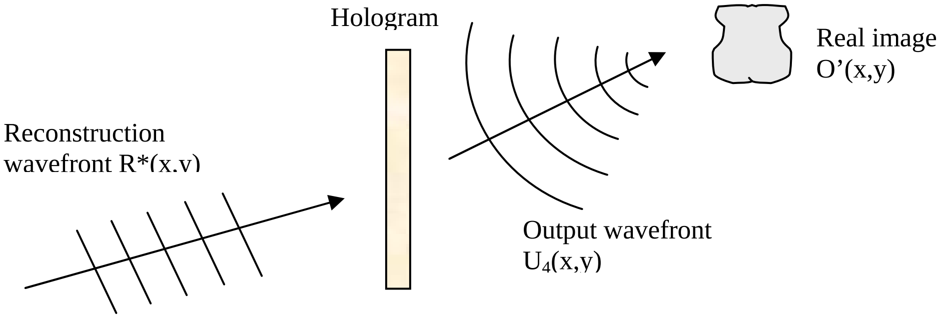

Figure 2.3. Wavefront reconstruction from a hologram. Reconstructing a real image of the object.

In summary, holography uses optical interference phenomena to store both wavefront amplitude and phase information onto photographic recording media. The recorded interference pattern, which is called hologram, behaves like a diffraction grating. A hologram can be used to completely reproduce wavefronts with the same amplitude and the same phase function as the original object wavefront.

2.2. COMPUTER-GENERATED HOLOGRAMS

As depicted in the previous section, holograms are constructed by the means of interferometry. Physical existence of an object is required during the recording process. Computer-generated holography, on the other hand, eliminates this constraint. A computer-generated hologram (CGH) is produced via computer synthesis, where the object does not exist physically but it is expressed in mathematical terms.

Synthesizing holograms with the aid of computers allows complex waveforms to be produced that could not be realized otherwise. Practical considerations in holographic recording process such as illumination coherence, vibration, or air turbulence are of no concern for computer-generated holograms. Furthermore, CGH allows the study of certain holographic effects simply through computer simulation. There are other advantages of computer-generated holograms, which are associated with the fact that a binary diffraction pattern can be used instead of the recorded gray-scaled interference fringe pattern as for ordinary holograms **[Brown and Lowmann 1969]**.

High degree of flexibility in generating complex wavefront has made computer-generated holograms extremely important and widely employed in the fields of optical data-storage, image processing, laser scanning systems, and optical testing and metrology.

2.2.1. Computer-Generated Holograms: General Description

The process required for creating computer-generated holograms consists of four steps **[Lee 1978; Bryngdahl and Wyrowski 1990; Goodman 1996]**. The first step is to define a complex wavefront, called the object wavefront, which the finished CGH will be used to reproduce. Then, propagation of the complex wavefront from the object position to the hologram plane is computed by using inverse wave-propagation relationship. For example, if the object is located in the far field of the hologram plane, propagation from the object to the hologram can be computed using Fourier transform base on scalar diffraction theory. Next, a suitable encoding method is chosen to encode both the amplitude and the phase information of the wavefront at the hologram plane to a real and non-negative function. The last step of the process is to output the encoded hologram data via a proper output device. A block diagram shown in Figure 2.4 summarizes the four-step procedure of producing a CGH.

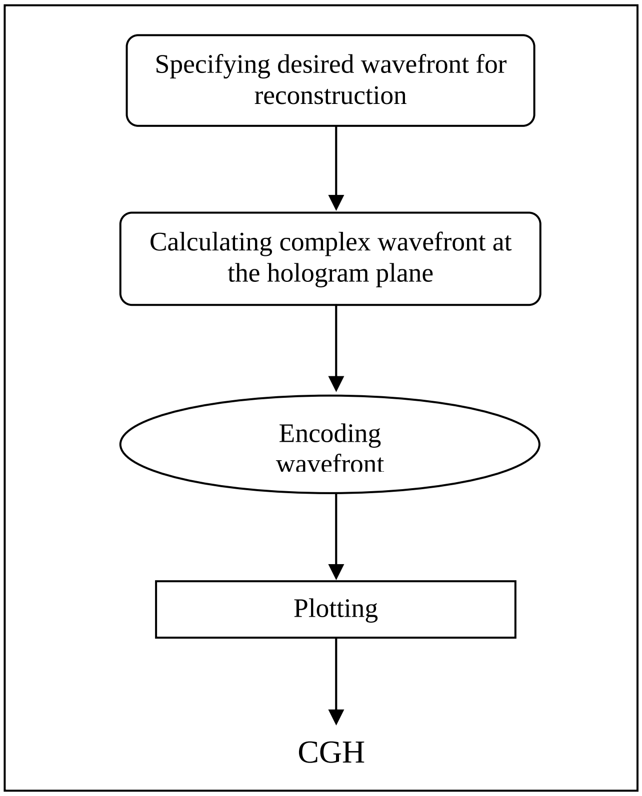

Figure 2.4. CGH generation flow-chart.

Historically, CGHs were generated by plotting the encoded hologram pattern at a much large scale than the final size; then the pattern is photographically reduced to the desired dimension. Nowadays, state of the art laser-beam lithography and electron-beam lithography technologies allow CGHs to be directly written at their finished size, which eliminate the photo-reduction process. Micro-lithography also allows the hologram to be generated at a much higher accuracy than the conventional photo-reproduction process. In Section 2.3, a review on both laser and electron-beam lithography for CGH fabrications is given.

2.2.2. Different Types of CGHs

There are two basic types of computer-generated hologram: amplitude holograms and phase holograms. An amplitude hologram stores both the phase and the amplitude information of the incident wavefront. A phase hologram assumes constant amplitude for the object wavefront. A phase hologram operates only on the phase function of the reconstructing wavefront.

Computer-generated holograms may be produced using different forms of wavefront encoding methods. In the following section, three of the most representative forms of CGH encoding method are reviewed: detour-phase hologram, kinoform, and binary computer-generated hologram. Binary holograms are normally preferred due to their advantages over gray-scaled holograms **[Brown and Lohmann 1969]**. In comparison to gray-scaled holograms, binary holograms are less sensitive to non-linearity of the photographic recording process; binary holograms are also more light efficient.

Detour Phase Hologram

Detour phase method, invented by Brown and Lohmann in 1966, is the oldest and the most studied technique for complex wavefront encoding **[Brown and Lohmann 1966]**. As its name states, detour phase hologram encodes wavefront phase function using “detour phase” as in diffraction gratings.

It is known that optical path difference (OPD) or phase difference between rays through adjacent slits of a perfect grating, in the first diffraction order, is exactly one wavelength. The OPD for rays through a dislocated slit and its neighbor, on the other hand, will be greater or less than one wavelength (Figure 2.5). This phase deviation from an integral wavelength due to the dislocation of the grating slit is called “detour phase”. Detour phase can be used for representing phase variations of a wavefront. It also forms the basis for encoding wavefront phase information in computer-generated holograms.

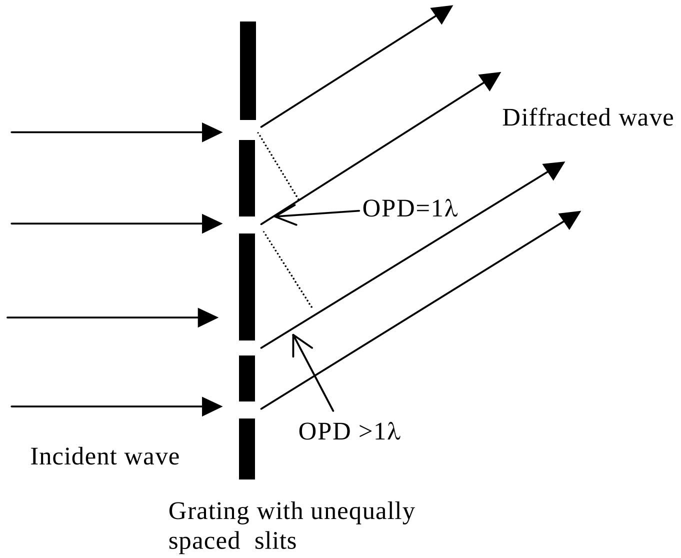

Figure 2.5. Detour phase from unequally spaced grating slits.

In a detour phase hologram, the hologram is divided into a matrix of equally spaced square cells. A rectangular aperture is placed in each cell of the hologram (Figure 2.6). The rectangular aperture inside each cell is varied in height (h_{nm}), width (w_{nm}) and center position with respect to the center of the cell ($c_{nm,}$) based on the amplitude and the phase values of the recorded wavefront at the cell location (Figure 2.7).

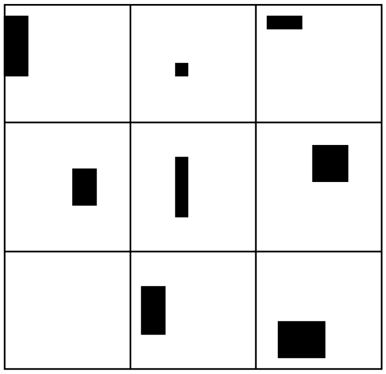

Figure 2.6. Detour phase hologram.

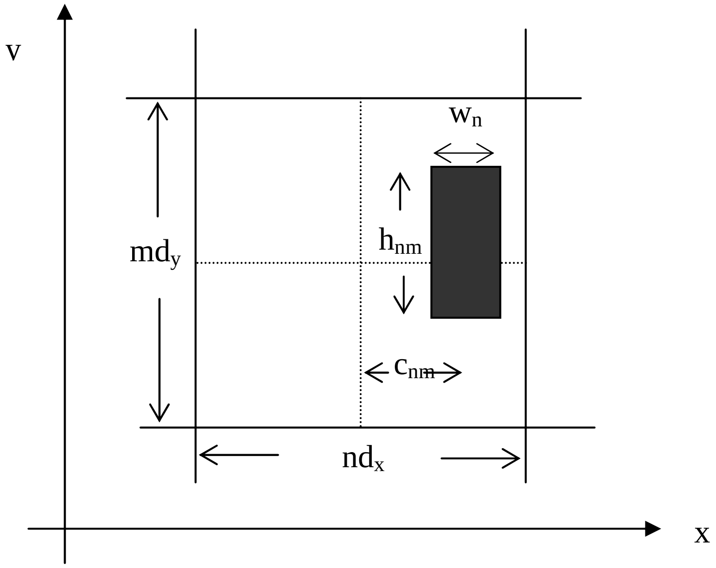

Figure 2.7. Cell structure in a detour phase hologram.
(subscripts m and n denote the x and y coordinates of the cell)

In a detour phase hologram, the area of each rectangular aperture, h_{nm} x w_{nm}, is made to be proportional to the modulus of the amplitude of the represented complex field at the cell position. At the same time, the aperture center position, C_{nm}, is made to be proportional to the phase value of the complex field at the cell location. Using this method, both the amplitude and the phase function can be encoded in the hologram. When a reconstruction wavefront passes through a detour phase hologram, both the amplitude and the phase values are modulated at each cell position.

Detour phase hologram relies on the dislocation of adjacent apertures in the hologram to store complex wavefront information. This technique can only approximate the wavefront amplitude and phase values due to the quantization process. Moreover, it is inadequate to handle large phase variations because the maximum phase variation that can be represented by the dislocation of each aperture is limited to 2π radiance. When the phase variation of the wavefront exceeds multiple of 2π, adjacent apertures will overlap in detour phase holograms **[Lee 1979]**.

Although a number of techniques have been suggested to eliminate the overlapping aperture problem, the inaccuracy of phase representation using detour phase method and difficulties in managing large phase variations in the object wavefront are inherent to this encoding method. **[Lohmann and Paris 1967; Brown and Lohmann 1969**; **Lee 1970; Burckardt 1970; Hugonin and Chavel 1976; Hsueh and Sawchuck 1978; Bartelt and Forster 1978]**.

Kinoform

Kinoform was developed in 1969 by Lesem, Hirsch and Jordan **[Lesem et. al. 1969]**. A Kinoform is produced by recording phase variations of the desired wavefront onto films as relief patterns rather than transmittance variations. The magnitudes of the relief patterns are set to be proportional to the phase variations modulo of 2π **[Lesem et. al. 1969]**. In a Kinoform hologram, the amplitude of the incident object wavefront is assumed to be constant; and only the phase information is used for the construction of the image of the object.

Kinoform can be thought as a simple phase-shaping element. It transforms the incident wavefront shape into forms that is needed to produce the desired image. A Fresnel lens shown in Figure 2.8 is a simple Kinoform, where the continuous phase function $\phi(x, y)$ is converted into surface relief height that can be determined using:

$$d_{\max} = \frac{\lambda_0}{2\pi(n_0 - 1)} \tag{2.12}$$

where n_0 is the index of refraction of the substrate at the incident wavelength (λ_0).

As shown in Section 2.1.1, an amplitude hologram produces multiple diffractive orders during the reconstruction process. A Kinoform, on the other hand, eliminates multiple orders by modulating only on the phase function of the incident wavefront. It provides higher diffraction efficiency by producing single image without undesired diffraction orders. Because a Kinoform does not require a reference wave or fringe carrier frequency, the reconstructed image may be centered on the optical axis. Kinoform is also less computationally intensive when compared to other hologram encoding methods.

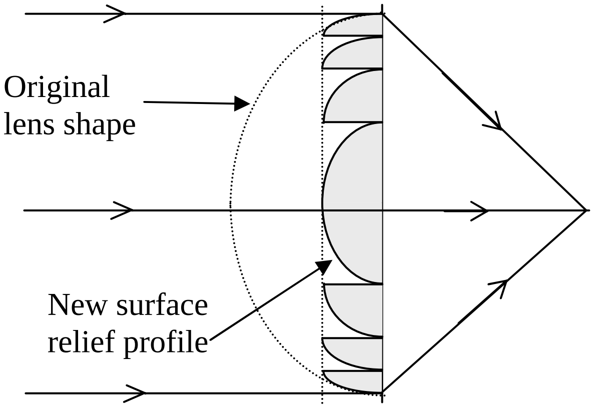

Figure 2.8. Structure of a Fresnel lens.

Binary CGH

In 1974, Lee introduced a new type of computer-generated hologram called binary computer-generated hologram. The new hologram encoding method solves the two fundamental problems in detour phase holograms. In his paper, Lee showed that patterns in binary computer-generated holograms could be interpreted as interference fringes in conventional holograms **[Lee 1974]**.

It was shown that an interference pattern is obtained from the interference between the reference and the object beam (in Section 2.1.1). If the reference wavefront is an off-axis plane wavefront with an angular spectrum of $2\pi\alpha x$, then Equation (2.3) and (2.5) becomes:

$$R(x,y) = R_0 \cdot e^{i2\pi\alpha x} \tag{2.12}$$

$$I(x,y) = R_0^2 + O^2(x,y) + 2 \cdot R_0 \cdot O_o(x,y) \cdot \cos\left[2\pi\alpha x - \phi(x,y)\right] \tag{2.13}$$

The third term in Equation (2.13) gives the sinusoidal fringe modulation; bright and dark interference fringes are observed at locations where:

Bright fringes: $$2\pi\alpha x - \phi(x,y) = 2\pi n \tag{2.14}$$

Dark fringes: $$2\pi\alpha x - \phi(x,y) = 2\pi\left(n + \frac{1}{2}\right) \tag{2.15}$$

where, $n = 0, \pm 1, \pm 2 \ldots$

If the sinusoidal fringe function is hardclipped with zero threshold, the output function g(x,y) will have values of 1 and 0 where $\cos\left[2\pi\alpha x - \phi(x,y)\right]$ has values that are positive and negative respectively (Equation 2.16).

$$g(x,y) = \begin{cases} 1 & \text{for}\cos[2\pi\alpha x - \phi(x,y)] \geq 0 \\ 0 & \text{otherwise} \end{cases} \tag{2.16}$$

This type of hologram is usually referred to as a binary phase hologram. It is also the focus of this dissertation.

It is not hard to realize that binary holograms generated by hardclipping the fringe function with a zero threshold will result in a lost of amplitude information of the object wavefront (see Equation 2.16). This recording technique is sufficient only when constant wavefront amplitude is assumed for the object beam. When the amplitude information $O_0(x, y)$ is needed, however, the hardclipping process must be re-considered.

As Lee pointed out in his paper, when the constant threshold is replaced with a bias function $\cos[\pi q(x)]$ for the hardclipping process, amplitude fluctuation of the object wavefront may be preserved. Figure 2.9 shows the generation of binary fringes using the new bias function:

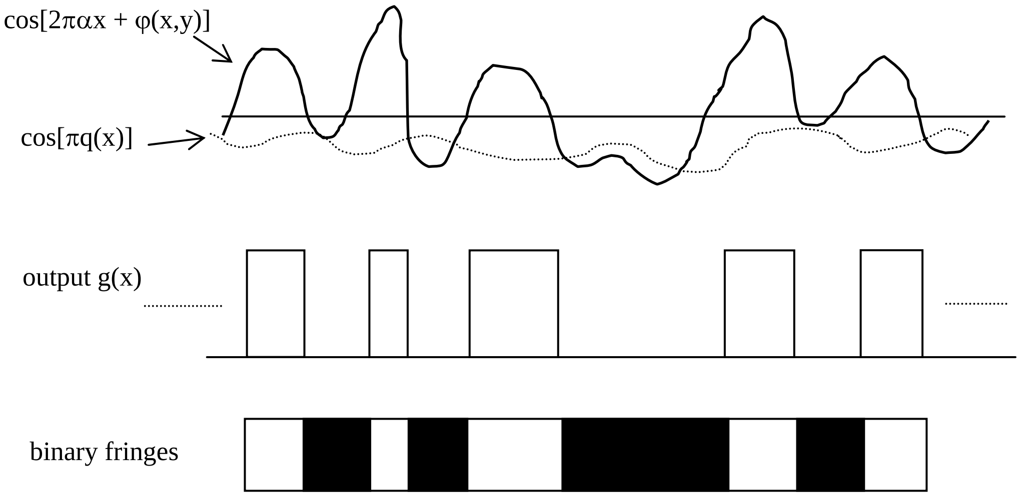

Figure 2.9. Binary CGH encoding process.

Original fringe function along the modulation direction, x-direction, is biased and then hardclipped. In 1-D, along x-axis, the output binary function g(x) has a leading and a trailing edge that may be defined by:

$$\cos[2\pi\alpha x - \phi(x, y)] = \cos[\pi q(x, y)] \tag{2.17}$$

and

$$2\pi\alpha x - \phi(x, y) = 2\pi n \pm \pi q(x, y) \tag{2.18}$$

A Fourier series representation of the 2-D binary output function g(x,y) is:

$$g(x,y)=\sum_{m=-\infty}^{\infty}\left[\frac{\sin[\pi m q(x,y)]}{\pi m}\right]\cdot e^{im[2\pi\alpha x-\varphi(x,y)]} \tag{2.19}$$

There are many ways to encode wavefront amplitude information into the binary output function g(x,y). One simple approach is to select the bias function so that:

$$\sin[\pi q(x,y)]=O_0(x,y) \tag{2.20}$$

In this case, the m = 1 term in the Fourier series will result in an amplitude factor in the Fourier expansion term:

$$\frac{\sin[\pi q(x,y)]}{\pi}=\frac{1}{\pi}O_0(x,y) \tag{2.21}$$

As a result of this, the original object wavefront $O_0(x,y)\cdot e^{i\phi(x,y)}$ is reconstructed in the first diffracted order (m = ± 1).

Using this method, both the phase and the amplitude information of the object wavefront are encoded in the position and the width of the binary fringe patterns. This binary holographic encoding method allows the recording of complex wavefront information without resorting to approximations as in the detour phase method.

2.2.3. Separation of Multiple Diffraction Orders

Similar to binary gratings, binary holograms generate multiple diffraction orders during the reconstruction process. Although different diffraction orders are spatially separated, cross talk between adjacent orders will occur when the separations between the orders are less than their width. Overlapping diffraction orders degrade the quality of the diffraction wavefront. One way to eliminate this order overlapping is to apply a "carrier frequency" to the encoded hologram fringe pattern **[Creath and Wyant 1992]**.

For a binary linear hologram, a linear carrier frequency that is equivalent to a wavefront tilt can be used to separate overlapping orders. The linear carrier frequency added to the hologram pattern produces a lateral spatial shift to the diffracted orders in the image plane. A carefully selected carrier frequency applied to a hologram can be used to increase the spacing between adjacent diffraction orders, which allows the desired diffraction order to be fully isolated from its neighbors. Figure 2.10 shows a drawing of a linear CGH with 1 wave Zernike spherical and 36 waves of tilt.

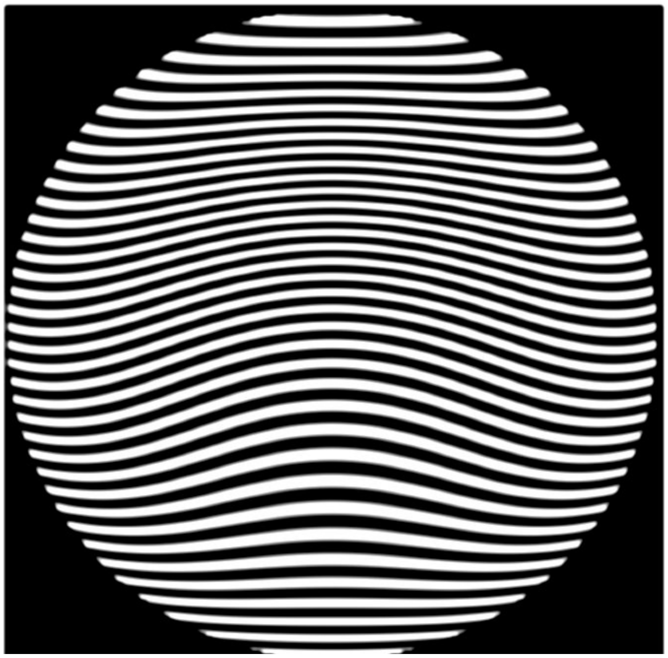

Figure 2.10. A linear CGH with 1 wave Zernike spherical and 36 waves of tilt.

Figure 2.11 shows the spot diagram of multiple diffraction orders generated by the linear CGH that possesses 1λ Zernike spherical aberration. The hologram produces a F/5 converging beam at a reference wavelength of 550nm.

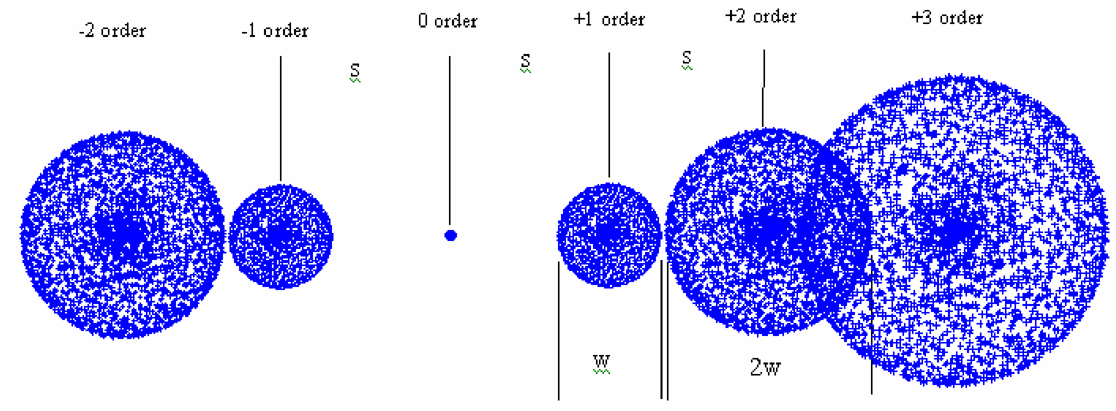

Figure 2.11. Spot diagram showing multiple diffraction orders with orders overlapping.

In order to separate the +1 and the +2 diffraction order beams, the two orders must be separated by at least the sum of the half width of the two beams; or

$$s \geq \frac{w_1}{2} + \frac{w_2}{2} \tag{2.22}$$

$$s \geq \frac{3}{2} w_1 \tag{2.20}$$

where w_1 and w_2 are the geometrical spot diameters for the two diffraction orders; and $w_2 = 2w_1$. It is obvious that a minimum geometrical spot size for the +1 diffraction order is desired to achieve the lowest carrier frequency or wavefront tilt for the separation of +1 and +2 diffraction orders in this case.

Both wavefront aberration and ray aberration plots for the +1 diffraction order at the minimum geometrical spot size position are shown in Figure 2.12 and Figure 2.13 respectively. The beam width (w_1) is found to be 66 um at this position. Thus, a separation of 99 um between the +1 and the +2 orders is required to eliminate beam overlapping. This lateral separation between the two beams corresponds to a wavefront tilt of 36 waves. The finished hologram with 36 waves tilt is shown in Figure 2.10.

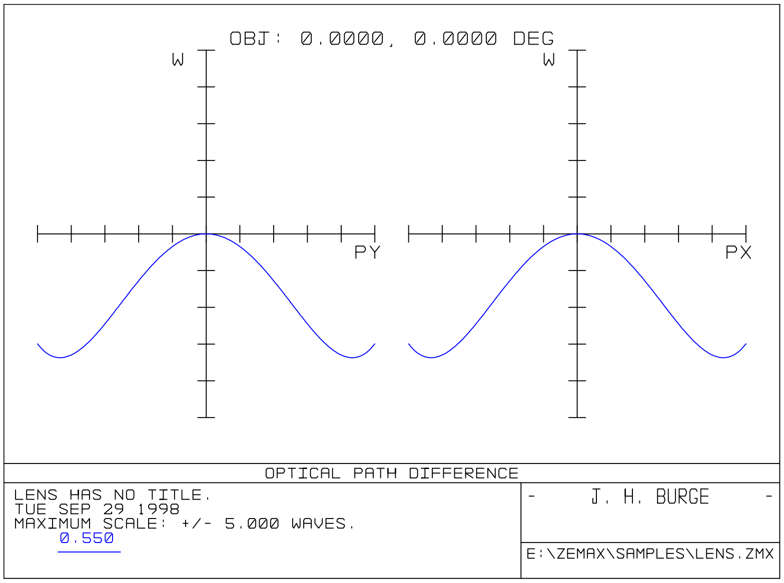

Figure 2.12. Wavefront aberration plot for +1 diffraction order.

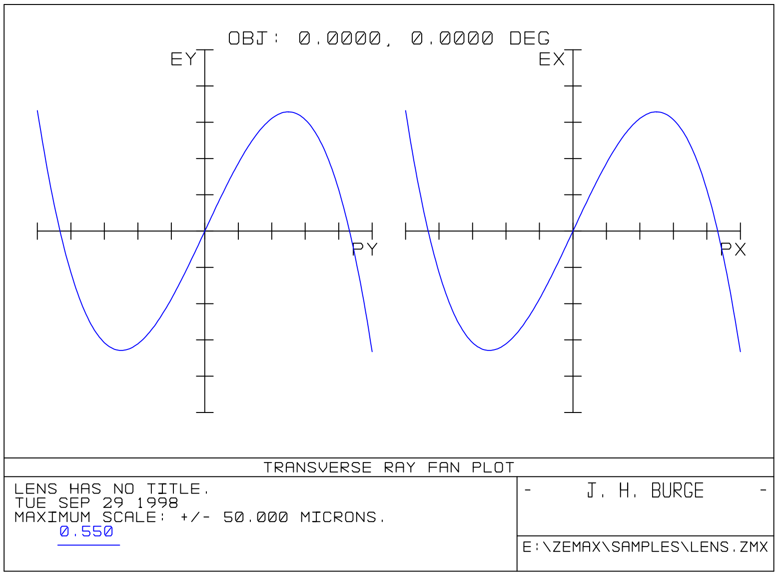

Figure 2.13. Ray aberration plot for +1 diffraction order.

For ring shape holograms, multiple diffraction orders may appear along the optical axis of the hologram. A quadratic carrier frequency, which may be treated as wavefront defocus, produces axis shifts to the diffracted beams. It may be used to separate overlapping orders for ring holograms.

2.3. CGH FABRICATIONS

Traditional method for fabricating computer-generated holograms is done through automated plotting and photographic reduction **[Lohmann and Paris 1967].** Encoded hologram transmission function is first transferred to a mask by a computer-driven plotter at a greatly enlarged scale. The resulting plot is then photographically reduced to the desired size on high-resolution films. The whole fabrication process could take several days to complete. Accuracy of this fabrication process is limited by the precision of the plotter and errors associated with the photo-reduction process **[Ono and Wyant 1974].** These disadvantages of the photo-reproduction process have prevented CGH from broad applications in practice.

With increasing demands for holograms with finer structure detail, new techniques for fabricating holograms are in need. Advances in micro-lithographic technologies have made it possible to manufacture holograms with high precision and finesse. Both electron beam lithography and laser beam lithography have been used to generate CGHs through direct writing process, or to produce replication masters for large volume production of CGHs.

Micro-lithographic technique was originally developed for the semiconductor industry for integrated circuits (IC) fabrication. The process contains four steps: exposure, development, etching, and cleaning. The exposure process requires coating of a thin layer of metal following by a thin layer of resist over the substrate. A laser or electron beam may be used to expose the resist layer where the beam strikes. The finished piece is then cleaned with solvent. If a negative type resist is used, the resist layer will become less soluble at the exposed areas. If a positive type resist is used, the exposed regions become more soluble. Next, an etching process removes regions on the metal layer that are not covered with resist. Finally, a second chemical solution strips the remaining resist from the substrate. The described process is illustrated in Figure 2.14.

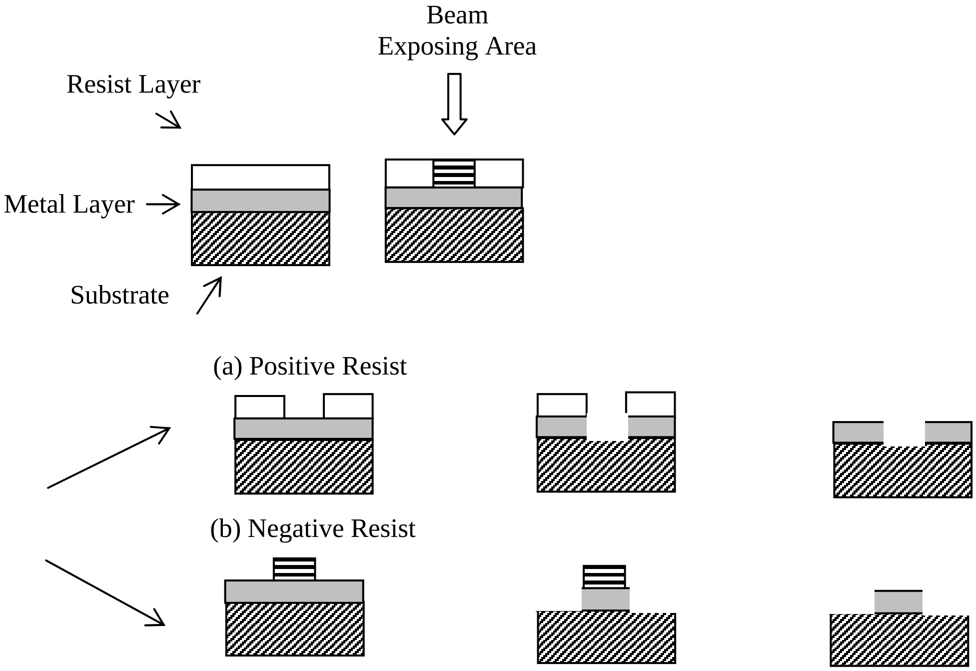

Figure 2.14. Schematic drawings show the processes of micro-lithography.

System setups for both laser beam and electron-beam writers are very similar. They both require a precision translation stage and a writing head. The servo controlled translation stage is usually mounted on an air-bearing table for friction free motion. Precise motion control of the stage is essential for obtaining high quality surface structures during the writing process. Distance-measuring interferometers are typically used to maintain sub-micron accuracy of the stage position.

Electron beam lithography uses an electron beam to generate patterns onto an electron-resist layer coated on a glass plate. Typically, an electron-beam writing head consists of an electron gun and electron-optics lenses for beam shaping, deflection and focusing. There are two basic types of electron-beam writers, different by their beam shaping systems: electron beam focusing or variable beam shaping **[Hessler 1997]**.

Different from the e-beam systems, a laser source is incorporated in the writing head for a laser beam writer. The wavelength of the laser source is chosen upon the need of the specific application and the photo-resist type. Typically, a gas laser with operating wavelength in the range of 400 to 600 nm is used **[Baber 1989; Haruna et. al. 1990; Bowen el. Al. 1997; Hessler 1997]**. The laser source is frequency stabilized. The output beam is filtered by a spatial filter and focused on the resist layer. An acoustic-optical (AO) modulator is used to modulate the output beam intensity during the writing process. An auto-focusing unit is often used to control the beam focusing optics to ensure that the writing beam is focused on the resist layer at all time during the process.

In general, an electron-beam writing system provides higher resolution than a laser beam writer does. The minimum spot size of a laser beam writer is limited by the diffraction spot size of the output beam, which is limited by the wavelength of the laser source. Minimum feature size that can be produced by a typical laser writer is about 500 nm currently. Electron beam writers, on the other hand, can achieve a minimum spot size of 100 nm. In some e-beam systems less than 20 nm structures have been produced.

Despite of the high spatial resolution, equipment cost and maintenance cost for typical e-beam writers are much higher in comparison to laser writers **[Hessler 1997].**

2.4. CGH MODELING THEORY

Scalar diffraction theory is commonly used for analyzing diffractive optical elements. Scalar diffraction theory assumes that light propagates in a linear, isotropic, homogeneous and non-dispersive media. All components of the electric and the magnetic fields behave identically; and they can be fully described by a single homogeneous scalar wave equation **[Born and Wolf 1980]**. Scalar diffraction theory requires that the size of the diffracting feature much be large compared with a wavelength of the incident light; and the diffracting fields must not be observed too close to the diffracting structures **[Goodman 1996]**.

Detailed derivations and developments of the scalar diffraction theory are not presented in this paper, since a handful of textbooks are available that cover this topic in great details **[Born and Wolf 1980; Goodman 1996]**. The result of Rayleigh-Sommerfeld approximation solution of the scalar diffraction theory is given in Equation (2.21). The Rayleigh-Sommerfeld diffraction formula provides a general description of the relationship between the diffracted wavefront ($U_1(x,y)$) and the incident wavefront ($U_0(\xi,\eta)$). The Rayleigh-Sommerfeld integral is often interpreted as one form of mathematical statements of the famous Huygens-Fresnel principle **[Born and Wolf 1980]**.

$$\begin{aligned} U_1(x,y) &= \frac{1}{\mathrm{i}\lambda}\iint_{\Sigma} U_0(\xi,\eta)\frac{\mathrm{e}^{\mathrm{i}k\mathrm{r}_{01}}}{\mathrm{r}_{01}}\cos(\vec{\mathrm{n}},\vec{\mathrm{r}}_{01})\mathrm{d}\xi\mathrm{d}\eta \\ &= \frac{\mathrm{z}_{01}}{\mathrm{i}\lambda \mathrm{r}_{01}^2}\iint_{\Sigma} U_0(\xi,\eta)\mathrm{e}^{\mathrm{i}k\mathrm{r}_{01}}\mathrm{d}\xi\mathrm{d}\eta \end{aligned} \tag{2.21}$$

where:

U_0 = incident wavefront function;

U_1 = complex diffraction wavefront at z_1 plane;

z_{01} = distance between the observation and the aperture planes;

$k = 2\pi/\lambda$;

λ = wavelength of incident light;

$\cos(\vec{n},\vec{r}_{01})$ = direction cosine between surface normal $\vec{n}$ and vector $\vec{r}_{01}$.

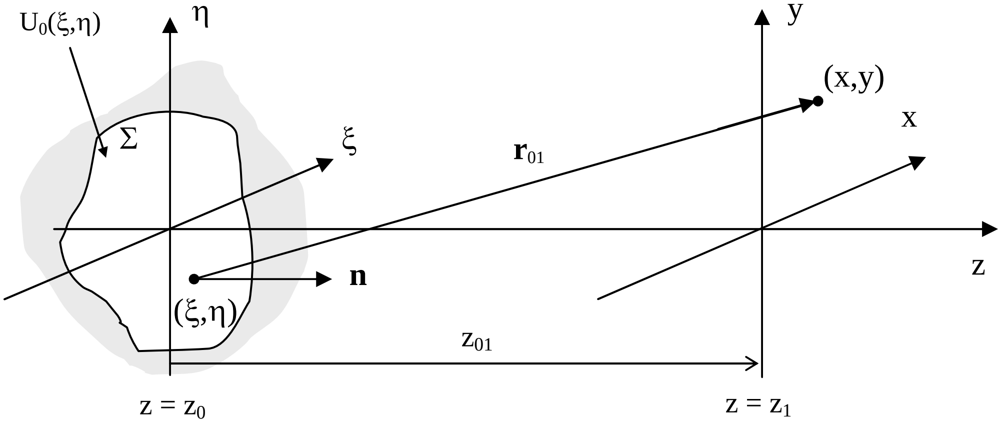

Figure 2.15. Geometry for Rayleigh-Sommerfeld diffraction integral.

The Rayleigh-Sommerfeld formula can be applied generally to any diffraction situation, whenever the two requirements for scalar approximation are satisfied. Nevertheless, the complexity of the integral has limited the use of Rayleigh-Sommerfeld in practical applications. In practice, simplified forms of the Rayleigh-Sommerfeld integral are usually used by imposing more approximations and restrictions.

Fraunhofer Diffraction Approximation

When the separation between the z_0 and z_1 plane in Figure 2.15 is much greater in comparison to both the maximum radial extent of the aperture ($\sum$) and that of the observation region, r_{01} can be approximated as:

$$
\begin{aligned}
r_{01} &= \sqrt{(x-\xi)^2+(y-\eta)^2+z_{01}^2} \\
&= z_{01}\sqrt{1+\left(\frac{x-\xi}{z_{12}}\right)^2+\left(\frac{y-\eta}{z_{12}}\right)^2} \\
&\cong z_{01}\left[1+\frac{1}{2}\left(\frac{x-\xi}{z_{12}}\right)^2+\frac{1}{2}\left(\frac{y-\eta}{z_{12}}\right)^2\right]
\end{aligned}
\tag{2.22}
$$

Equation (2.21) becomes:

$$
U_1(x,y)=\frac{\mathrm{e}^{\mathrm{i}kz_{01}}}{\mathrm{i}\lambda z_{01}}\iint_{\Sigma} U_0(\xi,\eta)\mathrm{e}^{\mathrm{i}\frac{\pi}{\lambda z_{01}}\left[(x-\xi)^2+(y-\eta)^2\right]}\mathrm{d}\xi\mathrm{d}\eta \tag{2.23}
$$

This result is commonly known as the Fresnel diffraction integral. Furthermore, when z_{12} is much greater than $\frac{k(\xi^2+\eta^2)_{\max}}{2}$, so that the quadratic phase term $e^{-j\frac{k}{2z}(\xi^2+\eta^2)}$ in the Fresnel integral (Equation 2.23) can be neglected. We will arrive:

$$U_1(x,y) = \frac{e^{ikz_{01}} e^{i\frac{k}{2z_{01}}(x^2+y^2)}}{i\lambda z_{01}} \iint_{\Sigma} U_0(\xi,\eta) \exp\left[-i\frac{2\pi}{\lambda z_{01}}(x\xi + y\eta)\right] d\xi d\eta \qquad (2.24)$$

This result is known as the Fraunhofer (or far-field) diffraction solution. The expression for the Fraunhofer integral is mathematically equivalent to a 2D Fourier transform of the incident wavefront over the defined aperture. In practice, the far field conditions described above are easily satisfied and the Fraunhofer solutions are often used. Computational simplicity of this solution makes it a powerful tool in diffraction analysis.

The Fraunhofer solution is adequate in dealing with vast majority of diffraction problems. It also serves as the theoretical foundation of our research from chapter 3 through chapter 5. In chapter 6 and 7, we will introduce the rigorous diffraction theory which impose no approximations to general diffraction problems. Differences between the scalar diffraction model and the rigorous model are discussed in detail.

2.5. APPLICATIONS OF CGHS IN OPTICAL TESTING

The ability of generating complex wavefront with arbitrary amplitude and phase functions has made CGHs extremely attractive in a wide range of applications. To stay within the scope of this work, we will focus our discussion on the applications of CGH in the field of optical metrology and testing.

Among numerous types of optical metrology systems, CGH has found its greatest potentials in the field of optical interferometry **[MacGovern and Wyant 1971]**. A brief review of optical interferometry is provided in the following section; applications of CGH in interferometry are then introduced.

2.5.1. Optical Interferometric Systems

Optical interferometry is based on the optical interference phenomena. Two interfering wavefronts are produced by a reference surface and a test surface respectively. Shape differences between the reference and the test surface result in phase differences between the two wavefronts. The generated interference pattern, also called interferogram, is interpreted as a contour map of constant height difference between the test and the reference surfaces. The interferogram is captured and digitized by a CCD camera in an interferometer. The shape of the test surface may then be obtained by analyzing the interferogram pattern and knowing the shape of the reference surface.

A schematic drawing of a Twyman-Green interferometer is shown in Figure 2.16. The setup consists of a laser source, a beam splitter, a reference surface and a test surface. The laser beam output is split into two paths by the beam splitter: one towards the reference arm and one towards the test arm. The configuration showed in Figure 2.16 is designed for testing concave spherical surfaces. The test surface is placed at the position where its radius of curvature matches the radius of curvature of the diverging test beam. Both beams reflected off the reference and the test surfaces are recombined through the beam splitter and interfere in space. The formed interferogram is captured by a CCD camera.

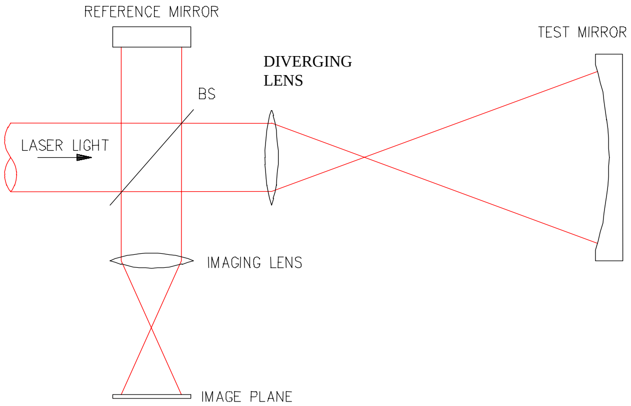

Figure 2.16. Schematic drawing of a Twyman-Green interferometer.

Optical interferometry is a relative measurement of the test surface against a reference. A larger shape difference between the test and the reference surfaces will be seen as an increase in the number of fringes in the interferogram. Sampling frequency of the CCD camera and the digitization process limits the maximum number of interference fringes allowed in an interferogram. In order to avoid fringe aliasing, sampling condition described by the Whittaker-Shannon sampling theorem **[see e.g. Gaskill 1978]** must be met. This fringe sampling restriction requires the reference surface to have almost the same shape as the surface under measurement. Consequently, a large collection of reference surfaces must be made available in order to measure surfaces with a wide range of shapes for optical interferometry.

2.5.2. CGHs in Optical Testing

Aspheric surfaces play an important role in modern optical systems. Many optical systems can benefit from the use of aspheric surfaces. Extra degrees of freedom in controlling the shape of optical surfaces help optical designers in controlling wavefront aberrations in optical imaging systems. By using aspheric optical elements, system performance can be improved while the number of optical elements may be reduced. Despite the advantages of aspheres, applications of aspheric components are still limited. The major obstacle in the broad usage of aspheres comes from the difficulties in asphere metrology and testing.

As discussed in the previous section, optical interferometry requires the reference surface to have the same shape as the surface under test. For asphere testing, this requirement translates into that an exact replicate of the asphere under test must be fabricated as the reference in order to measure the part. Unfortunately, conventional optical fabrication process based on lapping has a natural tendency of producing spherical surfaces **[Park 1987].** Non-spherical surfaces are difficult and costly to produce.

One way to test aspheres without the use of reference aspheres is to design a set of additional optics. The additional optics are used to generate a wavefront that matches the ideal shape of the test surface and replace the reference in an interferometer **[Offner and Malacara 1992]**. This set of optics is called "null lenses" to indicate its purpose: to reduce shape difference between the reference and the test wavefronts; or null the interference fringes in the interferogram. Depending upon the complexity of the desired reference wavefront, null lenses usually consist of several optical elements.

It is expensive and time consuming to test aspheres using either reference aspheres or null lenses. Besides, verifying the accuracy of the reference aspheres or the null lenses is no easy task of its own.

State of the art fabrication techniques such as diamond turning and injection molding have made the production of aspheres easier and at costs not much more than spherical surfaces. The ability of manufacturing aspheric components has again driven the demands of fast, accurate and low cost methods for asphere metrology.

Computer-generated holograms allow complex wavefronts to be generated without the physical existence of the object. This ability has made it desirable in the field of asphere metrology. A reference asphere or a null lens is no longer needed with the help of CGH; the desired aspheric wavefront can be synthesized and stored in a CGH. The stored wavefront can later be reconstructed and used in an interferometer as the reference wavefront for testing aspheres or surfaces with essentially any shape.

The first application of CGH for interferometric testing of aspheric surface was demonstrated by MacGovern and Wyant in 1971. Figure 2.17 shows the configuration of a modified Twyman-Green interferometer incorporating a CGH for testing aspheric elements. In this configuration, the CGH is placed at the image plane of the exit pupil of the test element. This arrangement allows both the test beam and the reference beam to travel through the CGH via the same optical path. Because of this, the accuracy of the measurement is not affected by any thickness variations or inhomogeneity in the CGH plate **[MacGovern and Wyant 1971]**.

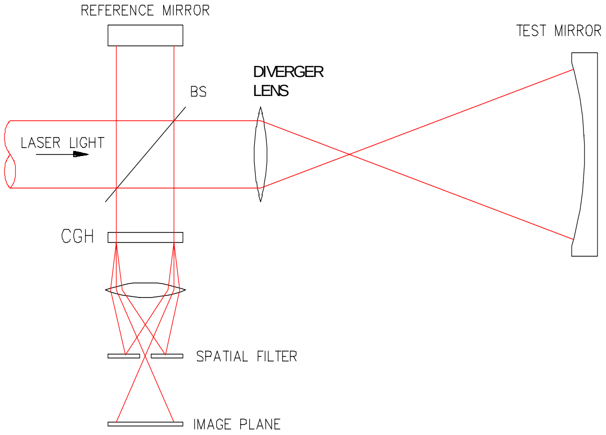

Figure 2.17. Modified Twyman-Green interferometer for asphere testing using CGHs.

The CGH used in Figure 2.17 setup stores the interference pattern expected from a perfect test surface. During the test, an interferogram pattern is produced from the interference between the reference and the test surface. This interferogram is imaged onto the CGH plane. The two overlapping interference patterns produce another fringe pattern, which is called moiré pattern. A moiré pattern is a ‘beat pattern’ produced by two gratings of approximately equal spacing **[Creath and Wyant 1992]**. Straight and equal-spaced moiré fringes will appear when the two interference patterns are identical. Differences between the two interferograms appear as variations of fringe spacing in the moiré pattern. By analyzing the moiré fringe pattern, shape differences between the test part and its ideal form can be quantitatively determined.

There are other interferometers configurations that utilize computer-generated holograms. For instance, a CGH may also be placed in the reference arm of an interferometer. Figure 2.18 shows the layout of such system. The CGH is positioned in the system so that its conjugate image is coincident with the image of the surface under test. In this setup, the CGH produces a reference wavefront that matches the wavefront expected from an ideal test surface.

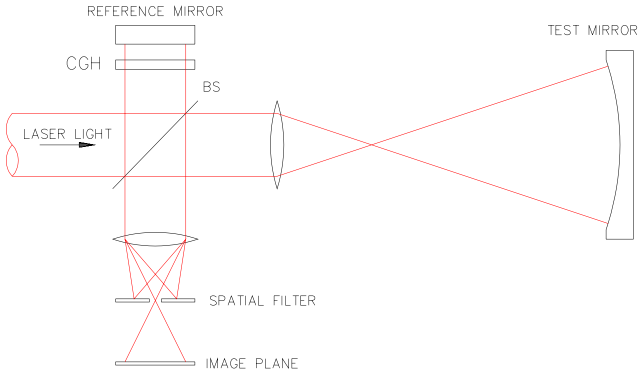

Figure 2.18. Interferometer configuration with CGH in the reference arm.

One shortcoming of this configuration is that a high quality diverger lens is required. Otherwise, wavefront aberrations generated by the diverger lens will propagate into the reference beam, although aberrations introduced by the diverger can also be compensated by including the same amount of aberrations in the CGH designs.

One other commonly used interferometer configuration is to position the CGH in the test arm, as shown in Figure 2.19. This arrangement allows an easier incorporation of the CGH with commercially available interferometers comparing to other configurations. Figure 2.19 shows that by placing the CGH in the path of the test arm, aberrations produced by the diverger lens can be eliminated.

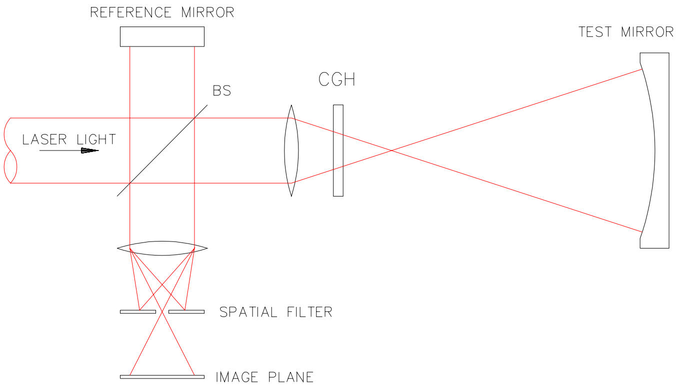

Figure 2.19. Interferometer configuration with CGH in the test arm.

However, in this setup, test beam is twice diffracted by the hologram and intensity of the test beam may be reduced. When the intensity ratio between the reference beam and the test beam is too high, fringe contrast of the interferogram will be low. The intensity of the test beam diffracted by a CGH is determined by the diffraction efficiency of the hologram. A typical chrome-on-glass CGH has a 10% diffraction efficiency **[Arnold 1989; Burge 1995]**. A double diffraction yields only 1% in the return beam. Therefore, CGHs with high diffraction efficiencies are necessary when used in such systems.

CGHs may also be used as the beam-splitter in optical testing. Burge in 1995 demonstrated that aspherical optics may be measured using Fizeau interferometer with a hologram recorded on the reference surface. The hologram pattern written onto the concave spherical reference surface separates and recombines the reference and the test wavefronts (Figure 2.20). Light diffracted from the hologram on the spherical reference surface forms the reference wavefront, and light reflected from the test surface forms the test wavefront **[Burge 1995]**.

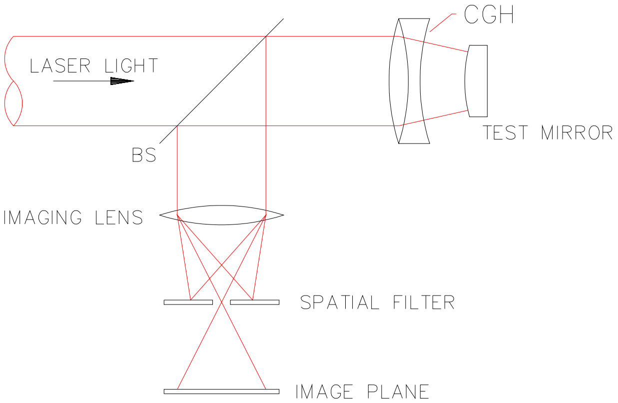

Figure 2.20. Using CGHs as beam splitting elements.

The advantage of this configuration is that the reference surface may have a spherical shape; it can be made and characterized to a high precision. In addition, the small separation between the test and the reference surface helps to significantly reduce air turbulence in the optical path. This interferometer configuration is very useful in testing large convex optical surfaces.

In summary, CGHs can be designed to produce wavefront with virtually any shape. Applications of CGHs in optical interferometry allow surfaces with complex shape to be measured easily and accurately. Computer-generated holograms are especially powerful in interferometric measurements for aspheric surfaces. In order to explore the full potential of CGHs in the field of optical metrology and testing, a thorough understanding of the design and the fabrication limitations is necessary.

CHAPTER 3

WAVEFRONT PHASE ERRORS
PRODUCED BY
CGH FABRICATION UNCERTAINTIES

Errors and uncertainties during CGH fabrication processes result in errors in the diffraction wavefronts created by the finished hologram. When applying the finished hologram in optical testing, accuracy of the measurement results will be affected consequently. Possible sources of errors in CGH fabrication such as substrate figure errors and pattern errors are discussed in this chapter. A binary linear grating model is introduced to analyze wavefront phase errors produced by grating duty-cycle and etching depth variations. Analytical solutions to diffraction efficiency, diffracted wavefront phase functions and wavefront sensitivity functions are derived. These results are used to analyze the performance of phase gratings and chrome-on-glass gratings. Moreover, a graphical representation of diffraction fields is introduced for diffraction wavefront analysis.

3.1. CGH FABRICATION ERRORS

Computer-generated holograms are commonly used in optical interferometry for producing reference wavefronts with desired shapes. Uncertainties from the CGH manufacturing processes produce errors in the finished hologram and the generated reference wavefront. CGH errors compromise the accuracy of the interferometric measurements. Although errors in the CGHs may be introduced during either the design or the fabrication process, fabrication uncertainties are mostly responsible for the degradation of the quality of CGHs **[Burge 1993]**.

A CGH may be treated as a set of complex diffraction fringe patterns written onto a substrate material. Errors in both the recorded grating pattern and the shape of the substrate contribute to errors in the reproduced diffraction wavefront. CGH fabrication errors may be classified into two basic types: substrate figure errors and CGH pattern errors. CGH pattern errors may further be classified as fringe position errors, fringe duty-cycle errors and fringe etching depth errors. These CGH fabrication errors will be discussed in detail in the following sections.

- **Substrate Figure Errors**
- **Pattern Errors**
    - **fringe position errors**
    - **fringe duty-cycle errors**
    - **fringe etching depth errors**

3.2. BINARY LINEAR GRATING MODEL

The simplest form of a hologram is a linear diffraction grating, where the spatial frequency of the grating pattern is constant over the entire hologram. A computer-generated hologram with variable fringe spacing may be viewed as a collection of linear gratings with variable spatial frequency. By controlling the spatial frequencies of these linear gratings across the CGH, incident light can be deflected into any desired form **[Burge 1993]**.

The performance of a CGH may be directly related to the diffraction characteristics of a linear grating **[Sawson 1989]**. Linear gratings are often used for studies on CGH properties in order to avoid mathematical difficulties in modeling complex hologram fringe patterns. To reduce the degree of complexity of our study, linear gratings are also chosen as the model for our work.

3.2.1. Binary Linear Grating

The linear grating model used in our studies is assumed to have binary amplitude and phase distributions. A binary linear grating has a surface relief profile that can be described as an infinite train of rectangular pulses with a uniform width (Figure 3.1).

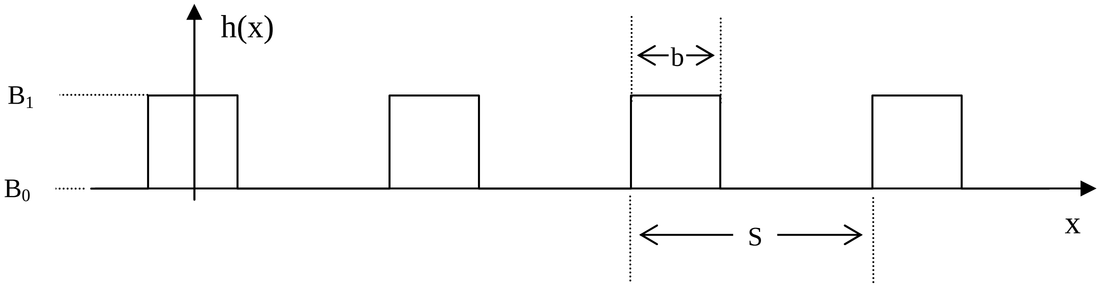

Figure 3.1. Surface relief profile of a binary grating

Using notations from Gaskill's book titled *"Linear systems, Fourier Transforms, and Optics"* **[Gaskill 1978]**, the grating surface relief function *h*(x) may be described mathematically as a convolution of a rectangular function with a width b and series of repeating delta functions equally spaced by *S* apart with a DC offset B_0:

$$\begin{aligned} h(x) &= B_0 + B_1 \cdot \mathrm{rect}\left(\frac{x}{b}\right) * \Sigma\delta(x - mS) \\ &= B_0 + B_1 \cdot \mathrm{rect}\left(\frac{x}{b}\right) * \frac{1}{S}\mathrm{comb}\left(\frac{x}{S}\right) \end{aligned} \tag{3.1}$$

where B_1 and B_0 are complex amplitudes and;

$$\mathrm{rect}\left(\frac{x}{b}\right) = \begin{cases} 1 & |x| < \frac{b}{2} \\ 0 & |x| > \frac{b}{2} \end{cases}$$

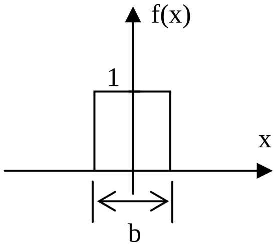

The scalar diffraction approximations can be applied when the wavelength of the incident light is much smaller in comparison to the grating period (*S*). In this case, the output wavefront immediately past the grating, either reflected or transmitted, can be expressed as a simple product of the incident wavefront function and the grating surface profile function. In another word, the grating function modulates the incident wavefront directly. For a normal incident plane wavefront, the output wavefront function can be written as:

$$u(x) = A_o + (A_1 e^{i\phi} - A_0)\mathrm{rect}\left(\frac{x}{b}\right) * \frac{1}{S}\mathrm{comb}\left(\frac{x}{S}\right) \tag{3.2}$$

The form of the output wavefront function expressed in Equation (3.2) resembles the shape of the grating profile (Figure 3.2).

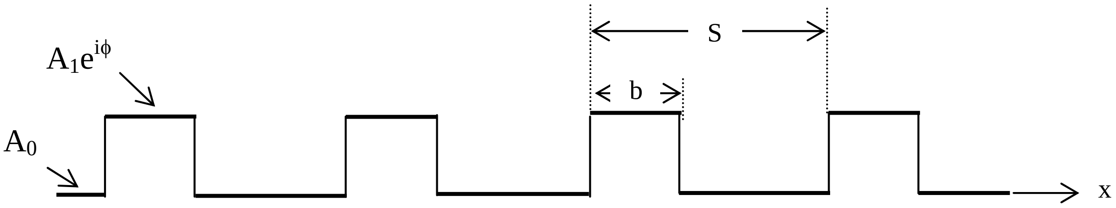

Figure 3.2. Output complex wavefront function at the diffraction grating.

In Equation (3.2), A_0 and A_1 correspond to the amplitude values of the output wavefront from the peaks and valleys of the grating respectively. These two values are determined from the amplitude functions of the reflectance or the transmittance coefficients at the grating interface using Fresnel equations. For a normal incident beam, the complex amplitude of reflectance and the complex amplitude of transmittance can be calculated as:

$$r_{//} = \frac{n_2 - n_1}{n_1 + n_2}, \qquad r_{\perp} = \frac{n_1 - n_2}{n_1 + n_2} \tag{3.3a}$$

$$t_{//} = \frac{2n_1}{n_1 + n_2}, \qquad t_{\perp} = \frac{2n_1}{n_1 + n_2} \tag{3.3b}$$

where n_1 and n_2 are the indices of refraction of the two homogeneous media.

Phase function ϕ, in Equation (3.2), represents the wavefront phase difference between rays reflected off or transmitted through the peaks and the valleys of the grating structure.

In this study, we are mostly interested in the behaviors of the diffraction wavefront in the far-field regime. We have shown earlier in section 2.4 that the far-field diffraction wavefront is related to the original wavefront via a simply Fourier transform relationship based on the Fraunhofer diffraction theory. Hence, the far-field wavefront function of a normally incident plane wavefront upon the grating described in Equation (3.2) is:

$$U(\xi) = \Im\{u(x)\} \tag{3.4}$$

$$U(\xi) = A_0\delta(\xi) + \left(A_1 e^{i\phi} - A_0\right)\cdot b\cdot \sin c(b\xi)\cdot \mathrm{comb}(S\xi) \tag{3.5}$$

$$\begin{aligned}
&= A_0\delta(\xi) + \left(A_1 e^{i\phi} - A_0\right)\cdot D\cdot S\cdot \sin c(DS\xi)\cdot \mathrm{comb}(S\xi)\\
&= \left\{A_0\delta(\xi) + \left[A_1\cos(\phi) - A_0\right]\cdot D\cdot S\cdot \mathrm{comb}(S\xi)\cdot \sin c(DS\xi)\right\}\\
&\qquad + i\left\{A_1\sin(\phi)\cdot D\cdot S\cdot \mathrm{comb}(S\xi)\cdot \sin c(DS\xi)\right\}\\
&= \left\{A_0\delta(\xi) + \left[A_1\cos(\phi) - A_0\right]\cdot D\cdot \sin c(DS\xi)\cdot \sum_{m=-\infty}^{\infty}\delta\left(\xi - \frac{m}{S}\right)\right\}\\
&\qquad + i\left\{A_1\sin(\phi)\cdot D\cdot \sin c(DS\xi)\cdot \sum_{m=-\infty}^{\infty}\delta\left(\xi - \frac{m}{S}\right)\right\}
\end{aligned}$$

or looking at one order at a time:

$$= \begin{cases} \{ A_0 + [A_1 \cos(\phi) - A_0] \cdot D \} + i\{ A_1 \sin(\phi) \cdot D \}; & m = 0 \\ \{ [A_1 \cos(\phi) - A_0] \cdot D \cdot \operatorname{sinc}(mD) \} + i\{ A_1 \sin(\phi) \cdot D \cdot \operatorname{sinc}(mD)\}; & m = \pm 1, \pm 2, ... \end{cases}$$

where $\xi = \frac{x'}{\lambda z}$ and the duty-cycle of the linear grating is $D = \frac{b}{S}$.

Equation (3.5) shows that the diffraction wavefront function $U(\xi)$ has non-zero values only when ξ takes values of multiples integer of $1/S$. This behavior describes the existence of multiple diffractive orders.

In practice, a proper spatial filter may be applied to select a desired diffraction order and isolate it from the others. A typical spatial filter configuration is shown in Figure 3.3.

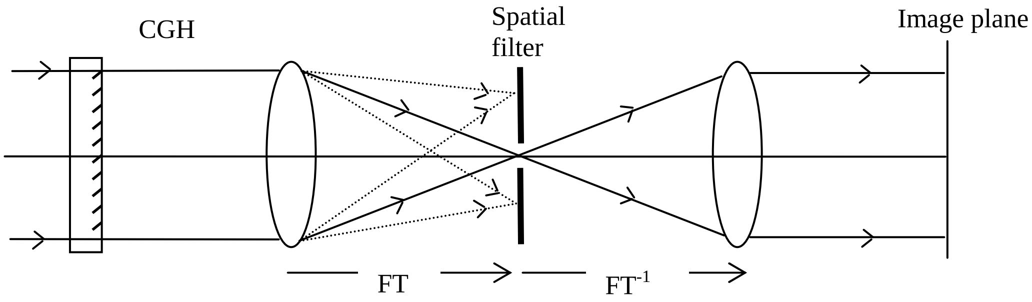

Figure 3.3. Spatial filtering using a 4-F configuration.

3.2.2. Diffraction Efficiency

Diffraction efficiency (η) of a hologram is defined as the ratio of the intensity values of the diffracted wavefront to the intensity of the incident wavefront. The diffraction efficiency of a specific diffraction order provides information of the efficiency of the hologram in deflecting light into a particular direction.

$$I(\xi) = \left|U(\xi)\right|^2 \tag{3.6}$$

For zero-order diffraction beam, $m = 0$:

$$\begin{aligned} I(\xi)\big|_{m=0} &= \left|\left\{ A_0 + \left[A_1\cos(\phi) - A_0\right]\cdot D \right\} + i\left\{ A_1 \sin(\phi)\cdot D \right\}\right|^2 \\ &= \left\{ A_0 + \left[A_1\cos(\phi) - A_0\right]\cdot D \right\}^2 + \left\{A_1 \sin(\phi)\cdot D \right\}^2 \\ &= A_0^2(1-D)^2 + A_1^2 D^2 + 2A_0A_1D(1-D)\cos(\phi) \end{aligned} \tag{3.7}$$

For non-zero diffraction orders, $m = \pm1, \pm2, \ldots$:

$$\begin{aligned} I(\xi)\big|_{m\neq0} &= \left|\left\{ \left[A_1\cos(\phi) - A_0\right]\cdot D\cdot \mathrm{sinc}(mD) \right\} + i\left\{ A_1 \sin(\phi)\cdot D\cdot \mathrm{sinc}(mD)\right\}\right|^2 \\ &= \left\{ \left[A_1\cos(\phi) - A_0\right]\cdot D\cdot \mathrm{sinc}(mD) \right\}^2 + \left\{ A_1 \sin(\phi)\cdot D\cdot \mathrm{sinc}(mD)\right\}^2 \\ &= \left[A_0^2 + A_1^2 - 2A_0A_1\cos(\phi)\right]D^2\,\mathrm{sinc}^2(mD) \end{aligned} \tag{3.8}$$

Diffraction efficiency for all orders are computed by evaluating the intensity values at the particular diffraction orders using Equation (3.15). Hence,

$$\eta = \frac{\left|U(\xi)\right|^2}{\left|U_0(\xi)\right|^2} \tag{3.9}$$

$m = 0$

$$\eta\big|_{m=0} = A_0^2(1-D)^2 + A_1^2 D^2 + 2A_0 A_1 D(1-D)\cos(\phi) \tag{3.10}$$

$m = \pm 1, \pm 2, ...$

$$\eta\big|_{m\neq 0} = \left[A_0^2 + A_1^2 - 2A_0 A_1 \cos(\phi)\right] D^2 \operatorname{sinc}^2(mD) \tag{3.11}$$

3.2.3. Wavefront Phase

Diffraction wavefront phase function can also be retrieved from Equation (3.5). The real part and the imaginary part of the complex wavefront $U(\xi)$ are:

$$\operatorname{Re}\{U(\xi)\} = A_0\delta(\xi) + D\cdot S\cdot\left[A_1\cos(\phi) - A_0\right]\cdot \operatorname{comb}(S\xi)\cdot\operatorname{sinc}(DS\xi) \tag{3.12}$$

$$\operatorname{Im}\{U(\xi)\} = A_1\sin(\phi)\cdot D\cdot S\cdot\operatorname{comb}(S\xi)\cdot\operatorname{sinc}(DS\xi) \tag{3.13}$$

and the diffraction wavefront phase function, Ψ, is determined as:

$$\begin{aligned}\tan(\Psi) &= \frac{\operatorname{Im}\{U(\xi)\}}{\operatorname{Re}\{U(\xi)\}} \\ &= \frac{A_1\sin(\phi)\cdot D\cdot S\cdot\operatorname{comb}(S\xi)\cdot\operatorname{sinc}(DS\xi)}{A_0\delta(\xi) + \left[A_1\cos(\phi) - A_0\right]\cdot D\cdot S\cdot\operatorname{comb}(S\xi)\cdot\operatorname{sinc}(DS\xi)}\end{aligned} \tag{3.14}$$

For different diffraction orders, the phase functions are:

$m = 0$

$$\tan(\Psi)_{m=0} = \frac{DA_1\sin(\phi)}{A_0(1-D) + A_1 D\cos(\phi)} \tag{3.15}$$

$m = \pm 1, \pm 2, ...$

$$\tan(\Psi)_{m\neq 0} = \frac{A_1\sin(\phi)\cdot\operatorname{sinc}(mD)}{[-A_0 + A_1\cos(\phi)]\cdot\operatorname{sinc}(mD)} \tag{3.16}$$

The wavefront phase value, Ψ, can therefore be obtained by taking arctangent of the above equations. The phase unwrapping process uses the sign information of the real and the imaginary parts of the complex wavefront $U(\xi)$ to allow calculation of phase between 0 to 2π period. This is the reason why the sinc(mD) functions are left in both numerator and denominator of Equation (3.16); the sinc functions are there to preserve the sign information for the phase unwrapping process. The new phase values, between 0 and 2π, are then evaluated point by point. A multiple number of 2π phase value can be added or to be subtracted to force the phase function to be continuous.

3.3. WAVEFRONT PHASE ERRORS

CGH fabrication errors may be classified as substrate figure errors and fringe pattern errors. Both types of errors produce deviations in the diffraction wavefront phase. In the following sections, effects of substrate figure errors, pattern distortion, duty-cycle errors, and etching depth errors on diffracted wavefront phase values are studied.

3.3.1. Substrate Figure Errors

Typical CGH substrate errors are low spatial frequency surface figure errors that are responsible for the low spatial frequency wavefront aberrations in the diffracted wavefront. The hologram substrate errors are usually results of the limitations in the fabrication and the testing processes.

In a reflection hologram setup, CGH substrate figure error is 2x amplified in the reflected diffraction wavefront because of the double path configuration (see Figure 3.3). For instance, a surface defect on a CGH substrate with a peak-to-valley deviation of δs will produce a phase error in the reflected wavefront that equals to 2δs. A transmission hologram that has the same peak-to-valley surface defect, on the other hand, will produce a wavefront phase error that is (n-1)δs, where n is the index of refraction of the substrate material.

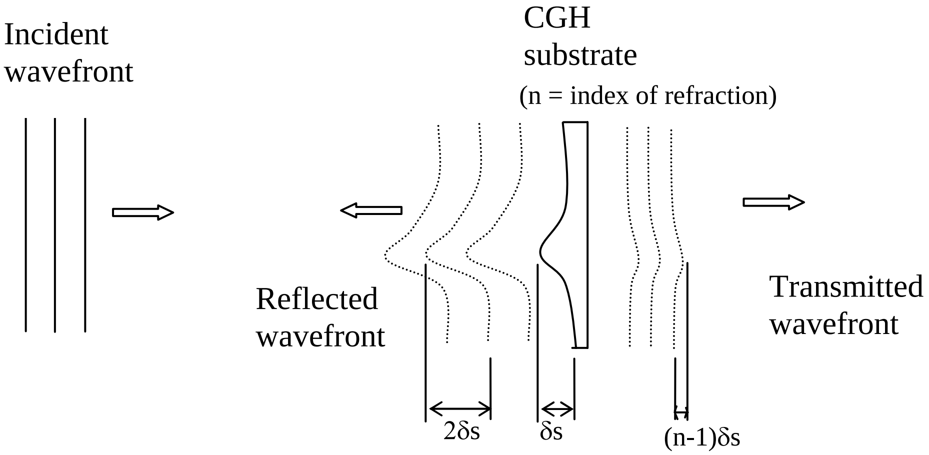

Figure 3.4. Wavefront deviations due to substrate surface defects for both reflective and transmissive type holograms.

One method of eliminating figure errors of CGH is to measure the flatness of the substrate before the grating patterns are applied. This usually can be done by using a Fizeau interferometer with a flat reference.

CGH substrate errors may also be estimated after the grating pattern is written. To show this, a 1-D grating with a high frequency binary fringe pattern and a low frequency substrate variation is demonstrated in Figure 3.5.

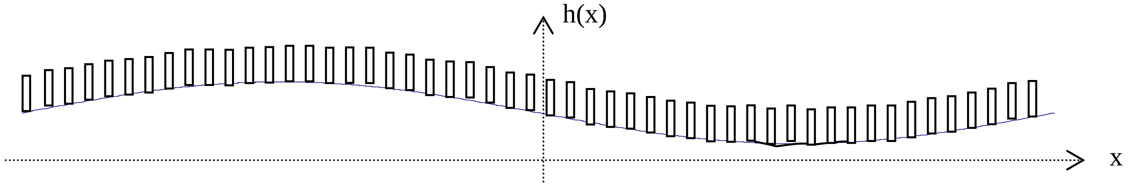

Figure 3.5. 1-D grating profile with sinusoidal substrate figure errors.

For a normal incident plane wave, the output wavefront through this grating can be expressed mathematically as a binary function u(x) (Equation 3.2) with a sinusoidal variation in the phase function from CGH substrate errors:

$$u'(x) = u(x) \cdot e^{ia\cos(\frac{2\pi x}{w})}$$

$$u'(x) = \left[A_0 + \left(A_1 e^{i\phi} - A_0\right) \cdot \text{rect}(x) * \frac{1}{b}\text{comb}\left(\frac{x}{b}\right)\right] \cdot e^{ia\cos(\frac{2\pi x}{w})} \tag{3.17}$$

where

a = amplitude of substrate errors;

w = period of the cosine substrate error and w>>b.

Taylor expansion of the substrate errors in Equation (3.17) can be written as:

$$e^{ia\cos(\frac{2\pi x}{w})} = 1 + ia\cos(\frac{2\pi x}{w}) + \left[ia\cos(\frac{2\pi x}{w})\right]^2 + \left[ia\cos(\frac{2\pi x}{w})\right]^3 + \ldots\ldots\ldots\ldots \tag{3.18}$$

Assuming the magnitude of the substrate error (a) is small, higher orders terms in Equation (3.18) may be ignored. To the first order approximation, the wavefront function u′(x) can be expressed as:

$$u'(x) \cong \left[A_0 + \left(A_1 e^{i\phi} - A_0 \right) \cdot \mathrm{rect}(x) * \frac{1}{b} \mathrm{comb}\left(\frac{x}{b} \right) \right] \cdot \left(1 + ia \cos\left(\frac{2\pi x}{w} \right) \right) \tag{3.19}$$

The far-field diffraction wavefront function, according to the Fraunhofer diffraction integral, is therefore the Fourier transform of wavefront function u′(x):

$$\begin{aligned} U'(\xi) &\cong \left[A_0 \delta(\xi) + \left(A_1 e^{i\phi} - A_0 \right) \cdot \mathrm{sinc}(\xi) \cdot \mathrm{comb}(b\xi) \right] * \left[\delta(\xi) + ia \left[\delta\left(\xi - \frac{1}{w} \right) + \delta\left(\xi + \frac{1}{w} \right) \right] \right] \\ &\cong \left[A_0 \delta(\xi) + \left(A_1 e^{i\phi} - A_0 \right) \cdot \mathrm{sinc}(\xi) \cdot \sum_{m=-\infty}^{+\infty} \delta\left(\xi - \frac{m}{b} \right) \right] * \left\{ \delta(\xi) + ia \left[\delta\left(\xi - \frac{1}{w} \right) + \delta\left(\xi + \frac{1}{w} \right) \right] \right\} \end{aligned} \tag{3.20}$$

where m in the equation corresponds to the diffraction order number.

It is realized from Equation (3.20) that CGH substrate errors affect all diffraction orders equally. For example, using spatial filter, we are able to select zero-oder diffraction beam. The complex amplitude of the zero-order diffraction beam at spatial filter can be expressed as:

$$U'_0(\xi) = A_1 e^{i\phi} \cdot \left\{ \delta(\xi) + ia \left[\delta\left(\xi - \frac{1}{w} \right) + \delta\left(\xi + \frac{1}{w} \right) \right] \right\} \tag{3.21}$$

The inverse Fourier transform of this function is therefore:

$$s(x) = A_1 e^{i\phi} \cdot \left[1 + ia \cos\left(\frac{2\pi x}{w} \right) \right] \tag{3.22}$$

The second term in Equation (3.22) corresponds to the CGH substrate errors. The substrate figure errors can therefore be retrieved this way.

3.3.2. CGH Pattern Distortion

A binary CGH stores both the amplitude and the phase information of the complex wavefronts by controlling positions, width and etching depth of the recorded fringe patterns. Hence, errors in the recorded fringe pattern have direct effects on the accuracy of the reproduced diffraction wavefront. The sources of CGH pattern errors are usually from the limitations in the hologram writer and uncertainties during the replication process.

The effects of the CGH distortion errors can be determined by modeling local areas on a CGH as linear gratings. Linear grating equation in Equation (3.23) can be used to describe the behavior of the grating and the diffracted wavefront function. Constructive interference, bright images, are observed at the observation plane when the condition imposed by Equation (3.24) is satisfied:

$$\begin{aligned} \mathrm{OPD} &= d_0 + d_m \\ &= S \cdot \sin\theta_0 + S \cdot \sin\theta_m \end{aligned} \tag{3.23}$$

$$\mathrm{OPD} = m\lambda \; ; \qquad m = 0, \pm 1, \pm 2, \ldots\ldots\ldots \tag{3.24}$$

where:

d_0, d_m = incident and diffracted path length, see Figure 3.6.

S = grating spacing;

θ_0 = incident beam angle;

θ_m = m^{th} order diffraction beam angle;

λ = wavelength of the incident beam.

In Figure 3.6, optical path difference (OPD) between adjacent slits in the linear grating equals to an integer number of wavelength for a particular diffraction order. For the m^{th} order diffraction beam, the OPD between the neighboring slits is exactly $m\lambda$. A dislocated slit in the grating, however, destroys this relationship. The OPD for beams passing through a dislocated slit and its neighbors will be greater or less than $m\lambda$. The displacement of the slit, or the recorded fringe in CGH, from its ideal position is commonly referred as pattern distortion. Pattern distortion is the dominant type of CGH fabrication error **[Burge 1993]**. CGH pattern distortions produce phase errors in the reproduced diffraction wavefront.

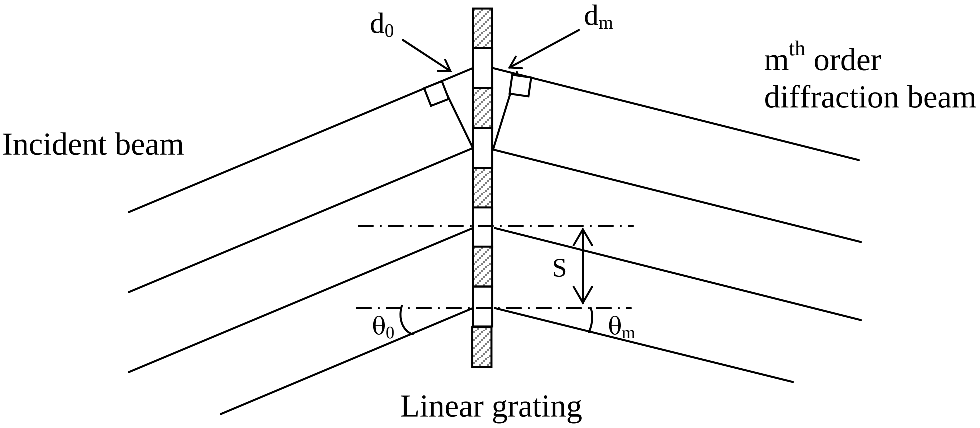

Figure 3.6. Schematic drawing of a linear diffraction grating.

The amount of wavefront phase errors produced by CGH pattern distortions can be expressed as a product of the gradient of the diffracted wavefront function and the pattern distortion vector $\vec{E}(x,y)$ **[Fercher 1976]**:

$$\Delta W(x,y) = -\vec{\nabla} W_{\lambda}(x,y) \cdot \vec{E}(x,y) \qquad (3.25)$$

where:

$\Delta W(x,y)$ = wavefront phase error;

$W_{\lambda}(x,y)$ = diffraction wavefront;

$\vec{\nabla} W_{\lambda}(x,y)$ = gradient of the diffraction wavefront (in the direction that is perpendicular to the fringes);

$\vec{E}(x,y)$ = CGH pattern distortion vector.

In a linear grating hologram, wavefront phase errors produced by pattern distortion is:

$$\Delta W(x,y) = -m\lambda \frac{\varepsilon(x,y)}{S(x,y)} \qquad (3.26)$$

where:

$\varepsilon(x,y)$ = grating position error in direction perpendicular to the fringes;

$S(x,y)$ = localized fringe spacing;

Equation (3.26) shows that wavefront phase errors due to pattern distortions are linearly proportional to the diffraction order number and inversely proportional to the local fringe spacing. Furthermore, CGH pattern distortion errors do not affect the zero-order diffraction beam.

3.3.3. CGH Duty-Cycle Errors

Besides pattern distortions or fringe position errors, variations in both fringe duty-cycle (D) and etching depth (ϕ) are also potential sources of error in CGHs fabrication. In order to study the effects of duty-cycle and phase depth variations on diffracted phase functions, binary linear grating models are used. Diffracted wavefront phase as functions of duty-cycle and phase depth derived in section 3.2.3 are used. Wavefront phase deviations result from one unit variation in grating duty-cycle at different diffraction orders are calculated as:

$m = 0:$

$$\begin{aligned}\frac{\partial \Psi_{m=0}}{\partial D} &= \frac{1}{1+\left[\tan(\Psi)_{m=0}\right]^2}\cdot\frac{\partial \tan(\Psi)_{m=0}}{\partial D} \\ &= \frac{A_0 A_1 \sin\phi}{A_1^2 D^2 + A_0^2 (1-D)^2 + 2A_0 A_1 D(1-D)\cos\phi}\end{aligned} \tag{3.27}$$

$m = \pm 1, \pm 2, \ldots :$

$$\begin{aligned}\frac{\partial \Psi_{m\neq 0}}{\partial D} &= \frac{1}{1+\left[\tan(\Psi)_{m\neq 0}\right]^2}\cdot\frac{\partial \tan(\Psi)_{m\neq 0}}{\partial D} \\ &= \begin{cases} \infty, & \text{for} \quad \sin c(mD) = 0 \\ 0, & \text{otherwise} \end{cases}\end{aligned} \tag{3.28}$$

The deviations of the diffracted wavefront phase values due to variations in either grating duty-cycle or phase depth are defined as the wavefront sensitivity functions. Equation (3.27) and (2.28) give the zero-order and non-zero order wavefront sensitivity functions in terms of grating duty-cycle variations respectively. It is noticed that CGH duty-cycle errors produce wavefront phase errors only in the zero-order diffraction beam; diffraction wavefront phase functions are not sensitive to CGH duty-cycle errors at non-zero diffraction orders.

3.3.4. CGH Etching Depth Errors

Diffraction wavefront phase sensitivities to CGH etching depth variations at different diffraction orders are also determined from Equation (3.15) and (3.16). Equation (3.29) and (2.30) give the zero-order and the non-zero order wavefront sensitivity functions in terms of phase depth variations.

$$\begin{aligned} \mathrm{m}=0: \quad & \\ \frac{\partial\Psi_{\mathrm{m}=0}}{\partial\phi} &= \frac{1}{1+\left[\tan(\Psi)_{\mathrm{m}=0}\right]^2}\cdot\frac{\partial\tan(\Psi)_{\mathrm{m}=0}}{\partial\phi} \\ &= \frac{A_1^2D^2 + A_0A_1D(1-D)\cos\phi}{A_1^2D^2 + A_0^2(1-D)^2 + 2A_0A_1D(1-D)\cos\phi} \end{aligned} \qquad (3.29)$$

$m = \pm 1, \pm 2, \ldots :$

$$\frac{\partial \Psi_{m\neq 0}}{\partial \phi} = \frac{1}{1+\left[\tan(\Psi)_{m\neq 0}\right]^2} \cdot \frac{\partial \tan(\Psi)_{m\neq 0}}{\partial \phi} \tag{3.30}$$

$$= \frac{A_1^2 - A_0 A_1 \cos\phi}{A_1^2 + A_0^2 - 2A_0 A_1 \cos\phi}$$

The wavefront sensitivity functions (Equation (3.27) through Equation (3.30)) provide insights of CGH fabrication errors and their effects on diffraction wavefront phase values. Using the wavefront sensitivity functions, we are able to identify the most and the least sensitive hologram structures, duty-cycle and phase depth, to fabrication uncertainties. The information may also be used to exercise error budget and analysis for applications using CGH. It is extremely valuable to the design and fabrication practices of computer-generated hologram.

In the following sections, we are going to evaluate two types of binary gratings: chrome-on-glass grating and phase grating. Wavefront sensitivity functions for both types of gratings are studied based on the analytical solutions derived in this section. The grating models described are assumed to operate in reflection modes.

3.4. NUMERICAL SIMULATION OF PHASE GRATING

Phase gratings modulate only the phase function of the incident wavefront. They are typically produced by etching the grating patterns onto a bare glass substrate. A drawing that shows the surface relief function of a typical phase grating is given in Figure 3.7.

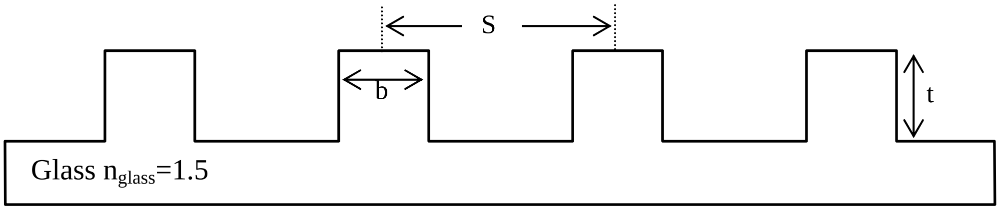

Figure 3.7. Schematic drawing of a phase grating surface profile.

In our study, the grating substrate is assumed to have an index of refraction of 1.5. The binary linear grating model introduced in the previous section is employed for the analysis. The coefficients A_0, A_1, and ϕ in Equation (3.2) are determined using Fresnel equations and $A_0 = A_1 = 0.2$. The phase function ϕ for the grating in reflection mode is calculated as:

$$\begin{aligned} \phi &= \left[\frac{2\pi}{\lambda}(2t) + \pi\right] - \pi \\ &= \frac{4\pi}{\lambda} t \end{aligned} \tag{3.31}$$

3.4.1. Diffraction Efficiency

Diffraction efficiencies of the phase grating at different diffraction orders are calculated using Equation (3.10) and (3.11). The results are shown in Figure 3.8 through Figure 3.12. Figure 3.8 shows the diffraction efficiency of the zero-order beam as a function of both duty-cycle and phase depth in a 3-D coordinate. As demonstrated in the diagram, the diffraction efficiency function is symmetrical about the 50% duty-cycle and half-wave phase depth point.

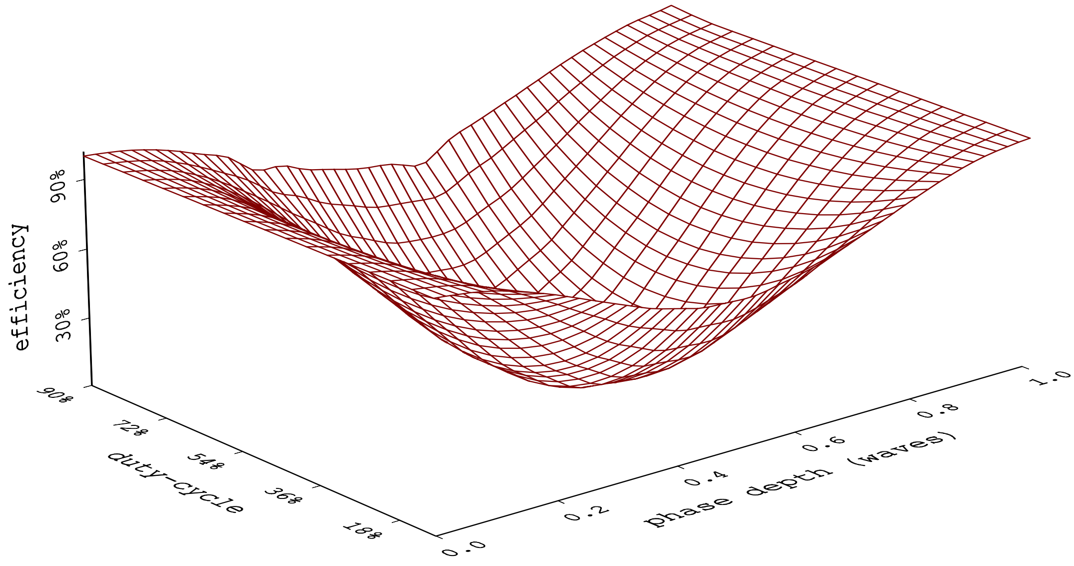

Figure 3.8. Diffraction efficiency of phase grating as a function of grating duty-cycle and phase depth for zero-order diffraction beam.

Figure 3.9 and Figure 3.10 show the cross-section profile plots of the diffraction efficiency function. Figure 3.9 shows that the diffraction efficiency function with

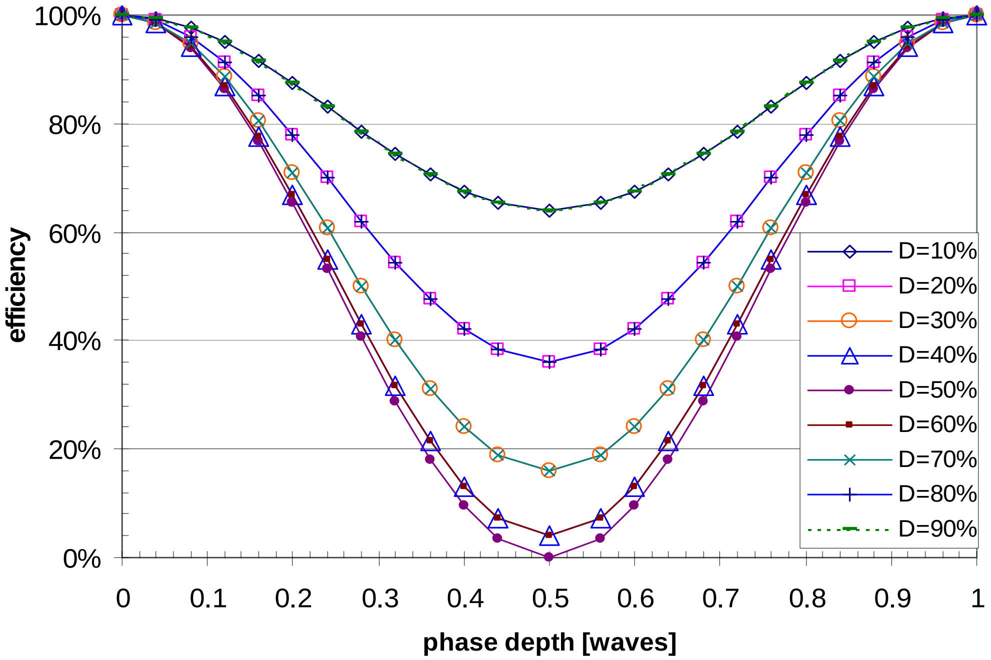

Figure 3.9. Diffraction efficiency of a phase grating as a function of phase depth for the zero-order diffraction beam for nine duty-cycle values.

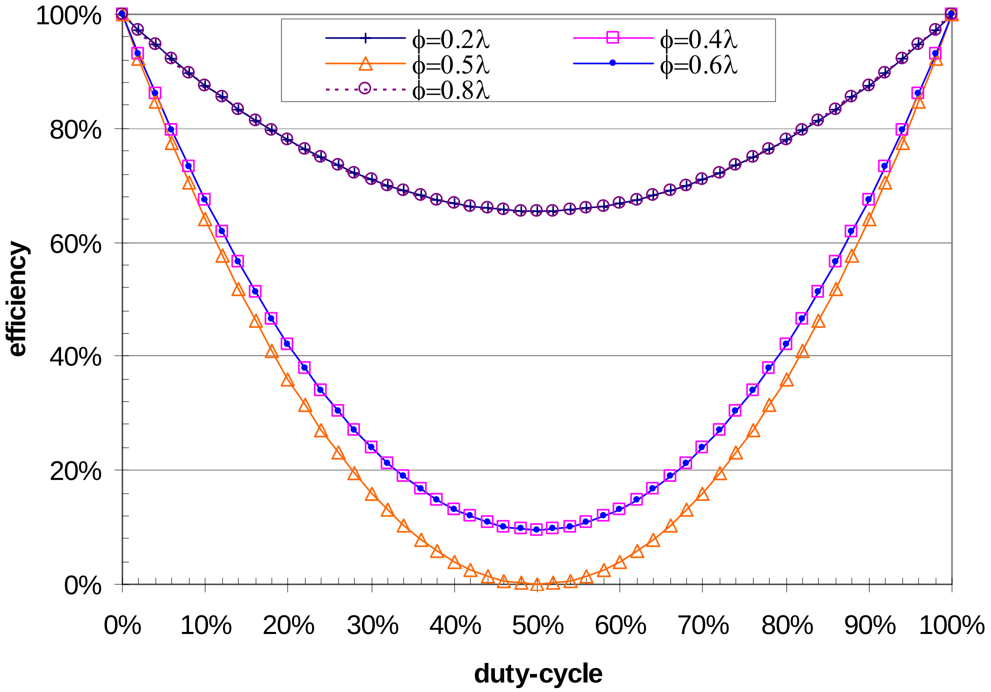

Figure 3.10. Diffraction efficiency of a phase grating as a function of duty-cycle for the zero-order diffraction beam for five phase depth values.

different duty-cycles reach the minimum value when the phase depth is λ/2. Figure 3.10 shows that phase gratings with 50% duty-cycle have the minimum diffraction efficiency regardless of the grating phase depth.

For the non-zero diffraction orders, the diffraction efficiency functions are also symmetrical about the 50% duty-cycle and the half-wave phase depth points (Figure 3.11 and Figure 3.12). Figure 3.11 gives the relationship between diffraction efficiency for non-zero order beams and duty-cycle. It shows that diffraction efficiency of the non-zero order beams vary periodically with changes in the grating duty-cycle for phase gratings with λ/2 phase depth. In addition, the number of times that maximum efficiency values are reached for each diffraction beam equals to the diffraction order number of beam.

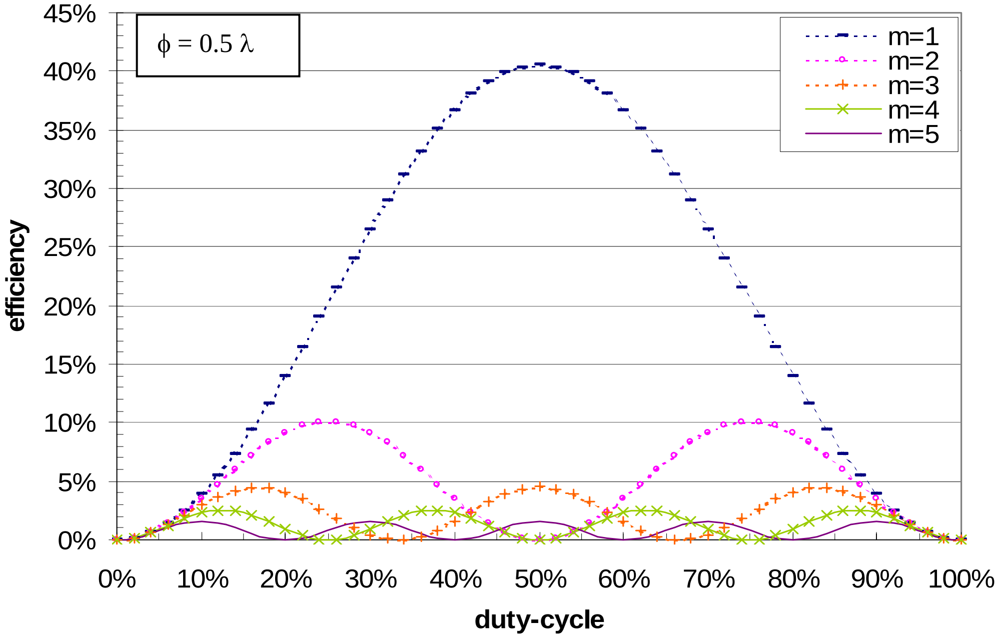

Figure 3.11. Diffraction efficiency of a phase grating as a function of duty-cycle for non-zero order diffraction beams with 0.5λ phase depth.

Figure 3.12 illustrates the diffraction efficiency values for the non-zero order beams as a function of phase depth variations. Phase gratings with a 50% duty-cycle produce maximum efficiency at λ/2 phase depth for all non-zero order beams.

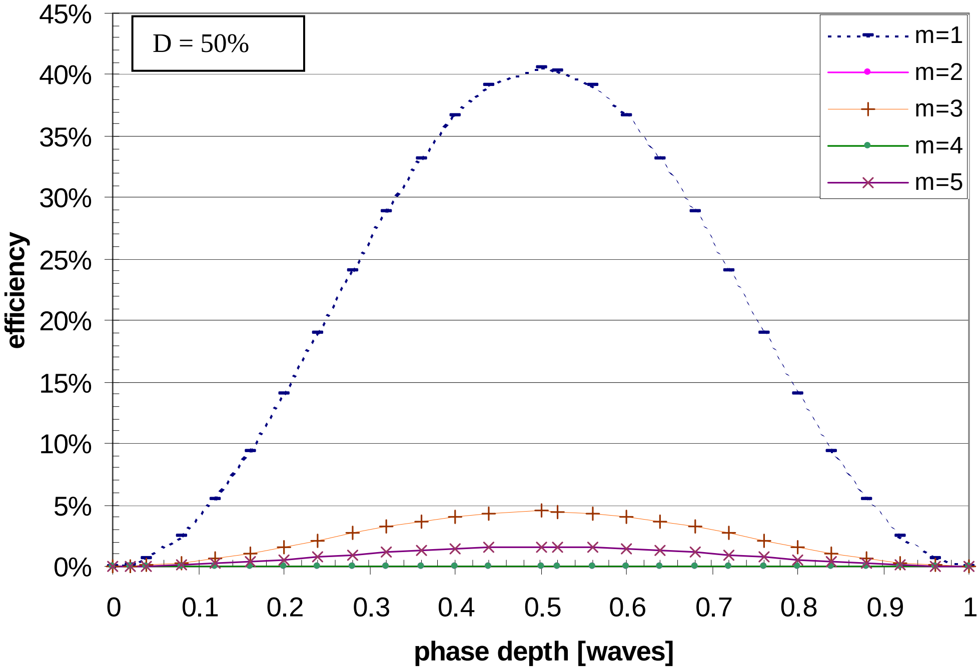

Figure 3.12. Diffraction efficiency of a phase grating as a function of phase depth for non-zero order diffraction beams at 50% duty-cycle.

3.4.2. Wavefront Phase

Diffraction wavefront phase functions for phase gratings are calculated using Equation (3.15) and Equation (3.16) for different diffraction orders. Diffraction wavefront phase values as functions of grating phase depth and duty-cycle for the zero-order (m=0) diffraction beam are shown in Figure 3.13 through Figure 3.21. Figure 3.13 displays the zero-order diffracted wavefront phase functions as a function of phase depth and duty-cycle in a 3-D coordinate. A phase discontinuity is observed along the 50% duty-cycle line for the zero-order beam at the half-wave phase depth point. This phase discontinuity may be better observed in Figure 3.14.

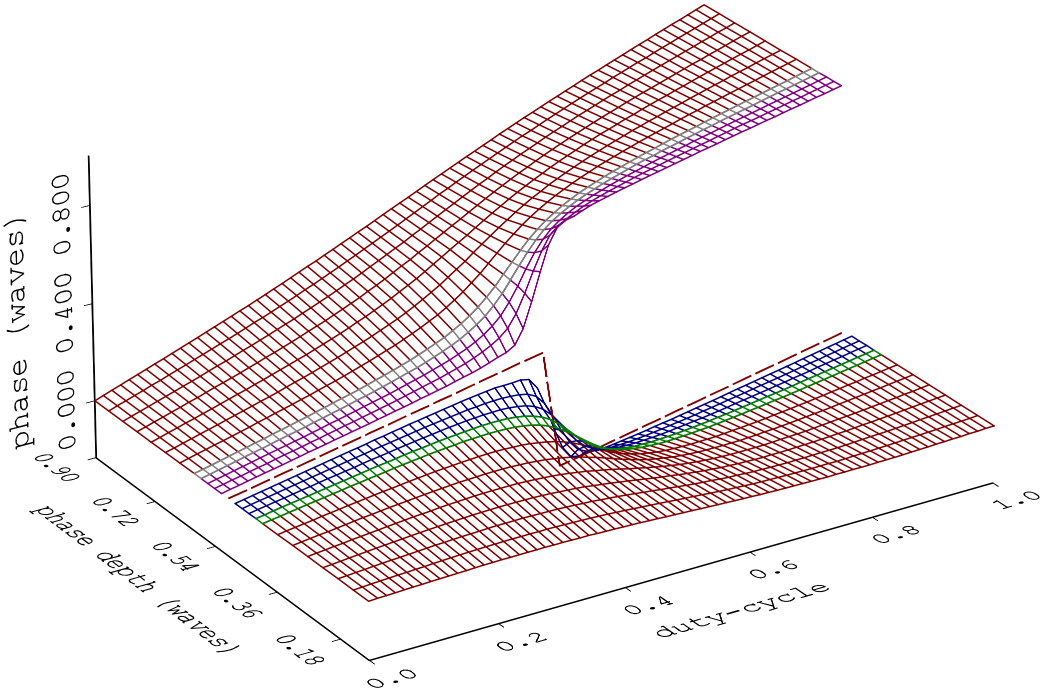

Figure 3.13. Diffraction wavefront phase values of a phase grating as a function of grating phase depth and duty-cycle for the zero-order diffraction beam.

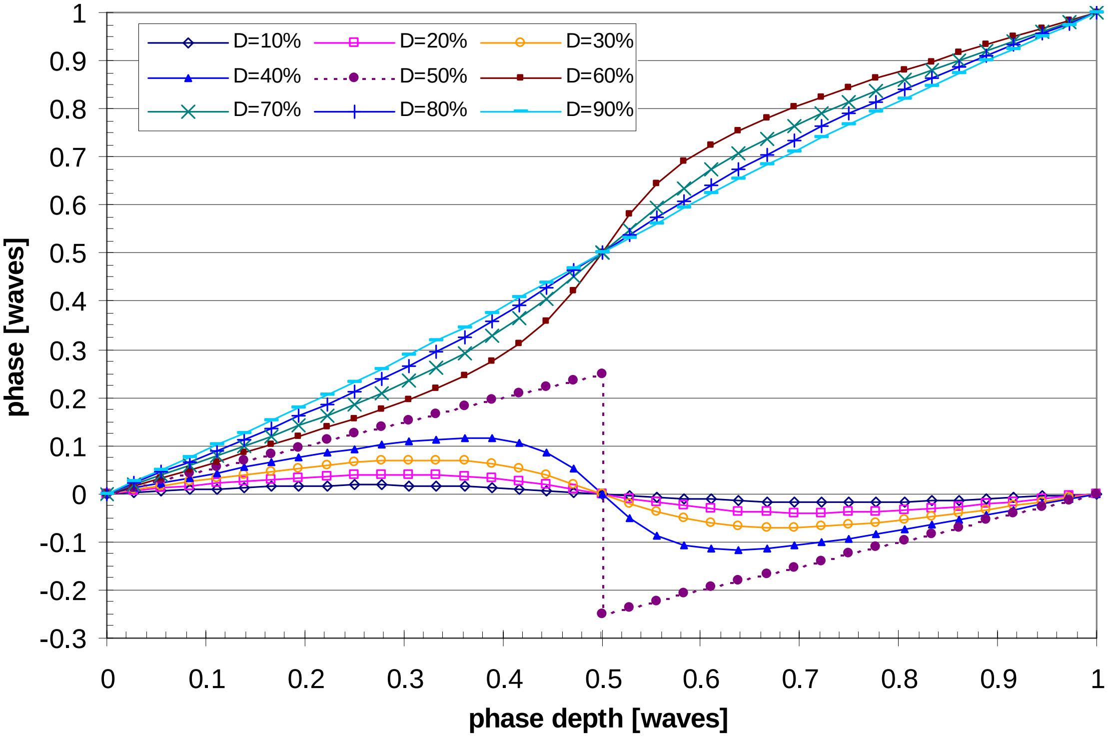

Figure 3.14. Wavefront phase vs. phase depth for a phase grating in the zero diffraction order.

As shown in the figure above, the diffracted phase values of all duty-cycle values appear continuous as the function of phase depth except for the 50% duty-cycle. The occurrence of discontinuity in phase for 50% duty-cycle at $\lambda/2$ phase depth is anomalous. It implies a phase reversal in the diffracted wavefront when grating phase depth varied through the $\lambda/2$ phase depth point. It also indicates a high sensitivity of the wavefront phase function in zero diffraction order to phase depth fabrication errors for gratings with a 50% duty-cycle and a $\lambda/2$ phase depth. More discussions on this phase discontinuity are given in section 3.5 using the complex fields representation.

Diffraction wavefront phase sensitivities to fabrication errors for phase gratings are studied using the wavefront phase sensitivity function from Equation (3.29). Figure 3.15 shows the wavefront phase deviations in the zero diffraction orders beam produced by one unit grating phase depth variation for phase gratings with different duty-cycles.

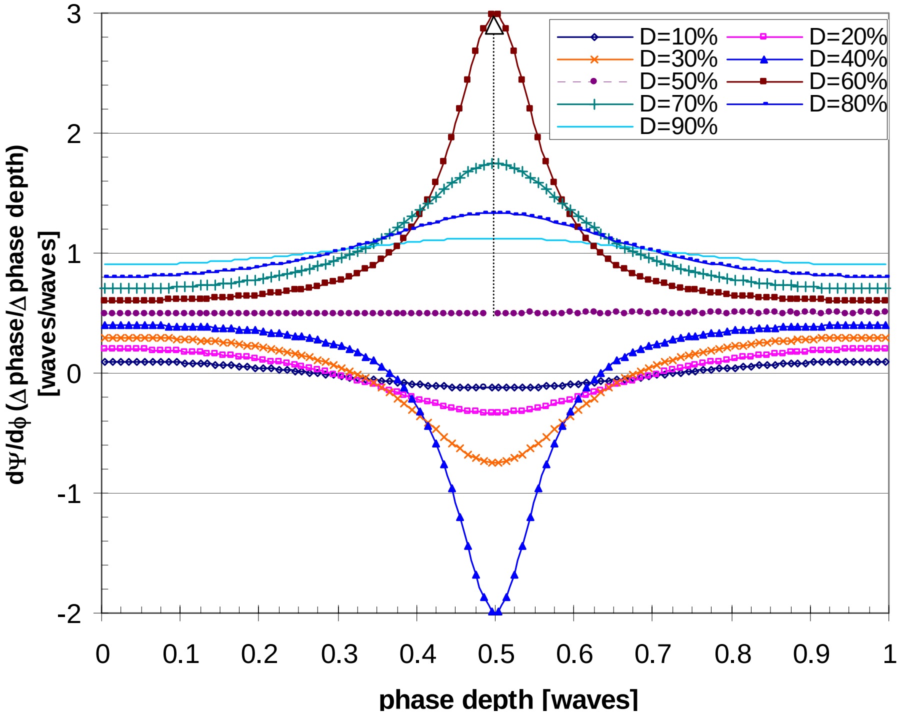

Figure 3.15. Wavefront phase sensitivity of a phase grating to grating phase depth variation for the zero-order beams for various duty-cycle values.

A 0.1λ phase depth error will produce a -0.075λ wavefront phase error for phase gratings with a 30% duty-cycle and a nominal phase depth of 0.5λ. The same phase depth error (0.1λ) produces $+0.03\lambda$ wavefront phase error for phase gratings with a 30% duty-cycle and a nominal phase depth value of 0.1λ. It is also realized that phase gratings with 50% duty-cycle is extremely to phase depth variations at a 0.5λ nominal phase depth.

Using Figure 3.15, we are able to identify grating structures that are the most or the least subject to phase depth errors. All data points in Figure 3.15 where $d\Psi_{m=0}/d\phi = 0$ represent grating structures that are not sensitive to phase depth variations. Figure 3.16 shows the complete solutions of all possible phase depths and duty cycle(s) combinations for phase gratings that are not subject to phase depth errors in the zero-order diffraction wavefront.

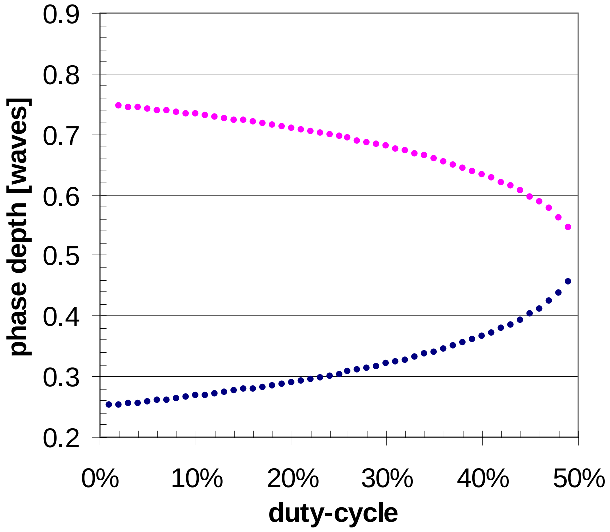

Figure 3.16. Phase depths and duty-cycle(s) combinations of phase gratings that are not sensitive to phase depth variations ($d\Psi_{m=0}/d\phi = 0$) for the zero-order beam.

Figure 3.17 shows the corresponding diffraction efficiencies for the gratings in Figure 3.16. As shown from the plot that the diffraction efficiency values of the zero-order diffraction beam decreases linearly with increasing in grating duty-cycle values.

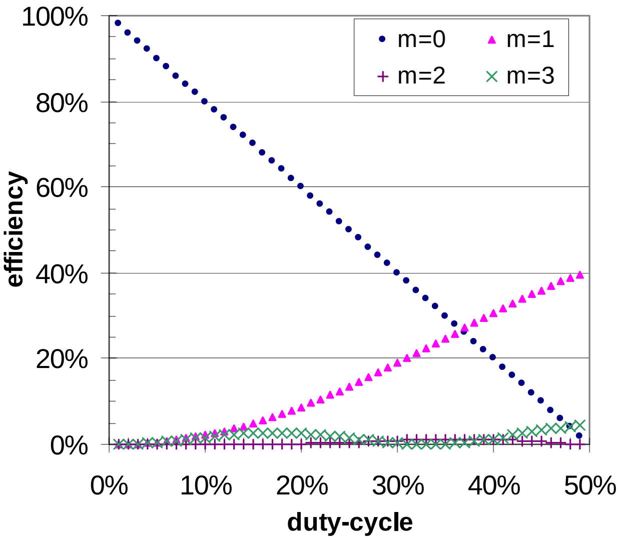

Figure 3.17. Diffraction efficiency values for phase gratings given in Figure 3.16 that are not sensitive to phase depth errors for the zero-order beam.

Figure 3.18 shows the phase values for the zero-order beam as functions of grating duty-cycle variations. Figure 3.19 shows the wavefront phase sensitivity function with variations in grating duty-cycle. The plot indicates that a 1% duty-cycle variation will result in a –0.004 waves phase error in the zero-order diffraction wavefront for phase gratings with a 30% duty-cycle and a 0.6 waves nominal phase depth.

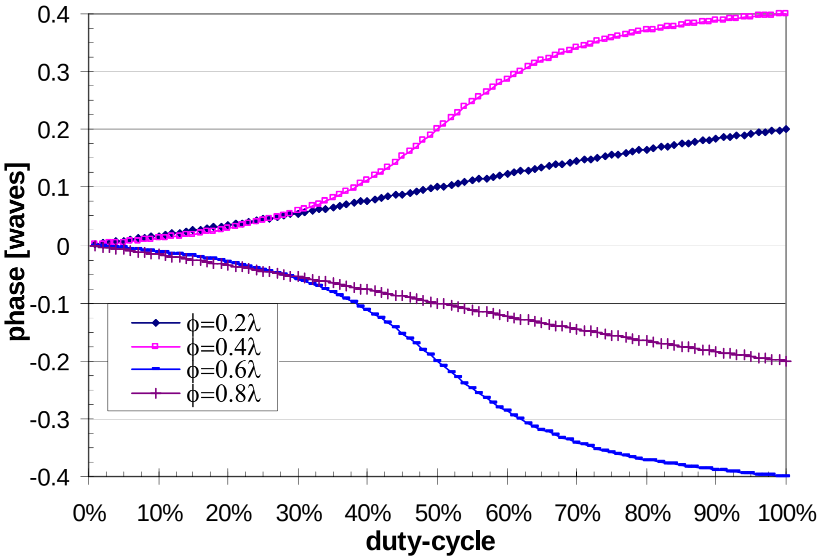

Figure 3.18. Wavefront phase vs. duty-cycle for the zero-order diffraction beam of a phase grating.

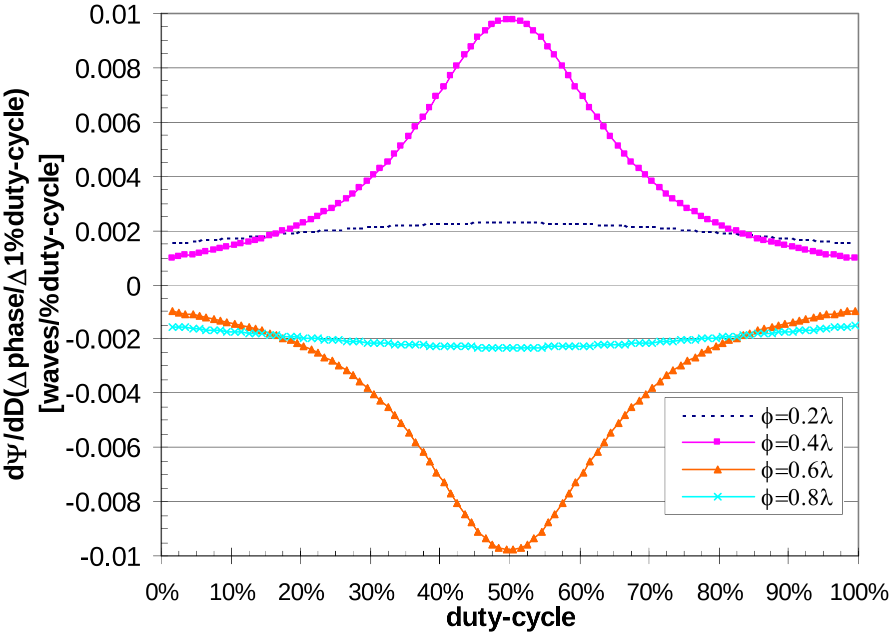

Figure 3.19. Wavefront phase sensitivity of a phase grating to grating duty-cycle variation for zero-order beam for various phase depth values.

Diffracted wavefront phase functions, calculated from Equation (3.16), for non-zero order beams ($m \neq 0$) are shown in both Figure 3.20 and Figure 3.21. Figure 3.20 gives the relationship between the diffracted wavefront phase functions and the grating phase depth for all non-zero order beams. It is shown that the wavefront phase functions vary linearly with the grating phase depth; and the dependence of diffracted wavefront functions on variation of phase depth errors is constant.

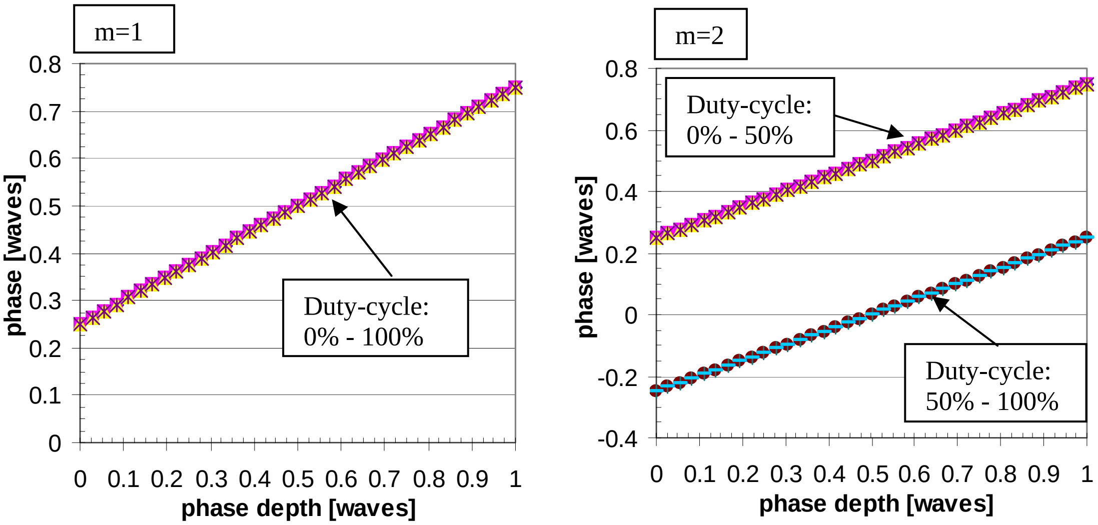

Figure 3.20. Wavefront phase vs. grating phase depth for the 1st-order and the 2nd-order diffraction beam for all grating duty-cycle values from phase gratings.

Figure 3.21 shows the relationship between wavefront phase values and duty-cycle for non-zero order beams. It is noticed that wavefront phase functions exhibit λ/2 discontinuities for higher than 1st diffraction orders (m>1). A λ/2 phase discontinuity is observed at the 50% duty-cycle point for the 2nd order diffraction beam. Two λ/2 phase steps are seen for the 3rd order diffraction beam at 33.3% and 66.6% duty-cycle points.

This characteristic of the phase function is the direct result of the sign changes of the sinc(mD) function in Equation (3.16). The alteration between positive and negative values of the sinc function causes the calculated phase values to change by +/-π radians. The number of phase discontinuities occurs in the phase function, or number of sign changes for sinc(mD), when grating duty-cycle is varied from 0% to 100%, equals to the diffraction order number minus one.

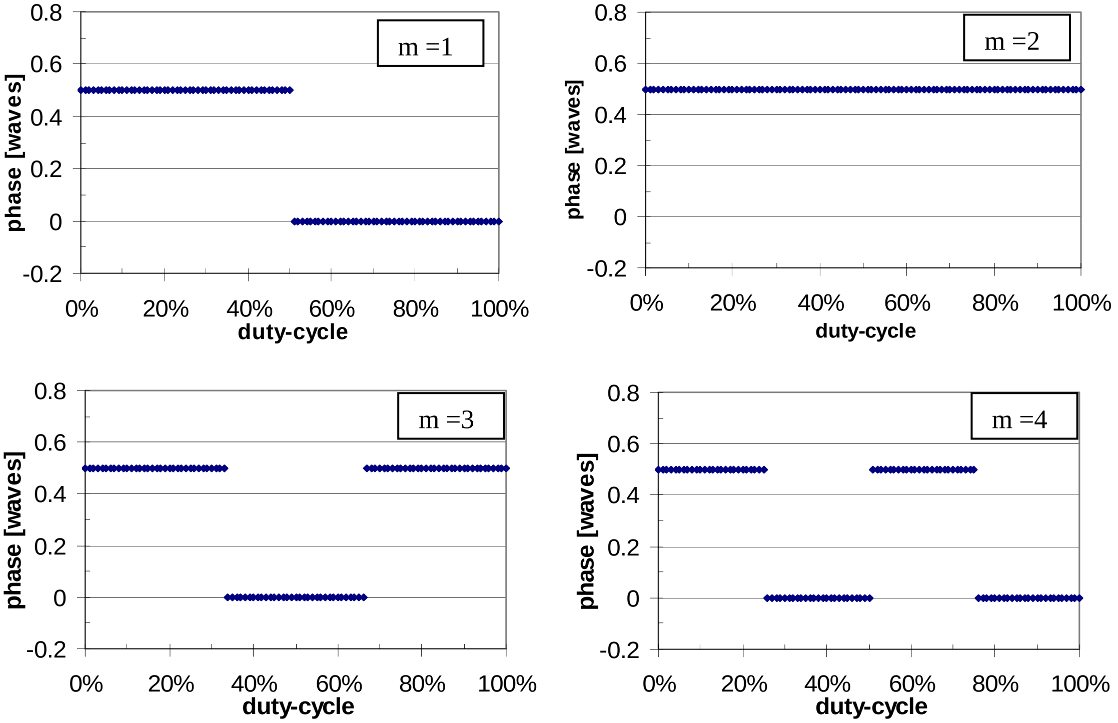

Figure 3.21. Wavefront phase vs. grating duty-cycle for non-zero diffraction orders at 0.5 waves phase depth from a phase grating.

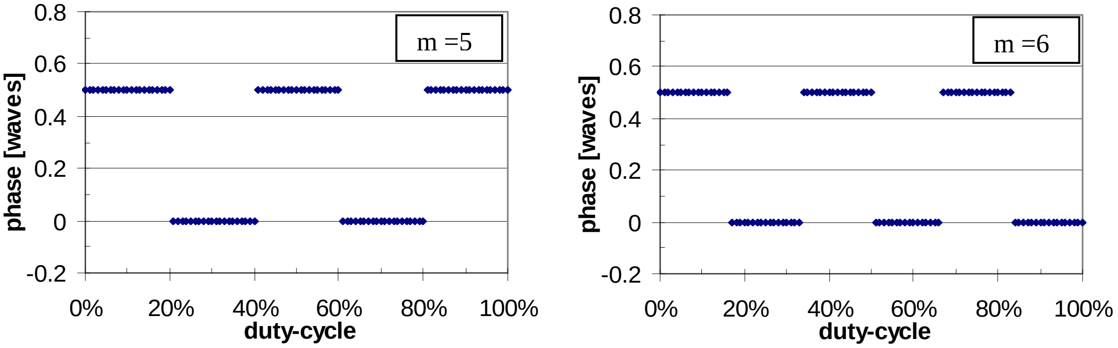

Figure 3.21. (continued) Wavefront phase vs. grating duty-cycle for non-zero diffraction orders at 0.5 waves phase depth from a phase grating.

Figure 3.21 also indicates that wavefront phase functions are not affected by duty-cycle variations in phase gratings for all non-zero diffraction orders. In other words, duty-cycle errors may be ignored for phase grating applications where only non-zero order phase function is of concern. This phenomenon has been predicted in theory by Equation (3.28).

3.5. GRAPHICAL REPRESENTATION OF DIFFRACTION FIELD

A graphical representation of the complex diffraction field can be obtained by plotting the real and the imaginary parts of the diffraction wavefront in the complex coordinates. Figure 3.22 gives a graphical illustration of the solution of the zero-order diffraction field for a phase grating with 40% duty-cycle.

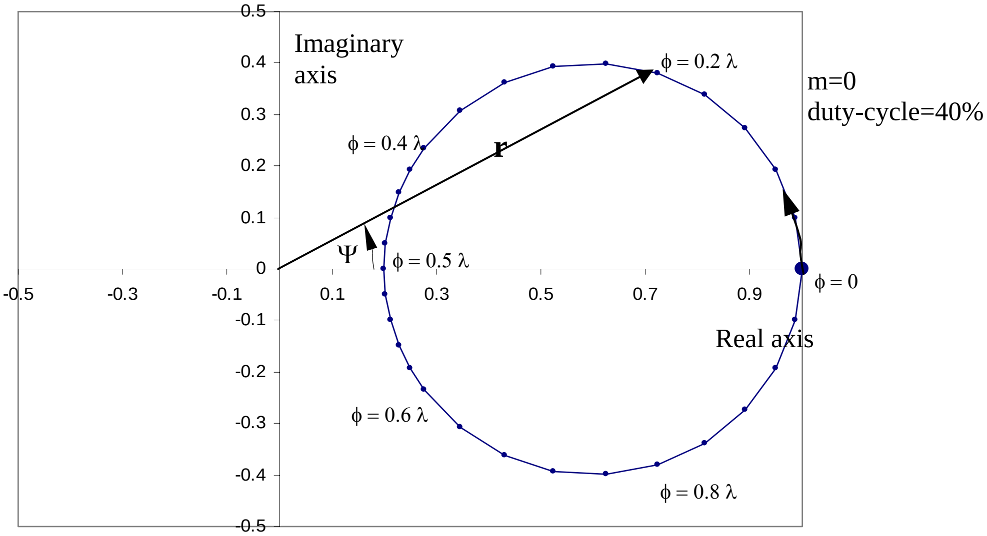

Figure 3.22. Graphical representation of the complex diffraction wavefront produced by a phase grating with 40% duty-cycle for the zero-order beam.

The circle in the plot gives the complete solution to the diffraction fields produced by the grating at a specific diffraction order. Each point in the circle corresponds to different values of grating phase depth. A vector (**r**) pointing from the origin of the complex coordinate to a point on the circle corresponds to a solution of the diffraction fields produced by the grating at a specific phase depth. As the grating phase depth increases, the solution point travels along the circle in the counter-clockwise direction that is indicated by the arrow along the circle. The magnitude of the vector (**r**) gives the amplitude of the diffraction field; while the angle between the vector (**r**) and the real axis gives the phase value (Ψ) of the diffraction field. As an example, in Figure 3.22, the vector **r** is pointing to the $\phi=0.2\lambda$ point on the circle. This point corresponds to the zero-order diffraction beam of a phase grating with 40% duty-cycle and 0.2 waves phase depth. The magnitude of the vector is 0.82 and the corresponding efficiency is $\eta = 0.82^2$

= 67%. The angle between vector **r** and the real axis is approximately 28^o which gives a wavefront phase value of $\phi = 28^o/360^o = 0.077\lambda$.

Figure 3.23 shows the diffraction wavefront solution at zero diffraction order for a phase grating with different duty-cycle values. Figure 3.23 contains the same amount of information on the diffraction wavefront functions that Figure 3.9 and Figure 3.14 combined.

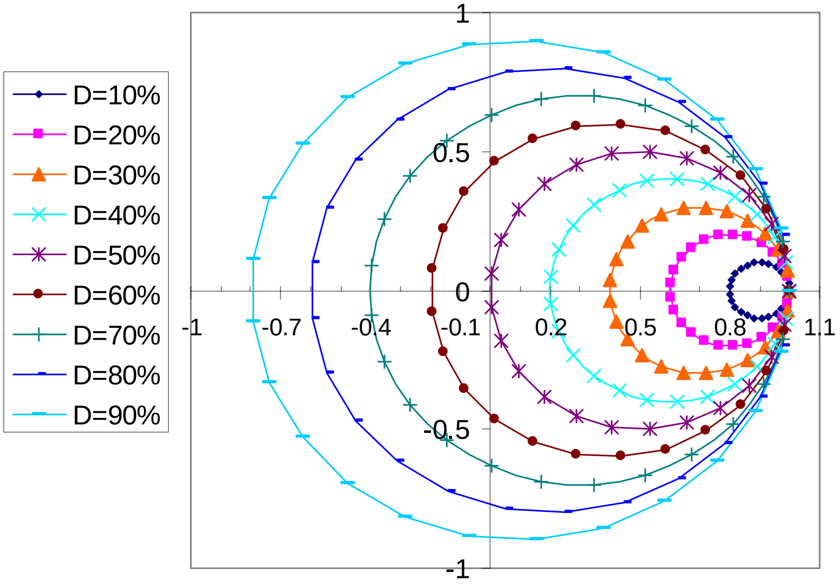

Figure 3.23. Graphical representation of the complex diffraction fields in the zero diffraction order produced by a phase grating with nine duty-cycle values.

Recall Figure 3.14, a phase discontinuity was observed for the zero-order diffraction beam along the 50% duty-cycle line at $\lambda/2$ phase depth. The explanation of the phase discontinuity was not obvious from the derived equations. It may however by be explained directly using the complex field representation. Figure 3.24 shows the solution of the complex diffraction field of the zero-order beam at

50% duty-cycle with the grating phase depth varied from 0 to 1 wave. The zero phase depth point is located on the real axis one unit away from the origin. As the phase depth increases, the solution points travels counter-clockwise along the circle. It passes through the origin when the phase depth equals to λ/2, where the angle of the vector (**r**) varies abruptly from +90 degree to –90 degree, or the phase value of the wavefront displays a π phase change. At this point, the diffraction efficiency of the grating is zero. Therefore, the apparent discontinuity in phase (see Figure 3.14) is actually continuous transition for the complex field.

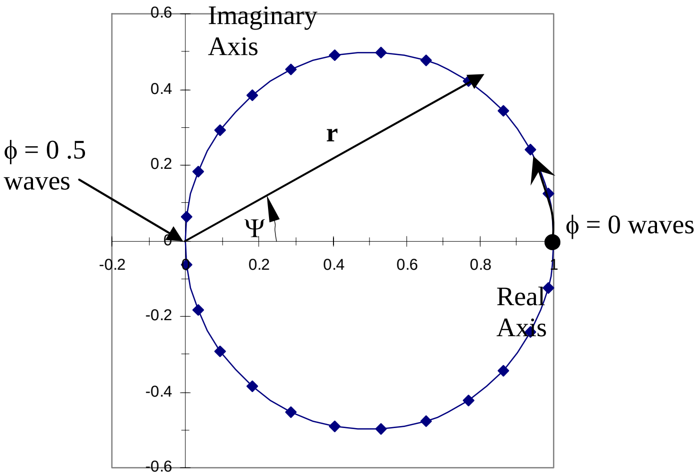

Figure 3.24. Graphical representation of the complex diffraction fields in the zero diffraction order produced by a phase grating with 50% duty-cycle.

Figure 3.25 shows the graphical representations of the complex diffraction fields for both zero and non-zero diffraction orders. Figure 3.26 combines all plots in Figure 3.25 in a 3-D space with an additional axis of grating duty-cycle.

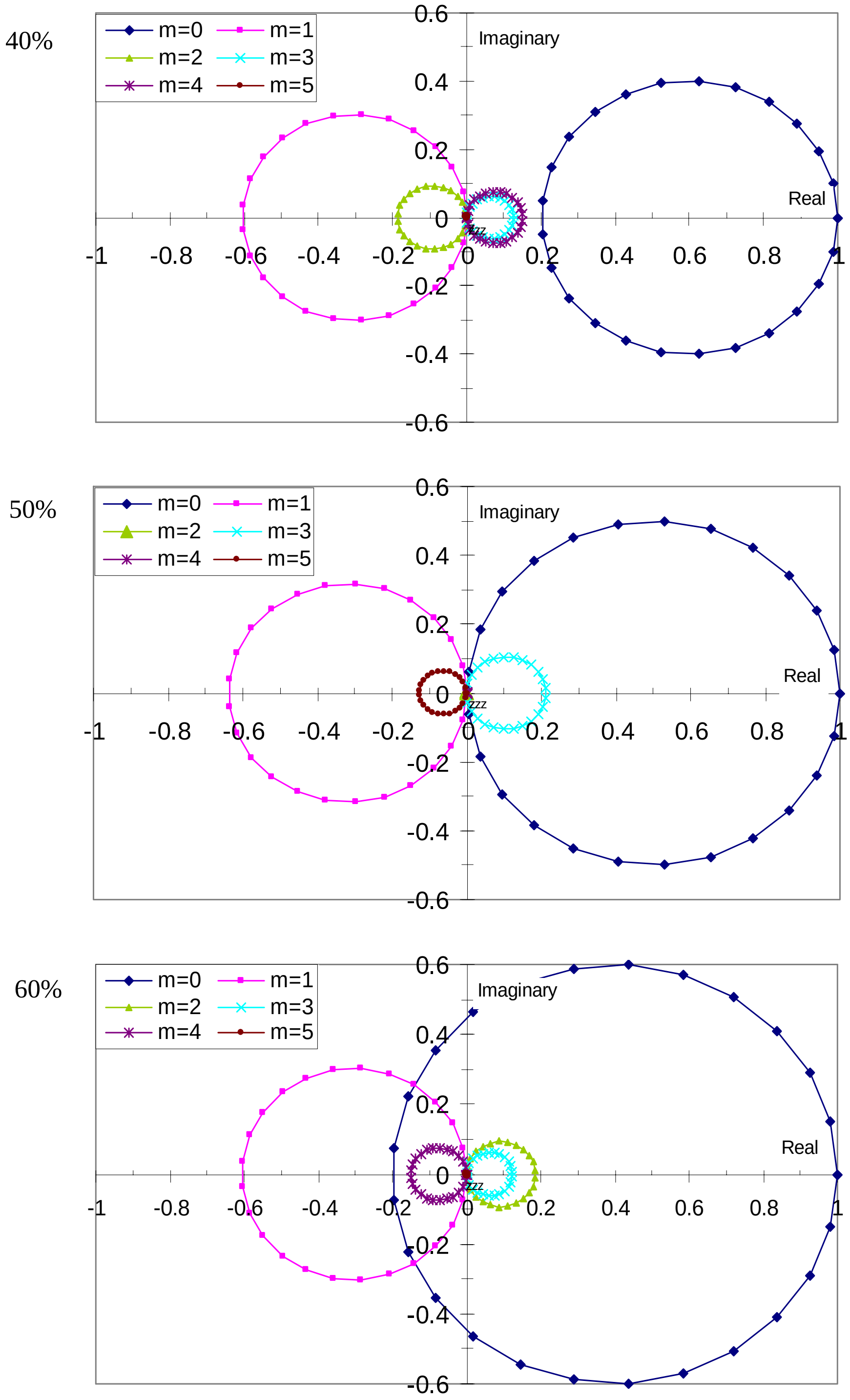

Figure 3.25. Graphical representations of the complex diffraction fields at various diffraction orders for gratings with different duty-cycles.

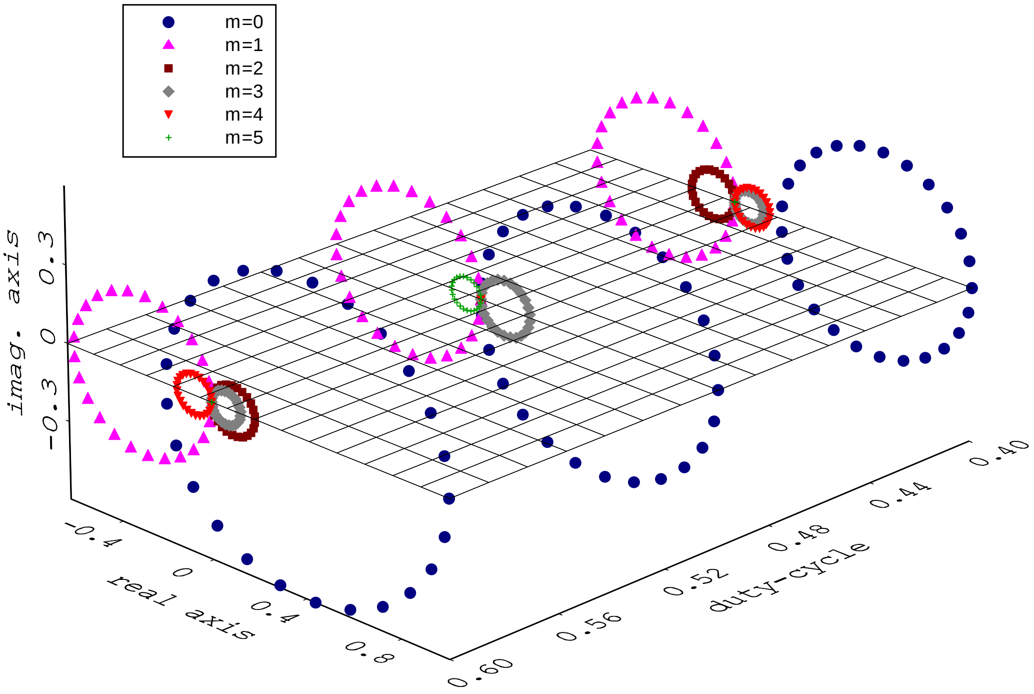

Figure 3.26. 3-D complex diffraction fields illustration of Figure 3.25. (from left to right: D = 60%, 50%, and 40%).

3.6. NUMERICAL SIMULATION OF CHROME-ON-GLASS GRATINGS

A chrome-on-glass grating consists of a flat glass substrate and a thin chrome coating with grating pattern written on it. A schematic drawing of the structure of a linear chrome-on-glass grating is shown as following:

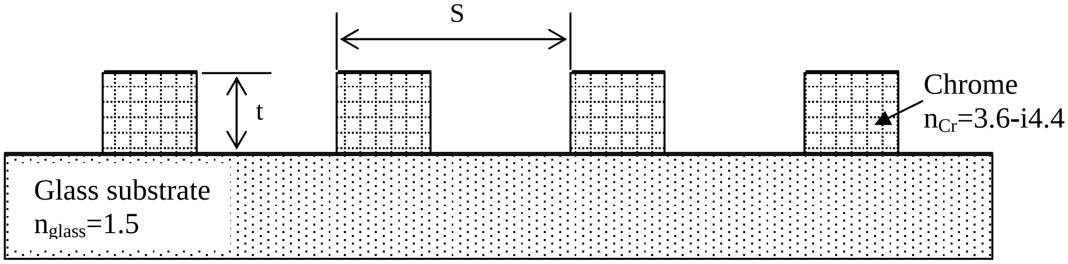

Figure 3.27. Schematic drawing of a chrome-on-glass grating.

Chrome has a complex value of index of refraction of 3.6-i4.4 at λ = 633 nm **[Lynch and Hunter 1991]**. The binary linear grating model is again used in this study and the complex amplitude functions A_0 = 0.2, A_1 = 0.8, and phase $\phi = \frac{4\pi}{\lambda} t - 0.0879\pi$.

A complete model of thin metal coating grating must include the effects of multiple reflections inside the metal layer **[Born and Wolf 1980]**. Figure 3.28 shows the calculated amplitude and phase values of the multiple reflection beam off the chrome layer as a function of the chrome thickness. The values of the amplitude and the phase functions stay constant when the chrome thickness is greater than 50 nm. This result indicates that the effects of multiple reflections in the chrome layer may be neglected for chrome coating over 50 nm thick. In our diffraction analysis, the chrome layer is modeled to have a thickness that is greater than 50 nm to eliminate multiple reflections effects.

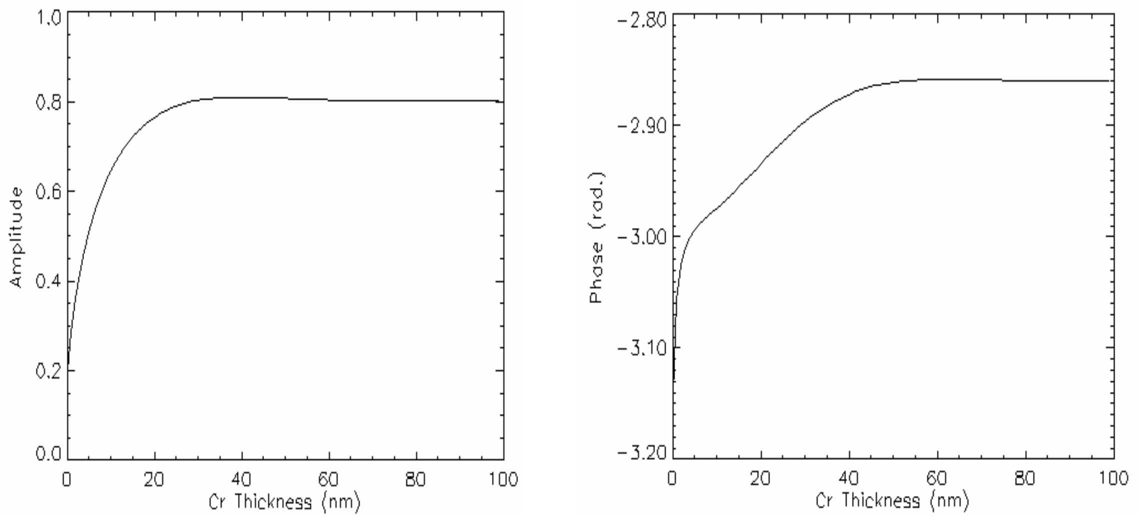

Figure 3.28. Reflectance amplitude and phase functions calculated for multi-reflection beams from a thin chrome coating at difference thickness.

3.6.1. Diffraction Efficiency

Equation (3.10) and (3.11) are used to calculate the diffraction efficiency values for the chrome-on-glass grating, as shown in Figure 3.29, 3.29, and 3.31. For the zero-order diffraction beam (*m=0*), the diffraction efficiency functions increases non-monotonically with duty-cycle (Figure 3.29). The diffraction efficiency decreases linearly as the chrome thickness increases (Figure 3.30).

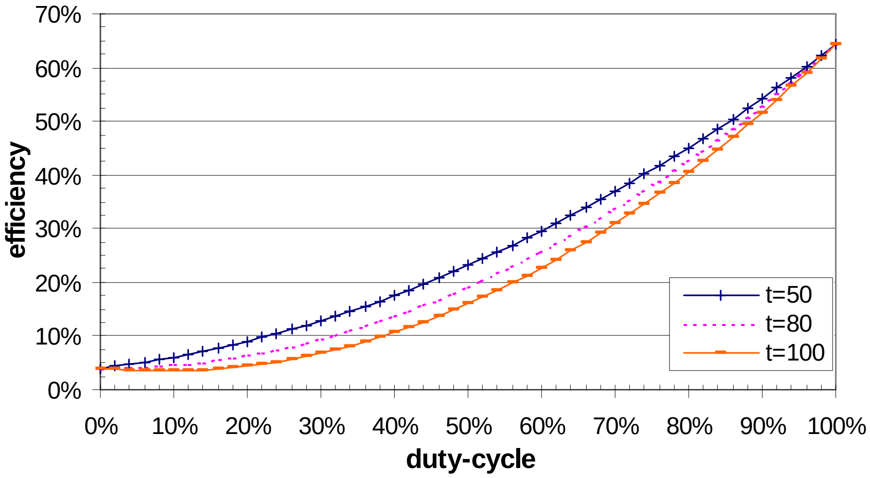

Figure 3.29. Diffraction efficiency for zero-order beam vs. duty-cycle for chrome-on-glass gratings with different chrome thicknesses.

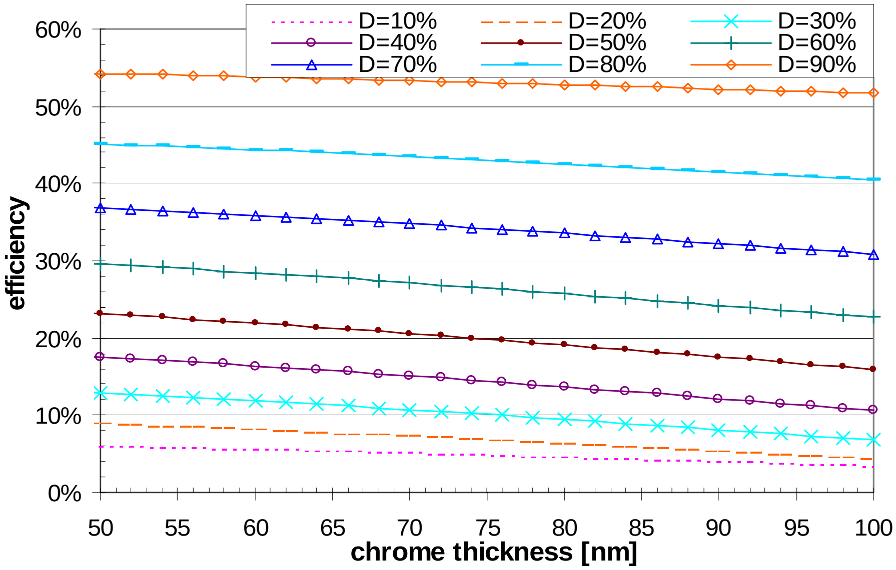

Figure 3.30. Diffraction efficiency for zero-order beam vs. chrome thickness for chrome-on-glass gratings at various grating duty-cycles.

Diffraction efficiency values for non-zero order beams ($m \neq 0$) vary periodically with changes in the grating duty-cycle for chrome-on-glass gratings, as shown in Figure 3.31. The number of times that maximum efficiency value are obtained for each diffraction beam equals to its order number. The 1st order diffraction beam achieves the maximum diffraction efficiency at 50% duty-cycle.

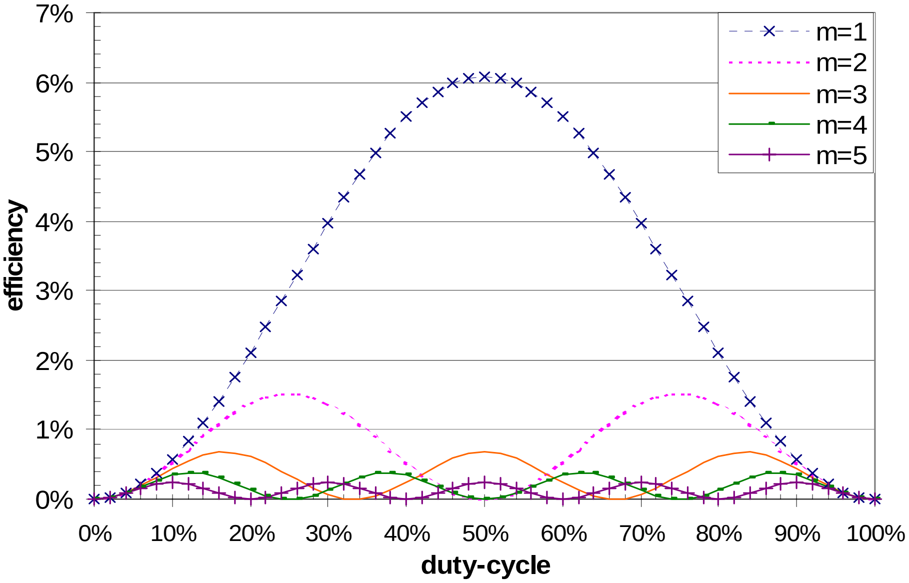

Figure 3.31. Diffraction efficiency for non-zero diffraction orders vs. duty-cycle for a chrome-on-glass grating with 80 nm chrome thickness.

3.6.2. Wavefront Phase

Wavefront phase values for all diffraction orders are calculated using Equation (3.15) and Equation (3.16). Diffraction wavefront phase as functions of grating duty-cycle and chrome thickness for the zero-order (*m=0*) diffraction beam are shown in Figure 3.32 through 3.37. Figure 3.32 displays the relationship among zero-order wavefront phase values, chrome thickness and duty-cycle in a 3-D coordinate. Figure 3.33 shows the diffracted phase verse grating duty-cycle. Figure 3.34 shows the diffracted phase in terms of chrome thickness.

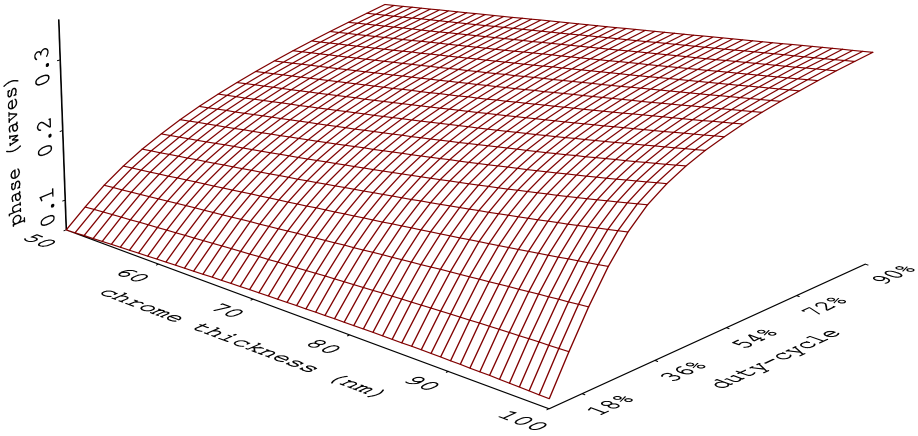

Figure 3.32. Wavefront phase for the zero-order beam vs. duty-cycle and chrome thickness for chrome-on-glass grating.

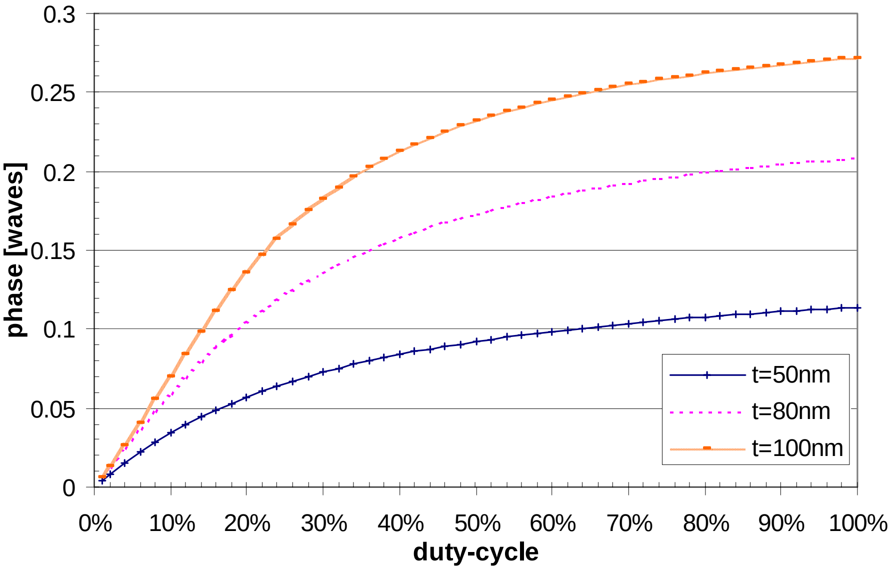

Figure 3.33. Wavefront phase for the zero-order beam vs. duty-cycle for chrome-on-glass gratings with different chrome thicknesses.

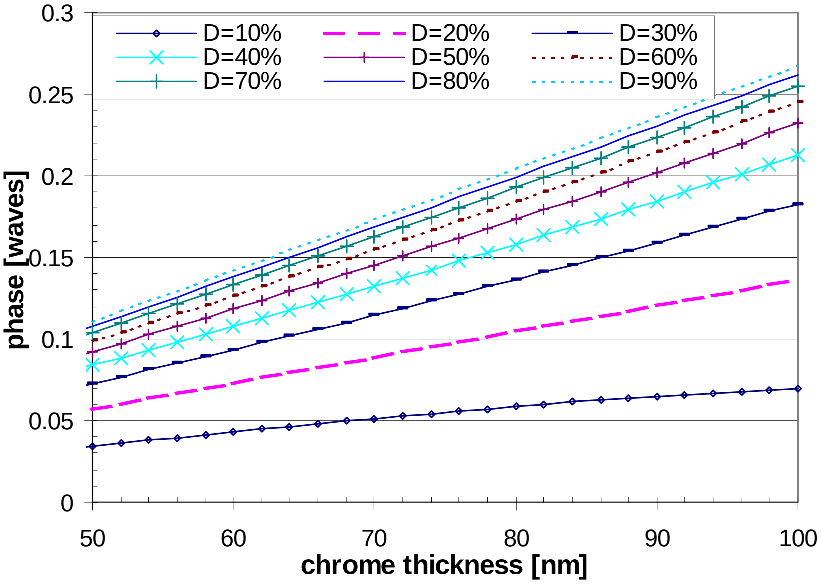

Figure 3.34. Wavefront phase for the zero-order beam vs. chrome thickness for chrome-on-glass gratings with various duty-cycles.

Wavefront phase sensitivity functions for the zero-order diffraction beam are calculated for the chrome-on-glass grating. Figure 3.35 shows the deviations in phase values with 1% duty-cycle variation for gratings with different chrome thickness.

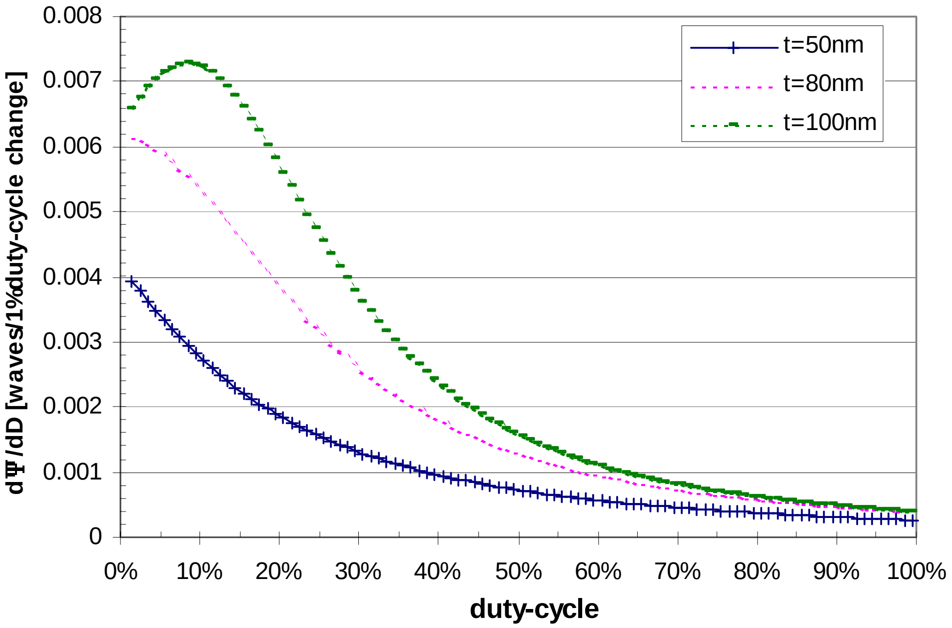

Figure 3.35. Wavefront phase sensitivity function to 1% duty-cycle variation in the zero-order beam for chrome-on-glass gratings with different chrome thicknesses.

Using the wavefront phase sensitivity plot, we are able to estimate the amount of potential wavefront phase errors that may be resulted from the uncertainties in the manufacturing process. For example, a 1% error in the grating duty-cycle produces a 0.0055 waves phase deviation in the diffraction wavefront for a chrome-on-glass grating with a 10% nominal duty-cycle and a 80 nm chrome thickness. Figure 3.35 also shows that the phase sensitivity function reaches its maximum value at approximately 10% duty-cycle point for chrome-on-glass gratings with 100 nm chrome thickness.

Figure 3.36 shows the diffraction wavefront sensitivity to chrome thickness variations. As an example, for a grating with 50 nm chrome and 20% duty-cycle, 1 nm thickness variation of chrome would cause 0.0015λ deviations for the zero-order diffracted wavefront.

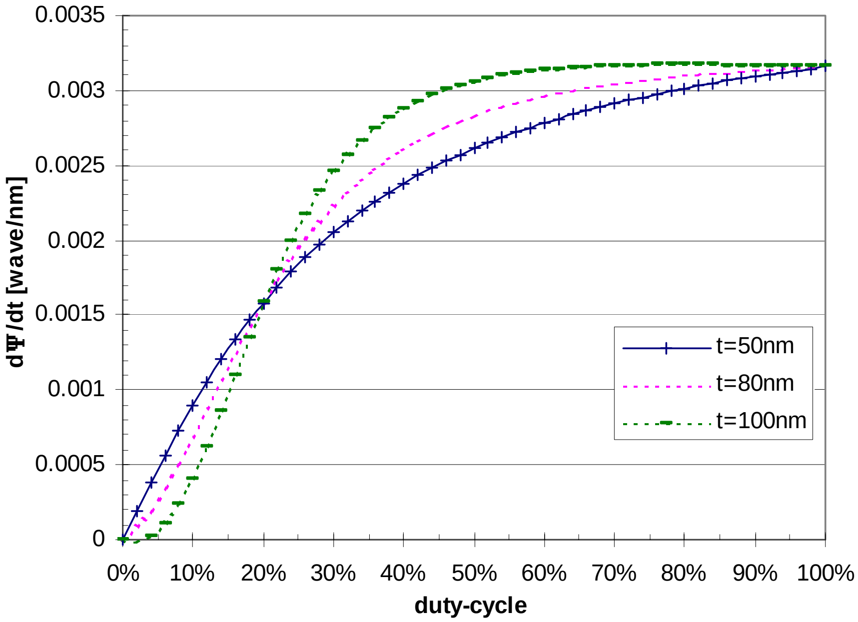

Figure 3.36. Wavefront phase sensitivity function to 1 nm chrome thickness variations for chrome-on-glass gratings in zero-order diffraction beam.

Grating duty-cycle (D) is defined as the grating line width (W) divided by the grating period (T): $D = \frac{W}{T}$; therefore, $\delta D = \frac{1}{T}\delta W$. Wavefront phase sensitivity to the grating line width variation can be calculated using the phase sensitivity function for grating duty-cycle through the following relationship:

$$\frac{\delta\Psi}{\delta W} = \frac{\delta\Psi}{\delta D}\cdot\frac{1}{T} \tag{3.32}$$

Therefore, wavefront phase sensitivity as a function of fractional grating line width variations (δW/W) can be calculated as:

$$\frac{\delta\Psi}{\delta W} = \frac{\delta\Psi}{\delta D} \cdot \frac{1}{T} = \frac{\delta\Psi}{\delta D} \cdot \frac{D}{W}$$

$$\frac{\delta\Psi}{\left(\frac{\delta W}{W}\right)} = \frac{\delta\Psi}{\delta D} \cdot D \qquad (3.33)$$

Figure 3.37 shows the wavefront phase sensitivity to 1% variation in grating line width from the nominal value for zero order diffraction beam. For example, consider a chrome-on-glass grating with 100 nm chrome thickness and 20% duty-cycle, a 10% line width tolerance, which is equivalent to a 2% duty-cycle tolerance, will experience a wavefront phase error of ±0.011λ.

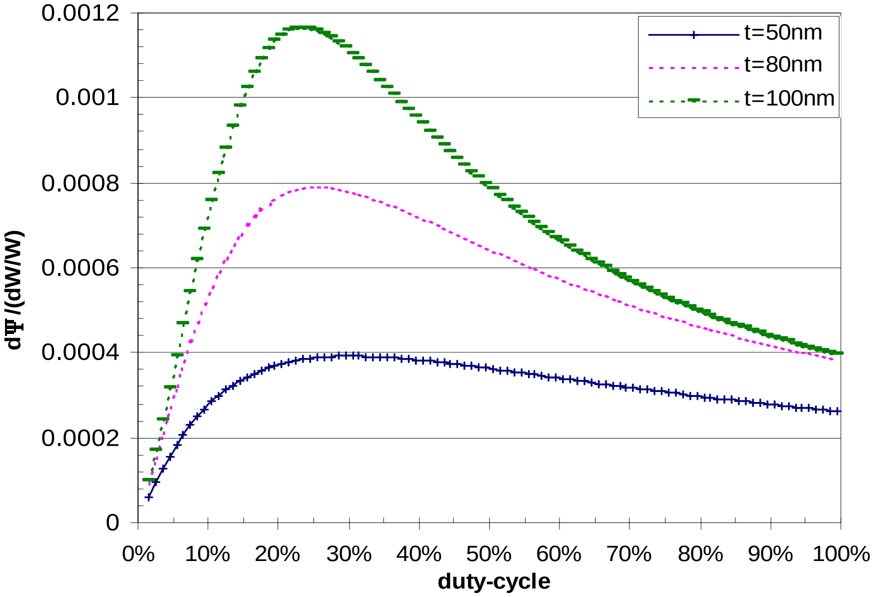

Figure 3.37. Wavefront phase sensitivity function for chrome-on-glass gratings with different chrome thickness per 1% line width variation from the nominal value in the zero-order beam.

Diffracted wavefront phase for all non-zero orders (m≠0) are shown in Figure 3.38 and Figure 3.39. Figure 3.38 gives the relationship between the diffracted wavefront phase functions and the chrome thickness. Like phase grating, diffracted phases vary linearly with the chrome thickness or phase depth for all non-zero order beams. The dependent of diffracted phase on chrome thickness variation is constant.

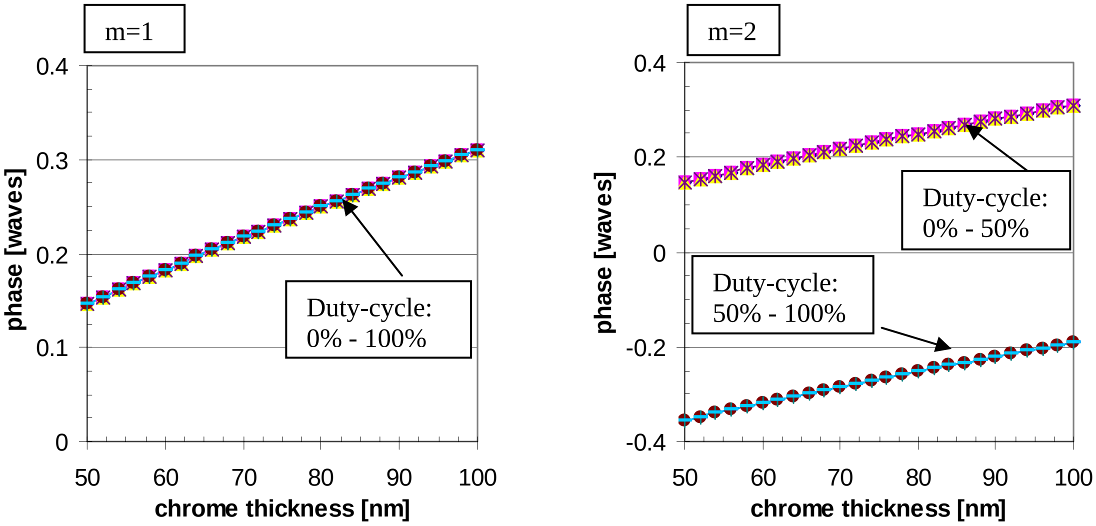

Figure 3.38. Wavefront phase vs. chrome thickness for the 1st-order and 2nd-order diffraction beams for all duty-cycle from chrome-on-glass gratings.

Diffracted wavefront phase versus duty-cycle for non-zero order beams are shown in Figure 3.39. Again similar to phase grating, the phase discontinuities phenomena is observed. The number of phase discontinuity appeared for each order equals to the order number minus one. Grating duty-cycle deviations have no effects on non-zero order wavefronts.

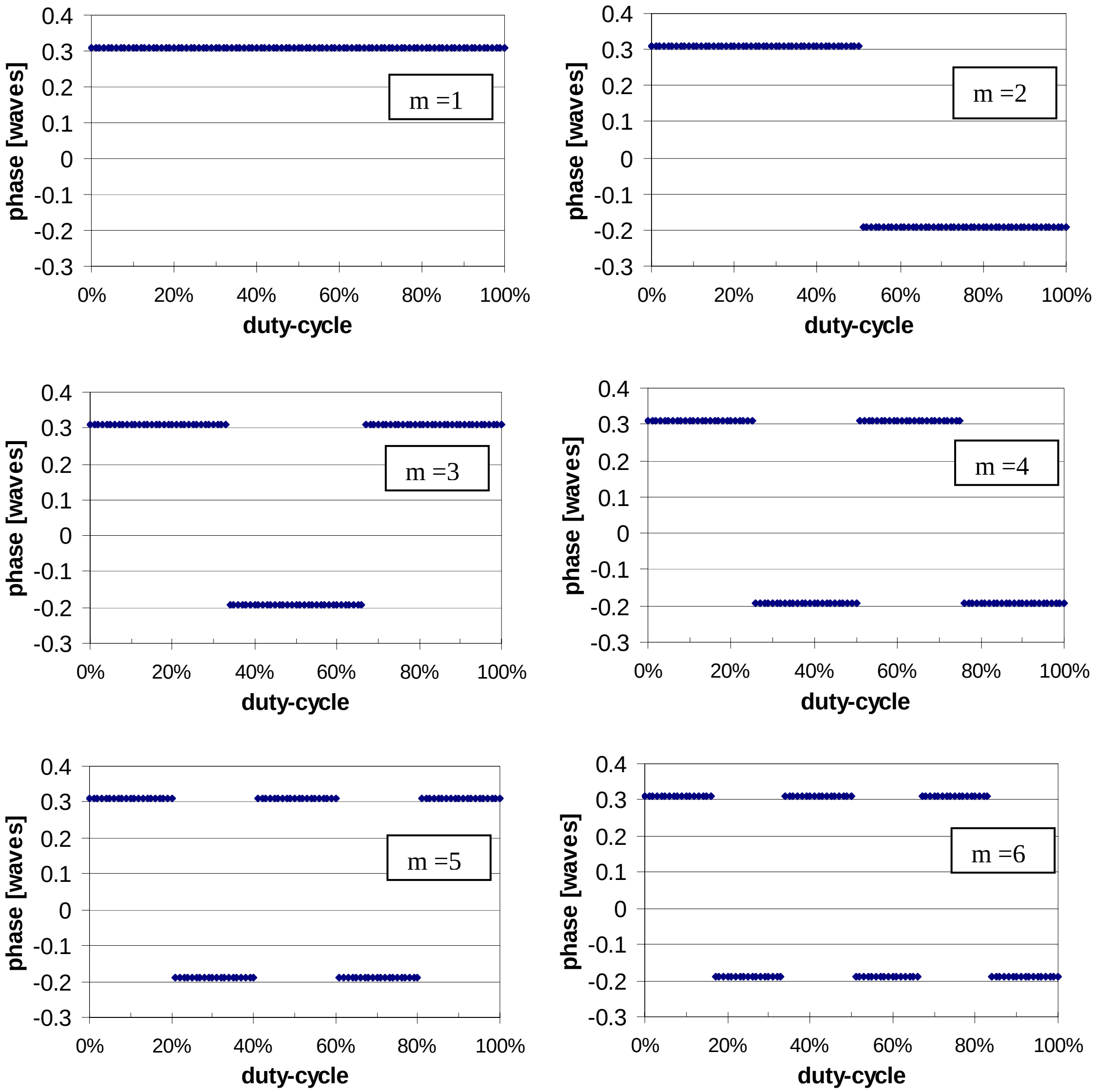

Figure 3.39. Wavefront phase vs. grating duty-cycle for non-zero diffraction orders for chrome-on-glass gratings with 100 nm chrome thickness.

Using scalar diffraction model, grating duty-cycle and phase depth errors and their effects on diffracted wavefront efficiency and phase functions are studied. Wavefront phase sensitivity functions for the binary linear grating model are determined. Using the wavefront sensitivity functions, potential wavefront phase and efficiency errors can be estimated with knowledge of the uncertainties from the CGH fabrication processes. The wavefront sensitivity functions can also be used as guidance for the design of CGHs to reduce or eliminate wavefront errors produced by fabrication uncertainties. In the following chapter, we will present experimental data on wavefront phase measurements for both phase and chrome-on-glass gratings. The results will be used to verify our theoretical model.

CHAPTER 4

DIFFRACTION WAVEFRONT PHASE MEASUREMENTS OF BINARY GRATINGS

In Chapter 3, mathematical model of binary linear gratings is used for analyzing diffraction wavefront phase deviations as results of hologram fabrication tolerance and uncertainties. Both phase and chrome-on-glass gratings are studied. Analytical solutions to the wavefront sensitivity function for both gratings are derived and presented. In this chapter, we describe measurements of sample phase and chrome-on-glass gratings with varied groove depth and duty-cycle values. Descriptions of the structures for both grating designs are given. The samples are measured using phase-shifting interferometers and the measured wavefront phase variations as functions of grating duty-cycles and groove depth are calculated. The experimental results are compared with theoretical models presented in the previous chapter.

4.1. PHASE GRATING

4.1.1. Description of the Sample Phase Grating

Results of the phase sensitivity analysis from Chapter 3 show that wavefront phase functions are most sensitive to grating phase depth variations for zero-order diffraction beam produced by a phase grating with 50% duty-cycle and 0.5 wave phase depth. Wavefront phase functions are most subjective to grating duty-cycle errors for zero-order diffraction beam produced by a phase grating with 0.5 wave phase depth at 50% duty-cycle. In this section, sample phase gratings with duty-cycle ranging from 40% to 60% and phase depth ranging from 0.44 waves to 0.58 waves were manufactured by direct laser beam writing and measured using a phase-shifting interferometer. Diffraction wavefront phase functions produced by the sample gratings are evaluated to determine the wavefront phase sensitivity functions.

Figure 4.1 shows the layout of the sample phase grating design for this experiment. The sample grating is divided into a 5 x 11 array, where each cell in the array contains a linear grating with specific duty-cycle and groove depth. The gratings were designed for a reference wavelength of 0.633 um. Along each row of the grating array, duty-cycle values are varied in a 2% increment from 44% to 60%. A 0% and a 100 % duty-cycle grating are placed at the first and the last cell of each row in the grating array. Along each column of the grating array, groove depth or half phase depth values are designed at 0.22λ, 0.24λ, 0.25λ, 0.27λ and 0.29λ.

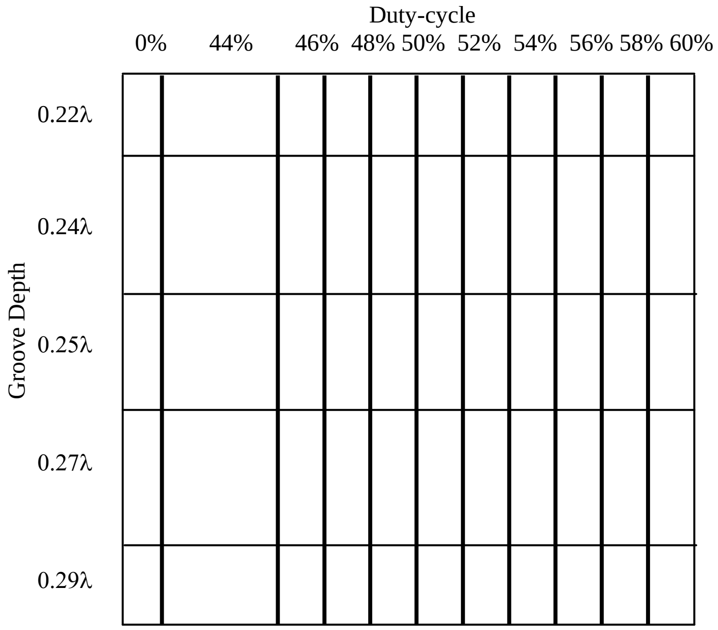

Figure 4.1. Design layout of the sample phase grating.
It is a 5 x 11 array where each cell in the array contains a linear grating.

The sample grating is 30 mm by 30 mm in square. Each column has a width of 2.17 mm. Adjacent columns are separated by a 20 um gap. Column #2 in the finished grating sample, which contains gratings with 44% duty-cycle, was made three times wider than the design value due to manufacturing errors. Linear gratings in all cells have 50 um grating period with the groove directions parallel to the row direction of the grating array. Figure 4.2 shows an enlarged view of a small area on the sample grating array. Figure 4.3 shows a profile plot of a cross-section of the sample grating.

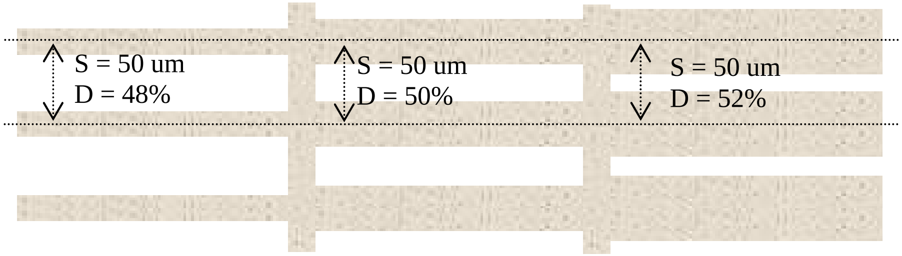

Figure 4.2. An enlarged top view of a small area on the sample grating array. Duty-cycle varies along the row direction of the grating.

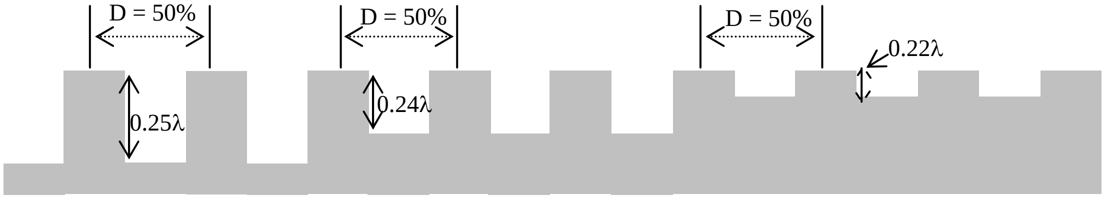

Figure 4.3. Cross-section view of column #3 (50% duty-cycle) of the sample grating array. Groove depth varies along the column direction.

The sample grating array is engraved on a 60 mm x 60 mm square glass plate (see Figure 4.4). It is designed to be used in the reflection mode and the grating surface is coated with a uniform layer of chrome (Cr) to improve surface reflectance.

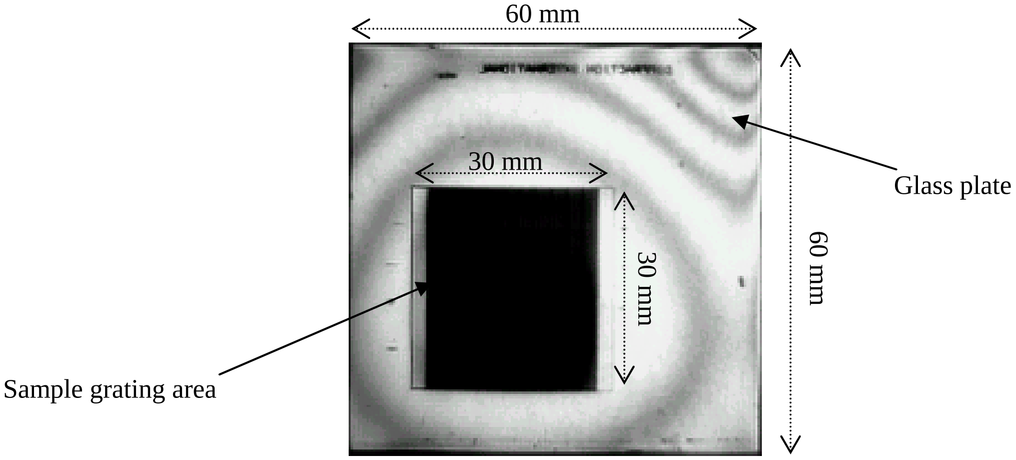

Figure 4.4. Sample grating array engraved on a glass substrate.

4.1.2. Procedure

A phase-shifting Fizeau interferometer was used to measure diffraction wavefronts produced by the sample gratings. The set-up of the experiment is shown in Figure 4.5. The sample grating was treated as a flat test plate and a transmission flat with λ/20 accuracy (λ = 632.8 nm) was used as the reference. The distance between the test grating and reference flat was reduced to minimum during the experiments in order to reduce air turbulence in the test beam path.

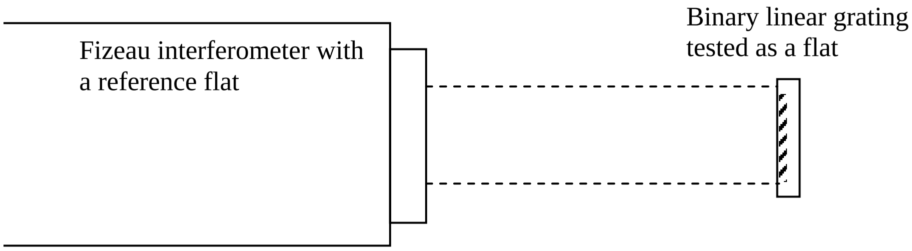

(a) For zero-order wavefront measurement

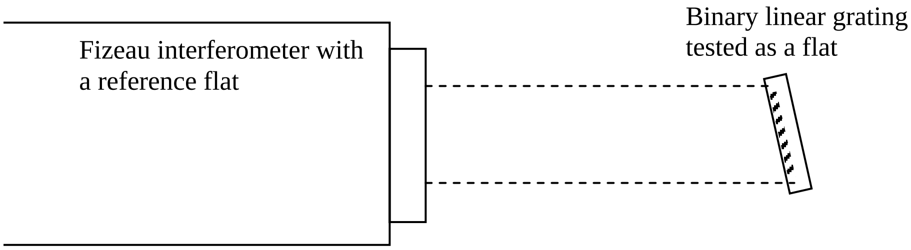

(b) For non-zero order wavefront measurement

Figure 4.5. Experimental setup for sample gratings wavefronts measurements.

Multiple diffraction orders were produced by the linear grating sample. In this study, only the zero-order diffraction wavefront and the first-order diffraction wavefront were measured.

I. Zero-Order Diffraction Wavefront Measurement

In order to measure the zero-order diffraction beams, the sample grating was aligned parallel to the reference flat, as shown in Figure 4.5(a). An interferogram obtained during the measurements is shown in Figure 4.6. A large amount of substrate figure errors and residual aberrations from the interferometer was observed in the measured wavefront. In order to reduce the effects of the substrate errors and the residual aberrations, low order Seidel aberrations were removed from the measured raw wavefront phase functions. A measured wavefront phase map with tilt, power and astigmatism removed is shown in Figure 4.7.

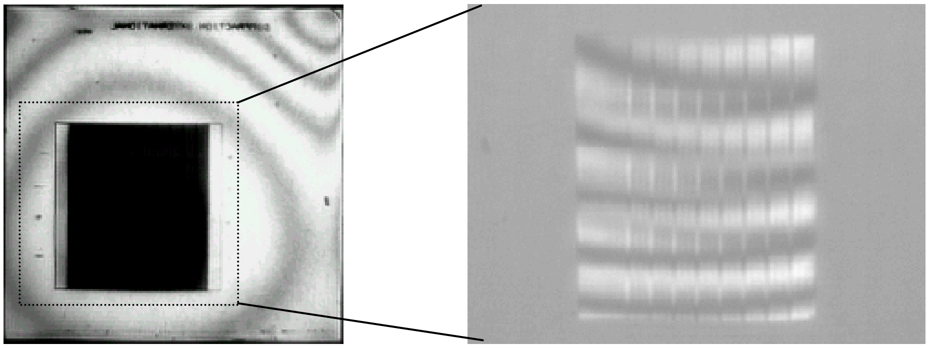

Figure 4.6. Interferograms obtained for the sample phase grating shown in the zero-order. (Note the phase shift around the center of the pattern).

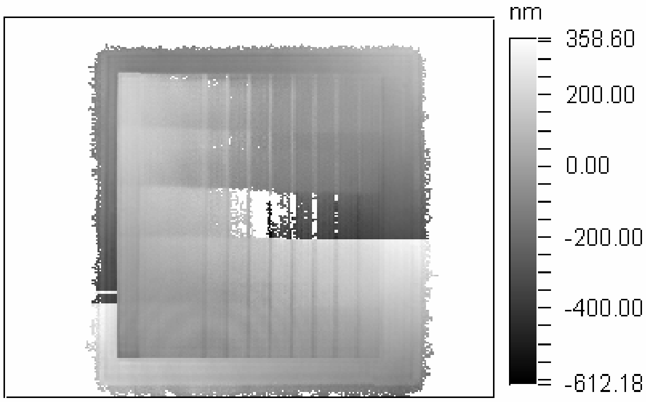

Figure 4.7. Measured zero-order wavefront phase of the sample phase grating with tilt, power and astigmatism removed.

Removal of tilt from the measured phase function eliminates the linear variation in the measured wavefront due to mechanical misalignments of the sample grating respect to the reference flat. It undermines, at the same time, the linear wavefront phase variation produced due to the grating duty-cycle change (see Figure 4.8). In order to compensate the over-corrected wavefront tilt, areas outside the grating array on the sample is utilized. The sample grating was measured with a clear aperture that is larger than the actual area of the grating array. Ideally, the same phase value should be obtained from areas outside the sample grating array where the surface is coated with a uniform layer of chrome, when substrate figure errors are ignored and tilt in the test surface is removed. Using the phase values from the surrounding areas of the grating array, wavefront tilt can be compensated to achieve zero phase difference between both sides of the grating array.

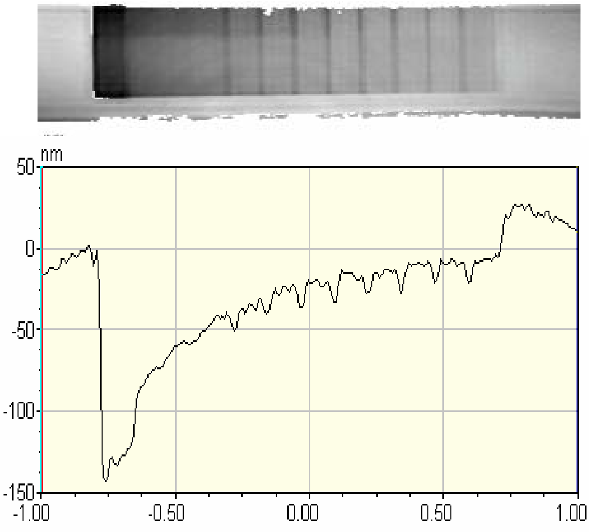

Figure 4.8. Phase profile plots of the sample grating array with surrounding Cr coated glass substrate.

II. First-Order Diffraction Wavefront Measurement

In order to measure first diffraction order wavefront, the sample grating must be tilted respective to the reference flat so that the 1st diffraction beam was seen by the interferometer (see Figure 4.5(b)).

4.1.3. Results and Analysis

I. Wavefront Phase Sensitivity for the Zero Diffraction Order

Optical interferometric measurements provide information on the wavefront phase function of the test beam relative to the reference wavefront. In order to avoid unnecessary complications or confusions when comparing the experimental results with the theoretical data, phase deviations between adjacent grating cells were used in our analysis instead of the absolute phase values. The presented phase deviations functions in the following section represent wavefront phase changes as results of the grating duty-cycle or the groove depth variations on the sample grating array.

Linear gratings with the same duty-cycle on the sample grating array were measured together to determine wavefront phase sensitivities as a function of grating phase depth variations. In order to reduce random noises in the measured wavefront phase values, four sets of measurement were conducted for each analysis. The standard deviation of the four sets of data were calculated. Measured wavefront phase deviations per unit grating groove depth variation for grating with various duty-cycles are shown in Figure 4.9. Theoretical wavefront phase sensitivity values derived from Chapter 3 are overlaid on the experimental results in the same charts. The error bars of the experimental data provides information on the noise and confidence level of our results. A large standard deviation of the data implies a high noise level or a large amount of random errors in our measurement procedures. For the phase sensitivity versus grating phase depth analysis, good agreement among the experimental results and the theoretical data are observed in most cases. At 50% duty-cycle, zero diffraction efficiency is obtained at 0.25 waves groove depth. As a result of this, no interference fringes were seen for the 0.27 waves and 0.24 waves gratings, and phase values for the two gratings are missing in the chart.

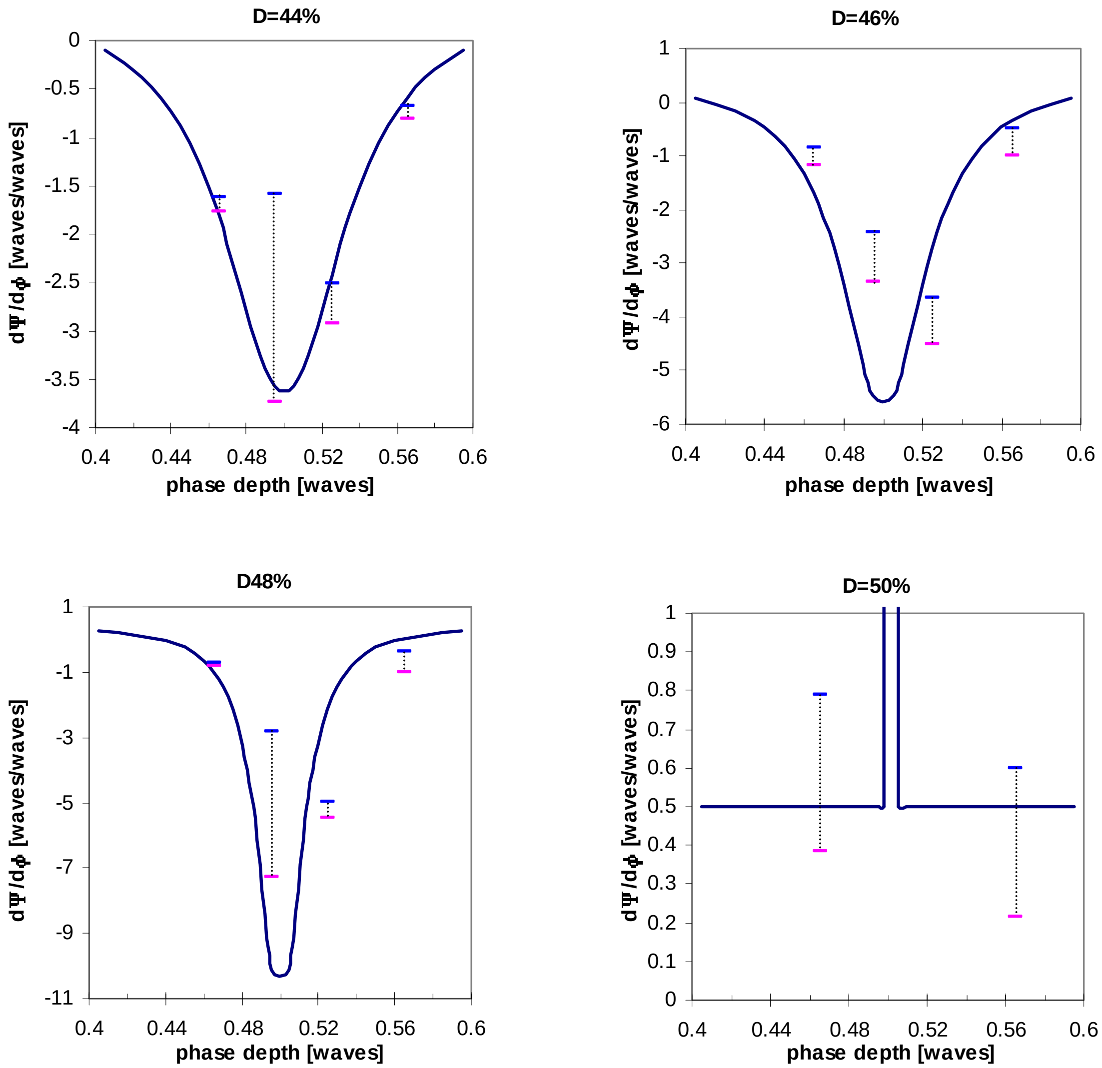

Figure 4.9. Diffraction wavefront phase deviations per grating etching depth variation for the zero-order beam of the sample phase grating.
Experimental data (vertical bar) vs. Theoretical results (solid line).

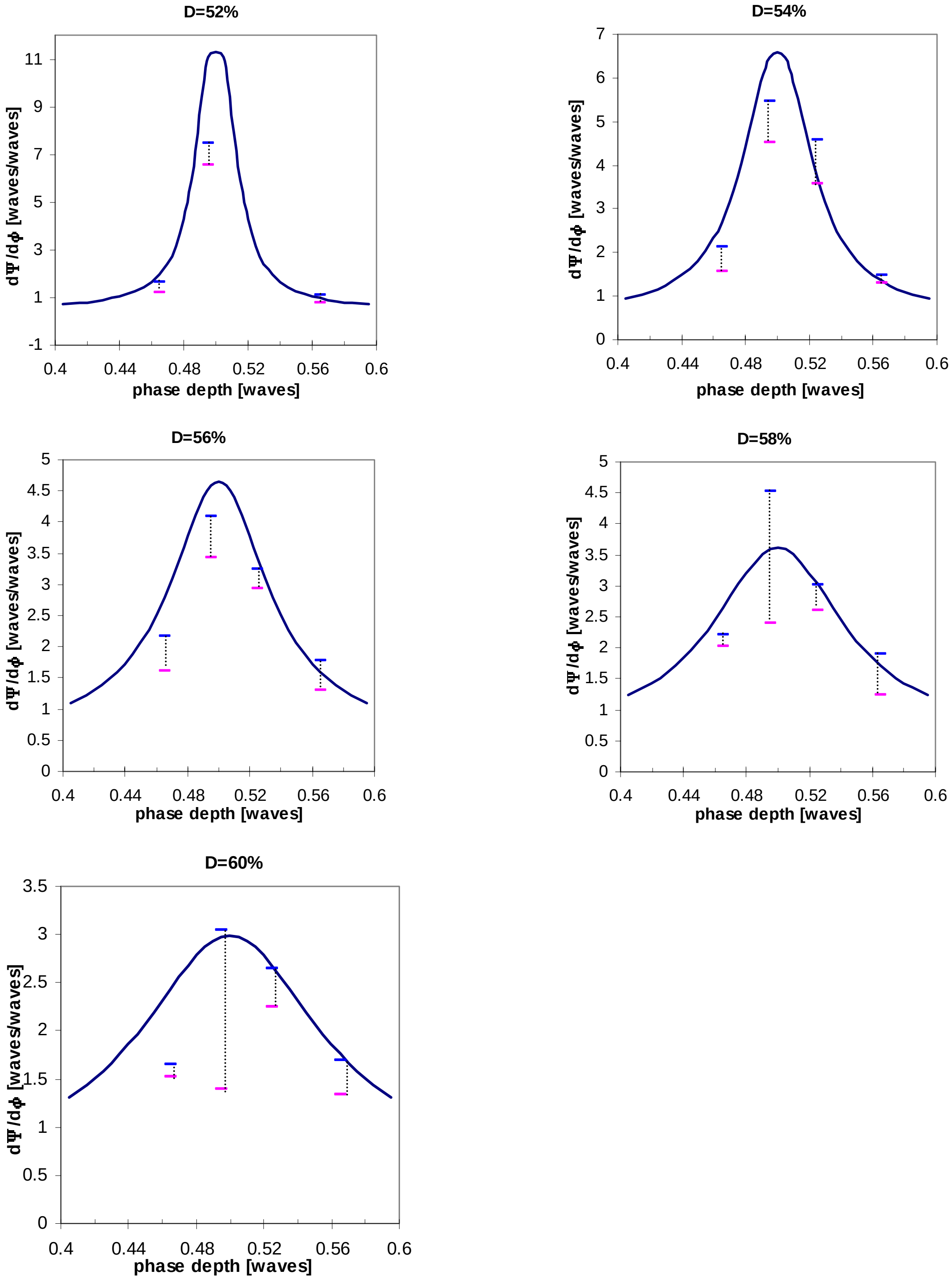

Figure 4.9. (continued) Diffraction wavefront phase deviations per grating etching depth variation for the zero-order beam of the sample phase grating. Experimental data (vertical bar) vs. Theoretical results (solid line).

Gratings with the same phase depth were measured together in order to determine wavefront phase sensitivities as a function of grating duty-cycle variations. Four sets of data were again taken for each measurement. The results of wavefront phase deviations per duty-cycle variations for gratings with various grating phase depths are given in Figure 4.10. Large deviations of measured data are seen. Although the measured data did not agree perfectly with the theoretical predication, general behaviors of the wavefront phase deviation as a function of grating groove depth variations hypothesized by our analytical models are observed.

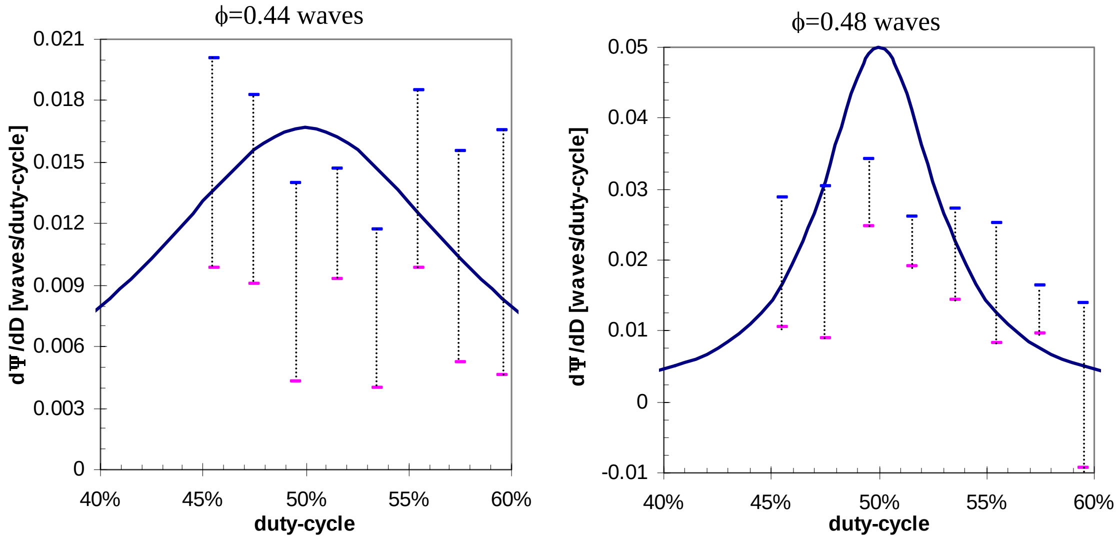

Figure 4.10. Diffraction wavefront phase deviations per grating duty-cycle variation for the zero-order beam of the sample phase grating.
Experimental data (vertical bar) vs. Theoretical results (solid line).

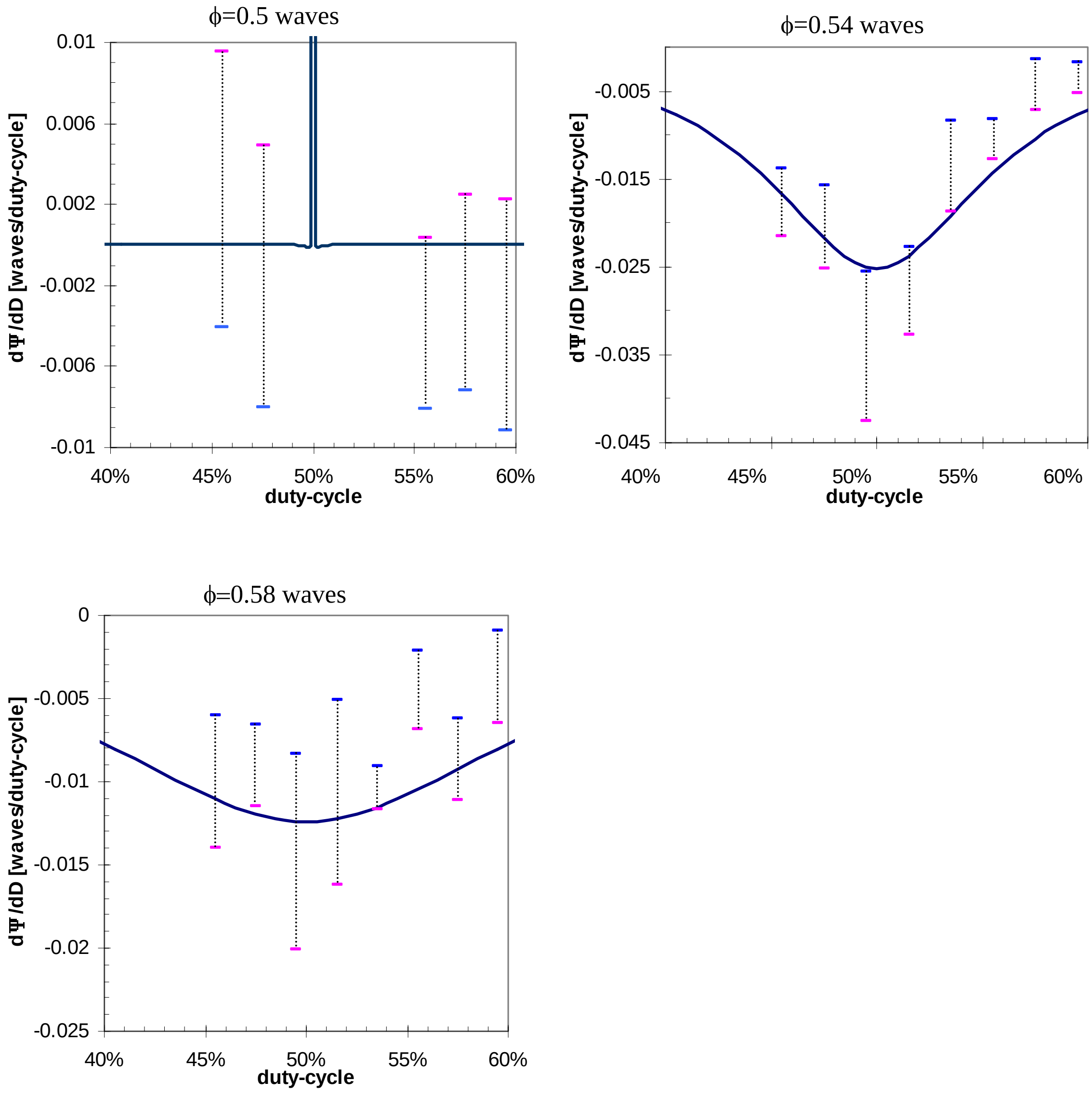

Figure 4.10. (continued) Diffraction wavefront phase deviations per 1% duty-cycle variation for the zero-order beam of the sample phase grating. Experimental data (vertical bar) vs. Theoretical results (solid line).

II. Wavefront Phase Sensitivity for the First Diffraction Order

The same wavefront phase analysis that was conducted for the zero-order diffraction wavefront was performed for the first order diffraction beam. The measured

1^{st}-order diffracted phase to phase depth and duty-cycle variations are shown in Figure 4.11 and Figure 4.12.

Our analytical model predicts constant sensitivity phase depth variations to all non-zero order diffraction beams. This agrees with the data, shown in Figure 4.11.

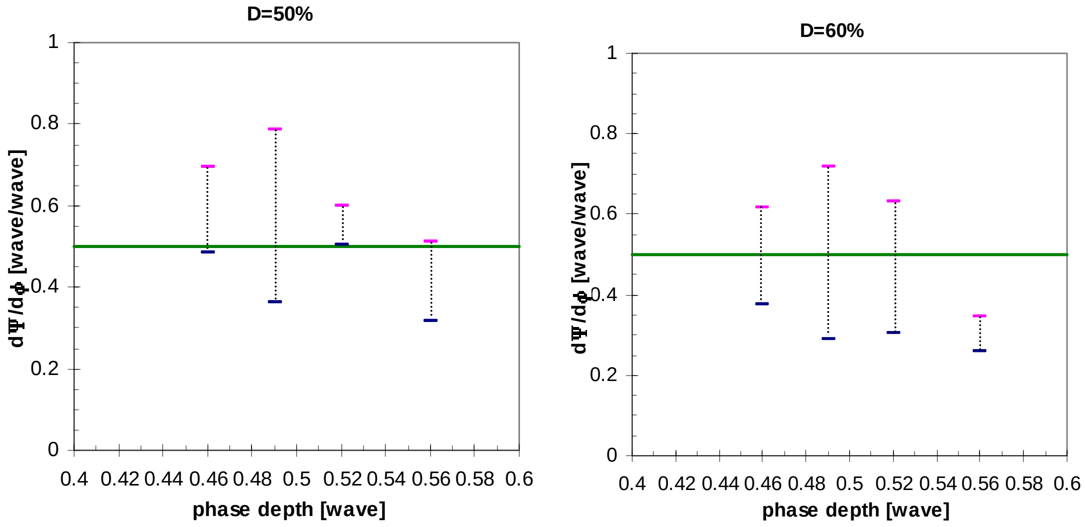

Figure 4.11. Wavefront phase sensitivity functions per phase depth variations for the 1^{st} order diffraction wavefront of the sample phase grating. Experimental data (vertical bars) vs. Theoretical data (solid line).

The measured wavefront sensitivities to grating duty-cycle variations are shown in Figure 4.12. According to our analytical model, the diffracted wavefront phase values are not sensitive to grating duty-cycle variations. The measured data agrees well with this theoretical predication.

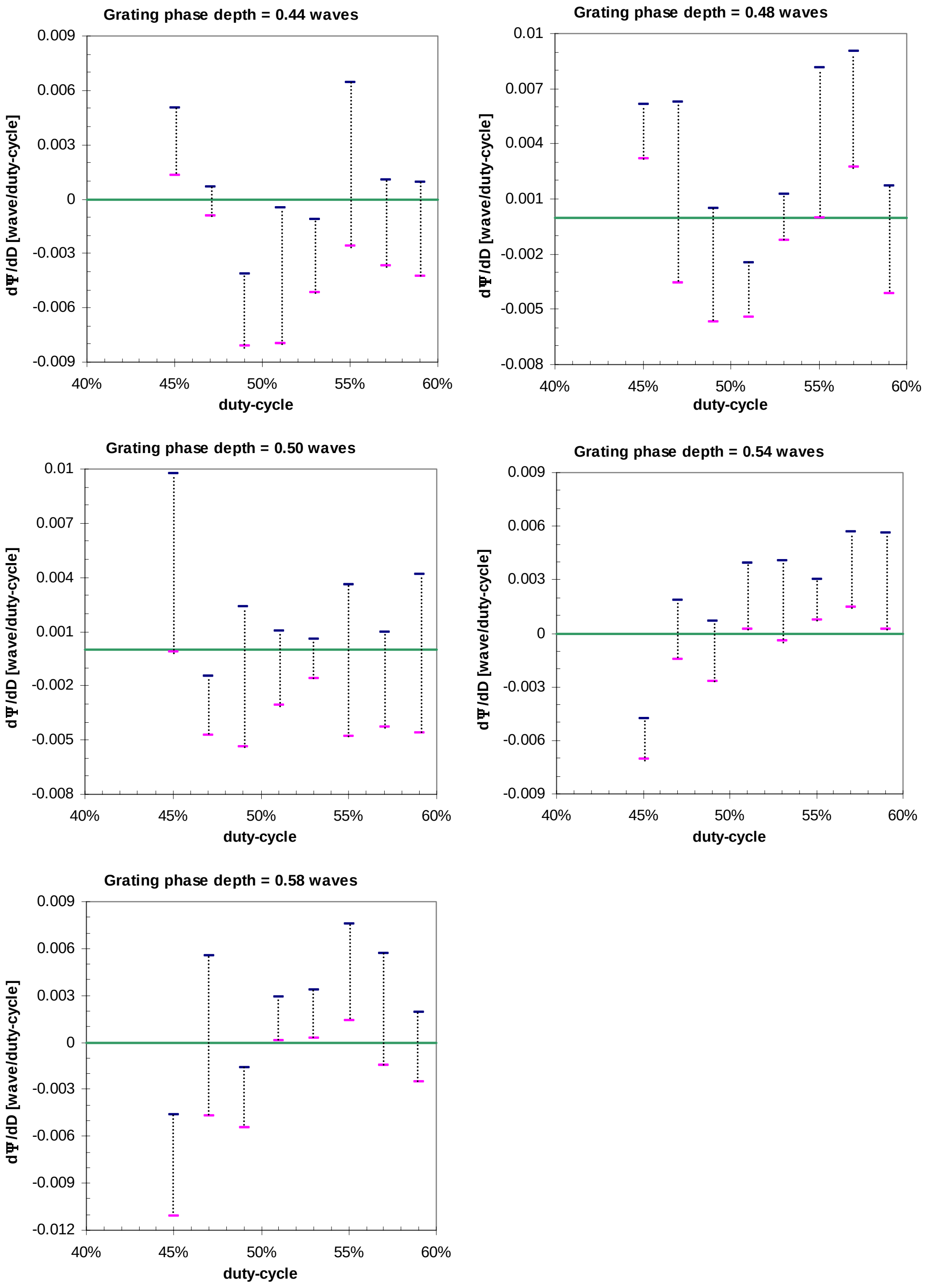

Figure 4.12. Wavefront phase sensitivity functions per 1% duty-cycle variations for the 1st order diffraction wavefront of the sample phase grating. Experimental data (vertical bars) vs. Theoretical data (solid line).

4.2. CHROME-ON-GLASS GRATINGS

4.2.1. Description of the Sample Chrome-on-Glass Grating

A sample chrome-on-glass grating was also fabricated by direct laser beam writing. Figure 4.12 illustrates the layout of the sample chrome-on-glass grating design. The sample was divided into eleven columns, where each column contains a linear grating with specific duty-cycle value. The eleven linear gratings have duty-cycle values varying from 0% to 100% in a 10% increment.

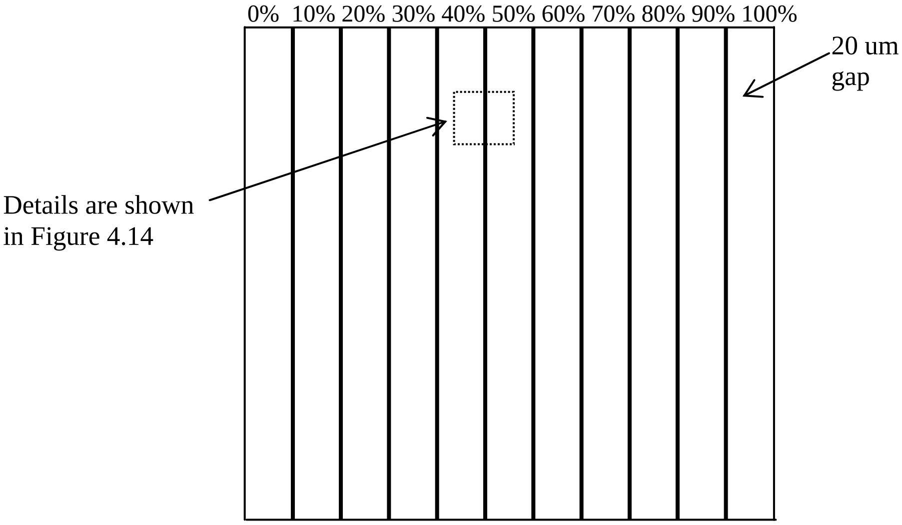

Figure 4.13. Design layout of the sample chrome-on-glass grating.

The sample grating is engraved on a 60 mm by 60 mm square glass plate, where the grating array occupies a 30 mm by 30 mm area in the center of the plate. Each column or linear grating has a width of 2.71 mm. Adjacent columns are separated by a 20 um gap. All linear gratings on the sample have the same grating period (50 um) with the groove direction parallel to the horizontal direction of the sample grating. Figure 4.14 shows a magnified view of a small section on the sample grating captured by an optical microscope. It shows that grating duty-cycle varies from 40% to 50% between adjacent grating columns.

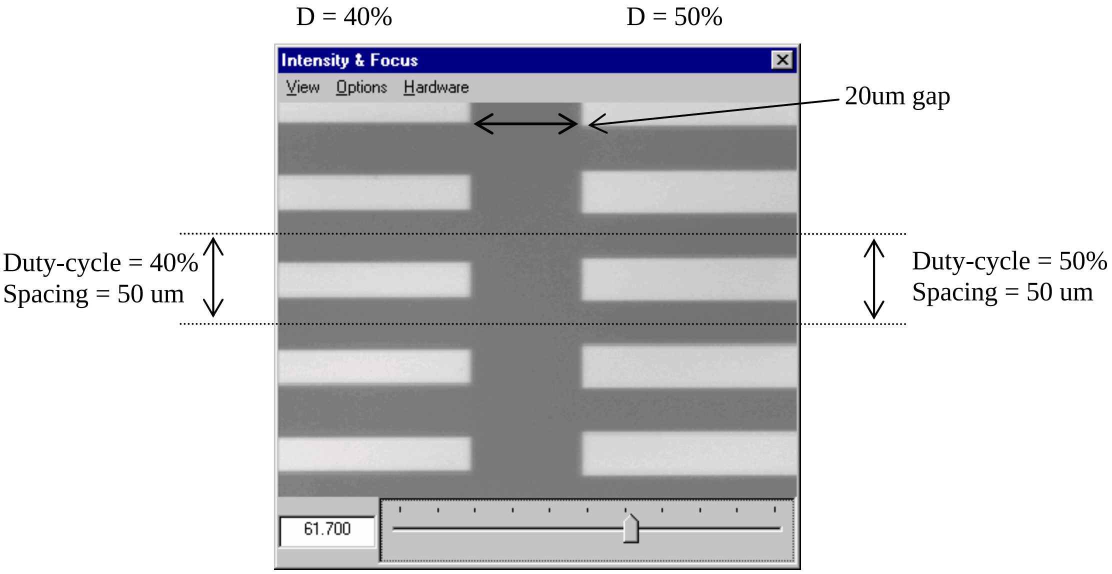

Figure 4.14. Microscope image of a small area on the sample chrome-on-glass grating with 50 um grating period and duty-cycle varied from 40% to 50%.

It is technically difficult to control the exact thickness of the chrome layer. Because of this manufacturing difficulty and our limited resources, film thickness of the sample grating were not varied. Wavefront sensitivities of the chrome-on-glass grating with grating phase depth variations was not included in this studied. Chrome thickness of the sample grating was designed to be 100 nm in order to eliminate multiple reflections in the chrome layer (see Section 3.6).

4.2.2. Procedure

The same experimental set-up used for the phase grating measurements was used for testing the chrome-on-glass grating. The chrome-on-grating was aligned parallel to the reference flat for zero-order diffraction beam measurements. A blue coating was applied to the second surface of the grating to reduce back reflection from the surface. Wavefront phase sensitivities to grating duty-cycle variations for both the zero-order and the first-order diffraction beams were studied.

In addition, diffraction efficiencies for zero through 7th order diffraction beams were analyzed and compared with the theoretical results from Chapter 3. The sample was tilted respect to the reference during the diffraction efficiency analysis on higher order diffraction beams.

4.2.3. Results and Analysis

I. Wavefront Phase Sensitivity for the Zero Diffraction Order

An interferogram obtained from the chrome-on-glass grating is shown in Figure 4.15.

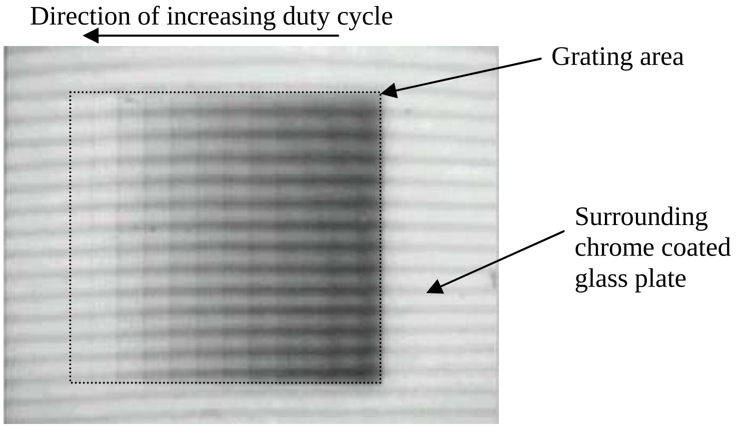

Figure 4.15. Interferogram obtained from the sample chrome-on-glass grating.

Our theoretical model predicted, in Section 3.6.2, a phase difference of 0.27 waves may be observed between a 100 nm chrome layer and a bare glass substrate at 632.8 nm wavelength. However, our experimental results show that measured phase difference between the bare glass (0% duty-cycle grating) substrate and the chrome coating on the sample grating was only 0.05±0.01 waves.

This significant discrepancy between the theoretical and the measured phase depth implies uncertainties in either the chrome coating thickness and/or the index of refraction of the chrome coating. The nominal thickness of the chrome coating, according to the vendor’s specification, is 1030 ± 50 angstroms. Using an atomic-force-microscope (AFM), the chrome coating thickness of the sample grating was measured. The grating chrome coating was sampled at multiple points; and the average of the measurements indicates a chrome thickness of approximately 50 nm **[Perterson 1999]**.

The index of refraction of the chrome coating of the sample grating was also measured using an ellipsometer. The measured index of refraction of the chrome coating is n = 2.534 and k = 3.61 at wavelength = 632.8, as shown in Figure 4.16 **[J. A. Woolam Co., INC]**. This value again differs from the nominal value of n = 3.6 and k = 4.4 suggested by the specification.

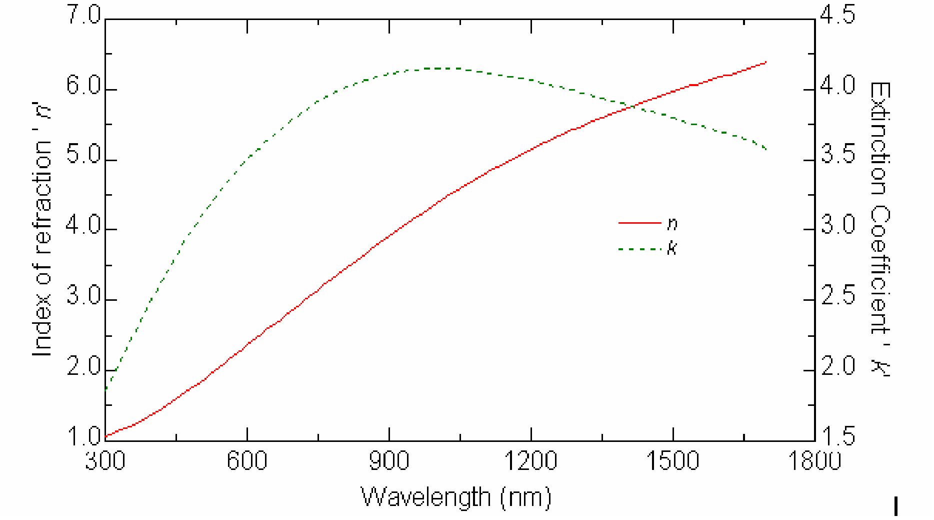

Figure 4.16. Measured index of refraction curves for chromium using ellipsometer. By J.A. Woolam Co., INC.

Using both the measured chrome thickness and the index of refraction, phase depth for the chrome-on-glass grating was calculated to be 0.1 waves. This result is different from both the theoretical and the measured result obtained from the Fizeau interferometer. One more measurement of the grating phase depth was conducted using a microscope interferometer. The measured phase depths were averaged at 0.12 waves from multiple sample points on the sample grating. This result agrees with the calculation using the measured chrome thickness and the index of refraction. The AFM measured chrome thickness and the ellipsometer determined index values are believed to be reliable. (The discrepancy between the results from the Fizeau interferometer and the calculated phase value is not understood; and this issue is subjected for further investigation.)

The wavefront phase sensitivity to duty-cycle variations for the zero diffraction order was measured for the chrome-on-glass grating (see Figure 4.17). The experimental data (shown in vertical bars) are compared with the theoretical model (shown in solid line) assuming the measured parameters of 50 nm chrome thickness and complex index of refraction 2.56-i3.6.

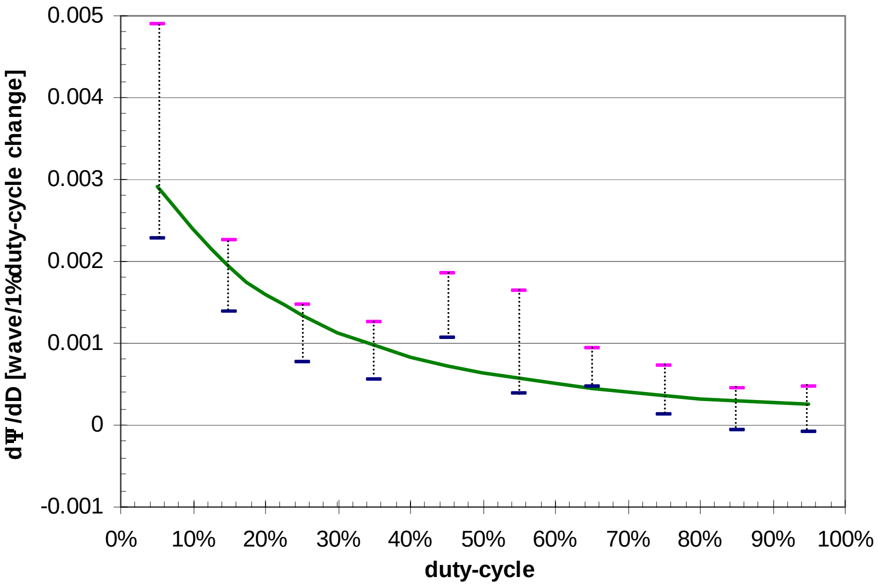

Figure 4.17. Wavefront phase sensitivity functions per 1% duty-cycle variations for the zero order diffraction wavefront for the sample chrome-on-glass grating. Experimental data (vertical bars) vs. Calculated data (solid line).

As shown in the figure above, the majority of measured data shows a good agreement with the theoretical model. Based on all the evidence, it is clear that vendor's specification of the chrome thickness (100 nm) and index of refraction from "*Handbook Of Optical Constants Of Solids II* **"** for bulk chrome does not apply.

II. Wavefront Phase Sensitivity for the First Diffraction Order

Based on the theoretical models, wavefront phase values are not sensitive to grating duty-cycle variations for all non-zero diffraction orders. Wavefront phase sensitivity function for the first diffraction order beam of the sample grating was calculated and compared with the theoretical data.

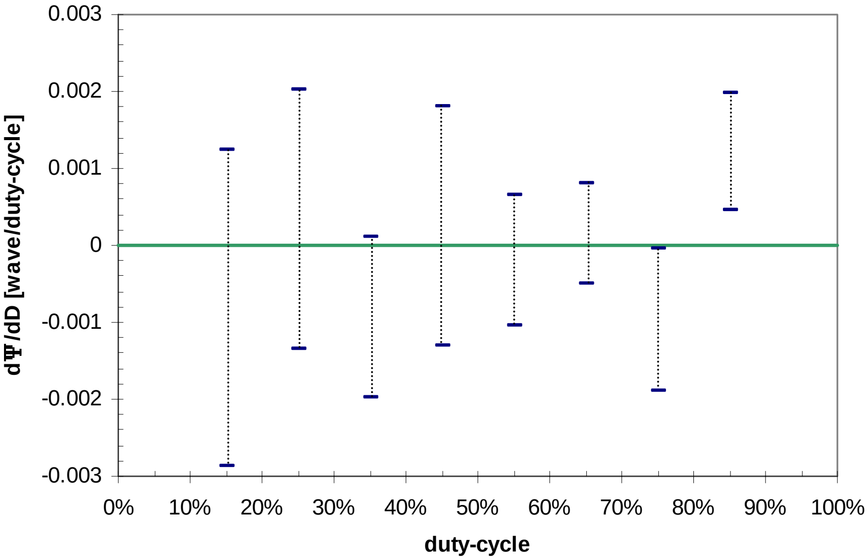

Figure 4.18. Wavefront phase sensitivity functions per 1% duty-cycle variations for the 1^{st} order diffraction wavefront for the sample chrome-on-glass grating. Experimental data (vertical bars) vs. Theoretical data (solid line).

Figure 4.18 shows the standard deviation of the experimental data. Good match between the experimental result and the theoretical predications are observed. Small fluctuations in the data are results of random errors in the measurement.

III. Diffraction Efficiency Distributions

In Chapter 3, we have derived the relationships between diffraction efficiency and grating duty-cycle at different diffraction orders. Our mathematical model shows that diffraction efficiency functions increases non-monotonically with duty-cycle (see Figure 3.29) for the zero-order beam. Diffraction efficiency for non-zero beams varies periodically with changes in grating duty-cycle (see Figure 3.31). The number of times that maximum efficiency values can be obtained for each diffraction order equals to the order number. This conclusion is verified with our experiments.

Diffraction efficiency functions for all desired diffraction orders of the sample grating are analyzed with helps from interferograms. Figures 4.19 shows the observed interferograms for zero through 7th order diffraction beams. Parallel fringes seen across the vertical direction (y-direction) of all interferograms indicate tilt of the sample grating in the vertical direction. Tilt of the sample grating in the horizontal direction was eliminated and no tilt fringes in the x-direction is seen. Observed intensity levels along x-direction across the interferograms in this analysis correspond directly to the diffraction efficiency values for gratings with various duty-cycles at specific diffraction order.

A normalized intensity distribution plot calculated based on the theoretical diffraction efficiency values is attached to each interferogram. For non-zero order beams, the phase reversal effects between different grating duty-cycles are also included in the intensity plots. Discontinuities of the fringes in the intergerograms correspond to the discontinuities of the phase function, or phase reversal.

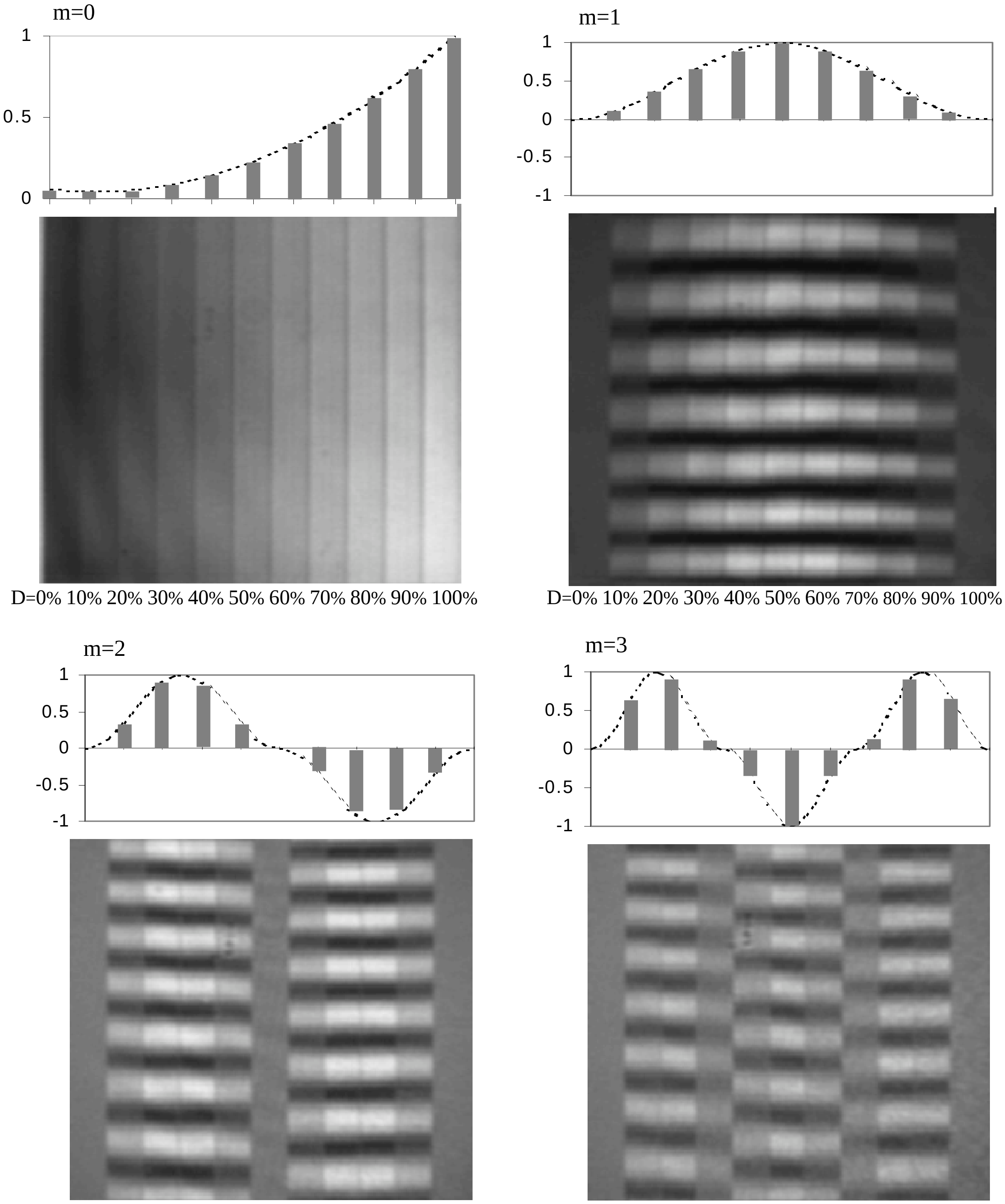

Figure 4.19. Interferogram indicating diffraction efficiency distribution and wavefront phase as a function of grating duty-cycle at different diffraction orders. Top chart shows the corresponding theoretical values.

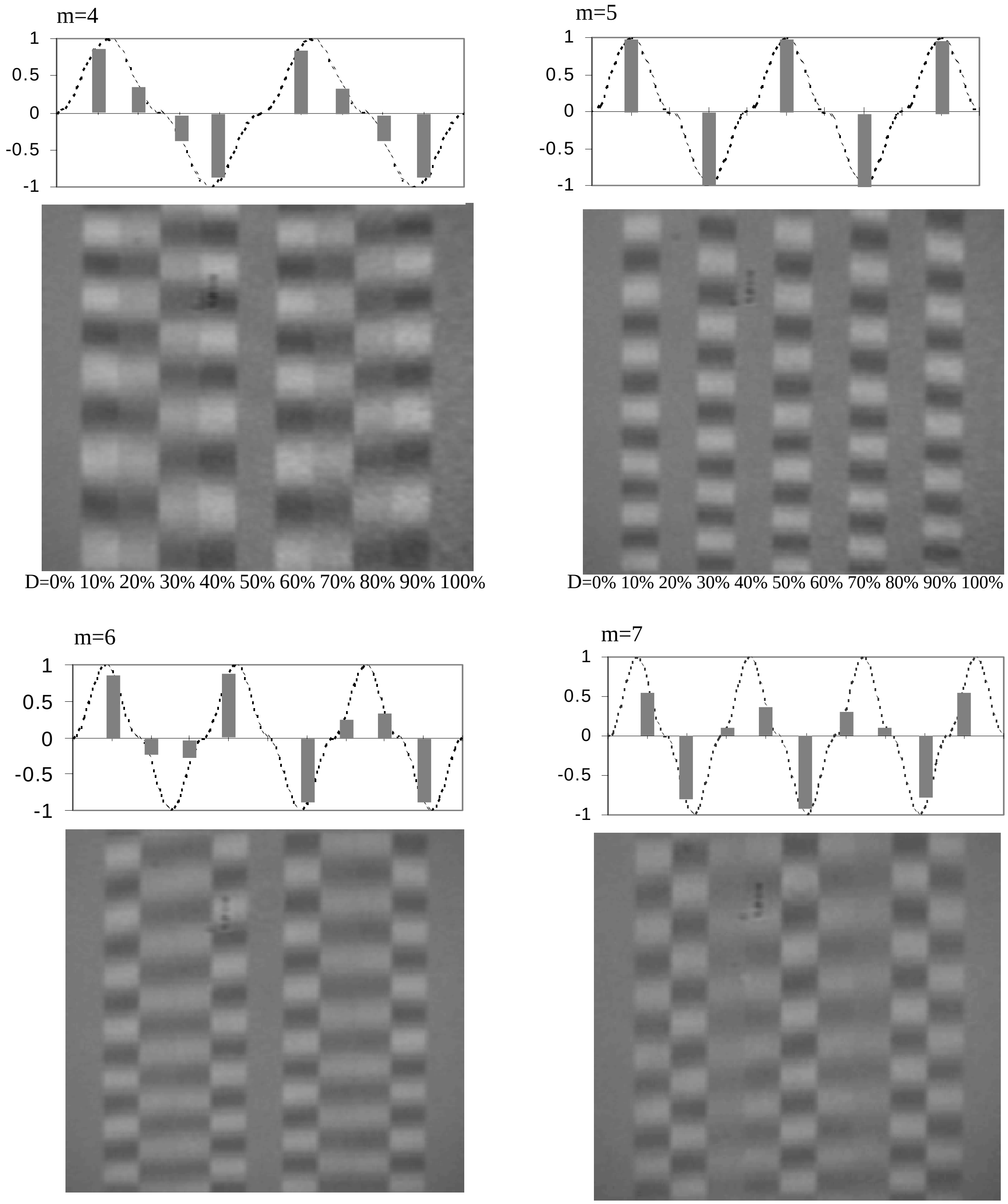

Figure 4.19. (Continued) Interferogram indicating diffraction efficiency distribution and wavefront phase as a function of grating duty-cycle at different diffraction orders. Top chart shows the corresponding theoretical values.

As seen from the figures, observed intensity distribution functions at different diffraction orders with variations in grating duty-cycle agree perfectly with the theoretical predictions. Periodicity of the diffraction efficiency functions for non-zero order beam produced by the chrome-on-glass grating can be clearly identified. Phase reversals, or the $\lambda/2$ phase discontinuities, in the diffraction efficiency for non-zero order beams predicted in Section 3.6.2 are also observed in the interferograms.

CHAPTER 5

EXAMPLES OF CGH ERROR ANALYSIS FOR OPTICAL TESTS

The objective of this chapter is to demonstrate one of the many applications using the results of CGH fabrication error analysis in practical problems. Two examples of utilizing CGHs in optical interferometry for aspheric surfaces measurements are given. Typical CGH fabrication errors such as substrate figure errors, pattern distortions, duty-cycle and phase depth variations are considered in the analysis. Wavefront errors produced by the two CGHs due to fabrication tolerances and uncertainties are estimated from the root-sum-squared (RSS) of all error sources. The calculated wavefront errors are used to determine errors for the interferometric measurements.

5.1. PHASE CGH

In the first example, a phase CGH is used with a Fizeau interferometer for testing aspheric optical components. The measurement set-up is shown in Figure 5.1.

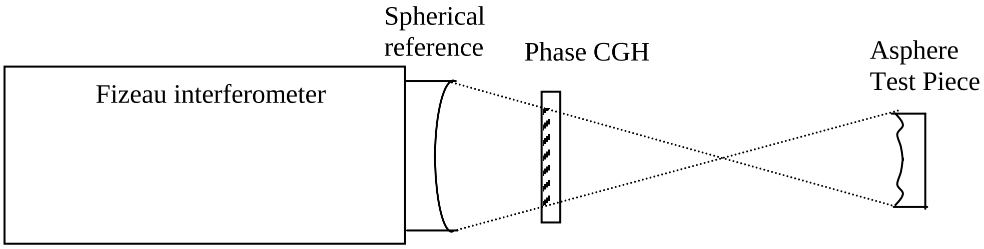

Figure 5.1. Asphere metrology uses a Fizeau interferometer with a phase CGH.

The phase CGH is designed to be used in the 1^{st} order transmission mode. It can be fabricated using a direct laser/electron beam writing process. The hologram has a glass substrate with an index of refraction of n=1.5. It has a grating groove depth of π radians and a 50% duty-cycle. In this example, we assume a potential pattern distortion of 1um in the hologram. The averaged fringe spacing on the CGH is approximated 40 um. Because the hologram is used in the transmission mode, surface figure errors from both the front and the back surface of the CGH contribute to diffraction wavefront aberrations; errors on both surfaces must be included in the error analysis. The phase CGH has a RMS substrate figure error of $\lambda/10$ on both the front and the back surface. It may be noticed from Figure 5.1 that the test beam passes through the CGH twice in this setup. Consequently, the total wavefront phase error for the setup is twice the value of the calculated error per pass.

Table 5.1. Phase CGH structure parameters.

Parameters	Values
Grating Type	Binary Phase Grating
Material	Glass: n = 1.5
Operating Mode	Transmission
Diffraction Order	1st order
Averaging Grating Period	40 um
Substrate Figure Errors	$\lambda/10$ rms
Pattern Distortion	1 um
Grating Groove Depth	$0.5\lambda \pm 5\%$
Grating Duty-cycle	50% ± 2%

Wavefront phase deviations caused by CGH fabrication errors can be determined using the wavefront phase errors analysis results shown in Chapter 3. For example, pattern distortion is calculated using Equation (3.26); wavefront phase errors contributed from grating groove depth errors and duty-cycle errors are determined using the wavefront phase sensitivity functions Equation (3.28) and Equation (3.30). The calculated wavefront phase errors per pass for each error source are listed below:

Table 5.2. Diffraction wavefront phase errors from CGH fabrication uncertainties.

Source of Errors	Fabrication Tolerances	Wavefront Phase Errors per Pass
RMS Substrate Figure Error (Front Surface)	$\lambda/10$	$\lambda/20$
RMS Substrate Figure Error (Back Surface)	$\lambda/10$	$\lambda/20$
Pattern Distortion	±1 um	$\pm\lambda/40$
Grating Groove Depth Error	±5%	$\pm\lambda/80$
Duty-cycle Error	±2%	0
Root-Sum-Squared Errors :		$\pm 0.076\lambda$

Assuming the calculated CGH errors are un-correlated and independent from each other, the total wavefront phase errors for the phase hologram can then be estimated as the root-sum-square (RSS) of these errors. The calculation shows that the estimated diffraction wavefront phase errors produced by fabrication uncertainties and tolerance in the phase CGH is approximately 0.152λ including the effect of the double path of the test beam. In other words, the accuracy of the asphere measurement using the setup in Figure 5.1 and the example CGH is limited by ±0.152λ even when other sources of errors, such as interferometer errors and air turbulence, are eliminated.

As shown in Table 5.2, the largest individual error source is the substrate figure errors of the CGH. Normally the substrate error may be identified and eliminated. CGH substrate errors can be measured using the zero-order diffraction beam. In this example, however, the phase grating is constructed by a 50% duty-cycle and λ/2 phase depth. Recall section 3.4.2, diffracted wavefront phase shows extremely high sensitivities to duty-cycle variations for grating with a 50% duty-cycle and λ/2 phase depth. In other words, a 1% duty-cycle fabrication error on the grating could produce up to λ/2 wavefront phase deviations. This phase error overwhelms the effects of CGH substrate error in the zero diffraction order and prohibits the substrate figure measurement in this example.

5.2. CHROME-ON-GLASS CGH

In the second example, a chrome-on-glass CGH is used to test a convex aspheric optics. A Fizeau interferometer is used again in this measurement. A schematic drawing of the system setup is given in Figure 5.2.

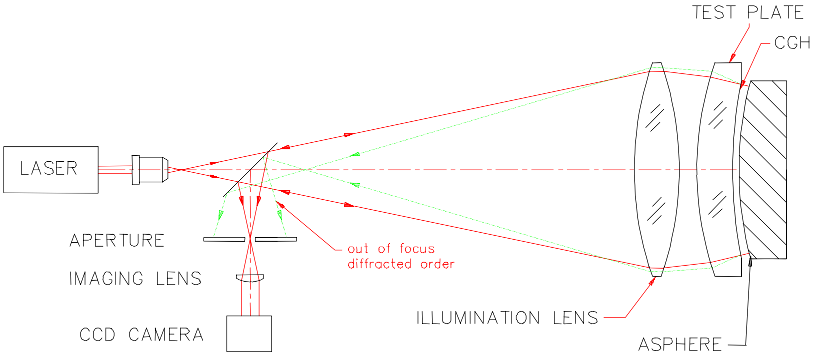

Figure 5.2. Asphere metrology setup using Fizeau interferometer with a chrome-on-glass CGH.

The CGH pattern is written on a glass substrate with a spherical shape. The CGH test plate is placed close to the test surface during the measurement procedure. The CGH used in the measurement is designed to produce a wavefront that matches the shape of the ideal test asphere. An enlarged drawing of the test plate and the asphere under measurement is shown in Figure 5.3

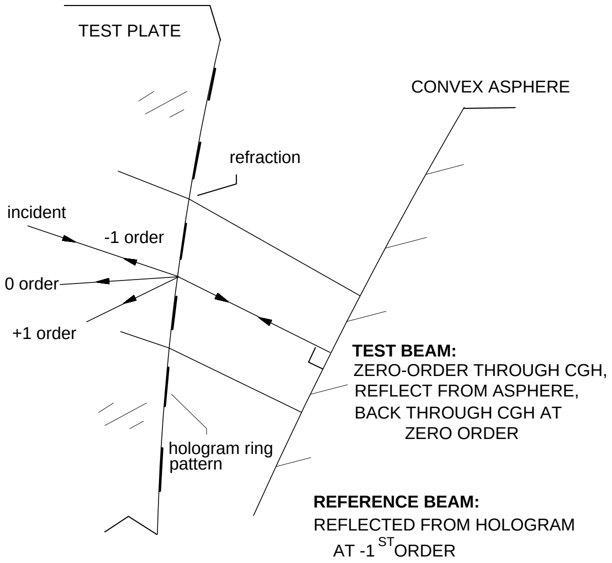

Figure 5.3. Schematic drawing shows the constructions of the test and the reference wavefronts.

The test plate is illuminated with coherent light. A portion of the incident light transmits through the test plate at zero diffraction order and strikes the asphere at normal incident for all points. This transmitted beam is retro-reflected by the asphere surface to form the test wavefront. The test wavefront passes through the hologram again at zero diffraction order where the wavefront is not deflected by the hologram. The reference wavefront of the setup is formed by the –1 diffraction order beam reflected off the CGH surface.

The reference beam retraces the incident beam path as indicated in the drawing above. The test wavefront and the reference wavefront coincide everywhere in the system except between the gap of the asphere and the test plate. The CGH on the concave spherical reference behaves like a beam-splitter in this configuration that separates and recombines the reference and the test wavefronts.

The chrome-on-glass CGH is assumed to produce –1 reflected diffraction order for the reference beam and transmitted zero order for the test beam. In this example, the index of refraction of the glass test plate is n_{glass}=1.5, and the index of refraction of the chrome coating is n_{chrome}=3.6-i4.4. The chrome layer thickness is 50 nm. The hologram fringe pattern has a 20% duty-cycle, and the average fringe spacing on the hologram is approximately 100 um. The hologram pattern has an radial pattern distortion of 1um. The test plate has $\lambda/10$ rms figure error on both the front and the back surface. Table 5.3 summarizes the stated parameters for the chrome-on-glass CGH.

Table 5.3. Chrome-on-glass CGH structure parameters.

Parameters	**Values**
Grating Type	Binary Chrome-on-glass Grating
Material (chrome)	n_{chrome} = 3.6-i4.4
Material (glass)	n_{glass} = 1.5
Reference Beam	-1 reflected order (glass-cr)
Test Beam	0 transmitted order (glass-cr)
Averaging Grating Period	100 um
Substrate Figure Errors	$\lambda/10$ rms
Pattern Distortion	1 um
Chrome Thickness	50 nm ± 2 nm
Grating Duty-cycle	20% ± 2%

As described earlier that both the test and the reference beams pass through the CGH in this configuration; both beams travel through the test plate via the same optical path. Optical interferometry is a relative measurement of the wavefront difference between the reference and the test wavefront; common errors in both wavefronts are cancelled in the final measurement results. In our example, test plate figure errors on the front surface may be neglected because the common path configuration. Figure errors on the CGH surface may not be ignored, since it directly affects the reference wavefront function; this error is included in the reference wavefront calculation. Wavefront phase errors in both the reference and the test beams induced by hologram pattern errors are determined independently for each beam, since the two beams are generated by the CGH at different diffraction orders.

Table 5.4. Diffraction wavefront phase errors from CGH fabrication uncertainties.
(A). Reference Wavefront: –1 order reflected beam (Glass-Cr):

Source of Errors	**Fabrication Tolerances**	**Wavefront Phase Errors**
RMS Substrate Figure Error* (CGH Surface)	λ/10	*(λ/5)**
Pattern Distortion	±1 um	±λ/100
Chrome Thickness Error	±2 nm	0
Duty-cycle Error	±2%	0
Root-Sum-Squared Errors :		λ/100

*CGH surface figure error may be removed using CGH surface figure measurement.

Table 5.4. **(**continued) Diffraction wavefront phase errors from CGH fabrication uncertainties.

(B). Test Wavefront: zero order transmitted beam (Glass-Cr):

Source of Errors	**Fabrication Tolerances**	**Wavefront Phase Errors**
Pattern Distortion	±1 um	0
Chrome Thickness Error	±2 nm	0
Duty-cycle Error	±2%	0
Root-Sum-Squared Errors :		0

As shown in Table 5.4(a), duty-cycle and chrome thickness variations have no effects on the reference wavefront. CGH duty-cycle cycle error has no effect because Equation (3.28) shows that all non-zero order diffraction wavefronts are independent of duty-cycle variations. The chrome thickness error has no effect because the reference beam reflects off the chrome coated surface figure, and the chrome thickness does not affect the wavefront phase function of the reference beam. For the test wavefront (Table 5.4b), wavefront phase function is independent of the pattern distortion, the chrome thickness errors and the duty-cycle variations. CGH pattern distortion has no effect because Equation (3.26) shows that zero-order diffraction beam is free of distortion. Chrome thickness error does not affect the test wavefront phase function because the chrome coating is assumed to be 100% reflective (opaque); test beam has zero amplitude at where the CGH surface is coated with chrome.

The dominant source of errors for this example is from the CGH surface figure deviations. This error can be measured and eliminated. Figure 5.4 shows the configuration of the CGH surface figure measurement.

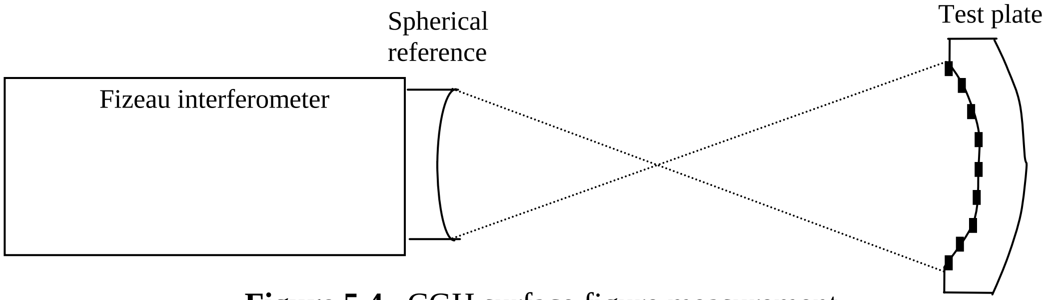

Figure 5.4. CGH surface figure measurement.

The test plate is measured at zero diffraction order, where the diverging test beam retro reflect off the CGH surface. The accuracy of this measurement is affected by the hologram pattern on the test plate surface. In this measurement, chrome thickness and grating duty-cycle variations are the sources of errors. The effect of the chrome thickness error is calculated to be 0.0015815 λ/nm using the wavefront sensitivity function Equation (3.29). The sensitivity of the duty-cycle variation is determined to be 0.001897 λ/1%duty-cycle using the wavefront sensitivity function Equation (3.27). These values can also be obtained directly from Figure 3.38 and Figure 3.37.

Table 5.5. Wavefront phase errors for CGH surface figure measurement.

Source of Errors	**Fabrication Tolerances**	**Sensitivity**	**Wavefront Phase Errors**
Chrome Thickness Error	±2 nm	±0.0015815 λ/nm	±0.003163λ
Duty-cycle Error	±2%	±0.001897 λ/1%duty-cycle	±0.003794λ
Root-Sum-Squared Errors :			0.004938λ

Wavefront phase errors of the reference and the test beams due to CGH fabrication uncertainties are calculated. The dominant error source is CGH surface figure errors in this example. This error can be measured and eliminated, although errors introduced by the CGH surface measurement should be considered when removing the CGH substrate errors. Overall wavefront phase errors resulted from the CGH fabrication uncertainties can be estimated as the RSS error of the reference, the test wavefront phase errors and the CGH surface measurement errors, and:

$$\delta\psi = \pm\sqrt{(\delta\psi_{\mathrm{ref}})^2 + (\delta\psi_{\mathrm{test}})^2 + (\delta\psi_{\mathrm{surf}})^2} \tag{5.1}$$

$$\delta\psi = \pm\sqrt{(0.01\lambda)^2 + (0)^2 + (0.004938\lambda)^2} = \pm 0.0115\lambda$$

Therefore, the accuracy of the asphere measurement using the stated interferometry setup and the chrome-on-glass CGH will be limited by ±0.0115λ. This error corresponds to surface measurement accuracy of ±0.00575λ rms.

CHAPTER 6

VALIDITY OF THE SCALAR DIFFRACTION MODEL IN CGH ANALYSIS

Scalar diffraction models are commonly used for the design and the analysis of diffractive elements because of their computational simplicity over rigorous models. New generation CGHs with high performance contains wavelength-scaled diffraction features. It is not obvious whether scalar diffraction analysis is still valid under this condition. In this chapter, validity of the scalar diffraction models for CGH analysis will be studied by analyzing hologram wavefront phase sensitivities to the changes of the state of polarization of the incident beam.

The chapter begins by introducing the concept of rigorous diffraction models and Fourier modal method (FMM). Numerical analysis of linear binary gratings are given. Diffraction wavefront phase and efficiency functions for linear gratings with various spatial frequency, etching depth and duty-cycles are calculated using the rigorous model.

The results of the analysis are then used to model binary zone plates. Wavefront phase variations due to changes in the polarization characteristics of the incident fields are studied.

6.1. RIGOROUS ANALYSIS OF GRATING DIFFRACTION

Recent advances in the field of micro-lithography have dramatically improved the capabilities of CGH fabrications. Nowadays, diffractive optical elements (DOE) with micrometer or sub-micrometer structures may be fabricated at high precision and low cost. Reduction in the minimum manufacturable diffraction feature size has led to a new generation of computer-generated holograms with higher diffraction efficiency. The analysis and the designs of this type of CGHs, however, require more rigorous mathematical models than the scalar diffraction theory.

In scalar diffraction model, light is assumed to propagate in a linear, isotropic, homogeneous and non-dispersive media. All components of the electric and the magnetic fields behave identically; they can be fully described by a single homogeneous scalar wave equation. Scalar diffraction theory also requires that: the size of the diffracting feature to be much large compare to the wavelength of the incident light; and the observation plane must not be too close to the diffracting surface. With these assumptions and limitations, scalar diffraction theory offers an approximate solution to diffraction problems. It is generally preferred because of its computational simplicity. Scalar diffraction models are typically used on diffraction gratings with the minimum feature size that is greater than 10 wavelengths of the incident light.

In rigorous diffraction models, couplings between the various components of electric and the magnetic fields are taken into account. A complete set of wave equations and the associated boundary conditions are solved exactly without introducing any approximation. Although rigorous diffraction method provides a general solution and can be applied to all diffraction problems, analytical solutions from this model are difficult to achieve due to its mathematical complexity. Over the years, a handful of numerical solutions have been proposed based on the rigorous models. For the purpose of this dissertation, we will not discuss each of the solutions in detail since several excellent reviews on this topic are available **[Petit 1980; Huntley 1982; Mayster 1984]**. In this paper, Fourier modal method (FMM) is chosen and used for the study on the validity of the scalar diffraction model.

Fourier modal method (FMM), which is also referred to as couple wave method **[Moharam and Gaylord 1986]**, is considered one of the simplest and most efficient rigorous diffraction solutions **[Li 1996]**. In the FMM, periodic grating structure, as well as the diffracted field, are expressed in the form of Fourier series. The Fourier expression helps to reduce the mathematical complexity of the boundary problem. In order to stay within the scope of this dissertation, only a brief discussion of the FMM is presented in the following.

Fourier Modal Method

Figure 6.1 shows a simple diffraction grating geometry, where the space is divided into three regions labeled as I (Z < 0), II (0≤ Z ≤ h) and III (Z > h). The media in Region I and Region III are supposed to be homogeneous. Region II consists of a periodic structure, which is modulated in the *x*-direction but is invariant in the *y*-direction. This periodic structure allows the decomposition of the TE and the TM components of the electromagnetic field inside Region II **[Herzig 1997]**.

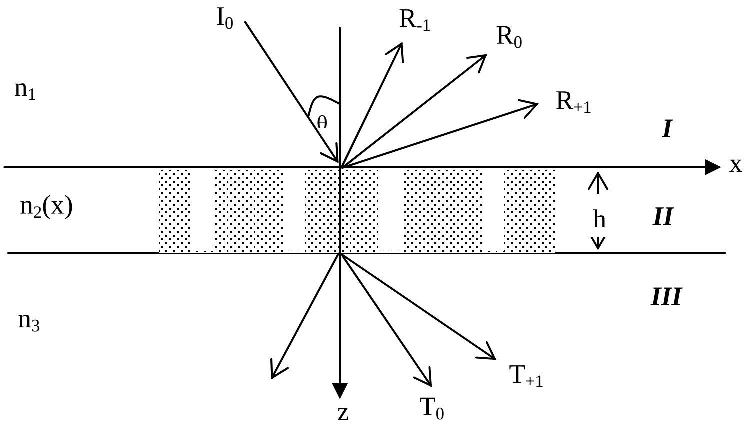

Figure 6.1. Geometry of the grating diffraction problem.

A unit amplitude monochromatic plane wave (I_0) with wavelength λ incident from Region I onto Region II at an angle θ with respect to the z-axis in the *xz*-plane. The diffracted fields in both Region I and Region III are expressed as series of plane waves:

$$U_I(x,z) = \sum_{m=-\infty}^{\infty} R_m \exp\left[i(\alpha_m x + r_m z)\right] \tag{6.1}$$

$$U_{III}(x,z) = \sum_{m=-\infty}^{\infty} T_m \exp\{i[\alpha_m x - t_m (z-h)]\} \tag{6.2}$$

where

R_m = complex amplitude of the reflected diffraction beam;

T_m = complex amplitude of the transmitted diffraction beam;

m = diffraction order;

$\alpha_m = kn_1 \sin\theta + 2\pi\, m/d$;

$r_m^2 = [(kn_1)^2 - \alpha_m^2]$;

$t_m^2 = [(kn_3)^2 - \alpha_m^2]$;

$k = 2\pi/\lambda$.

The electromagnetic field inside Region II can be decomposed into two orthogonal components TE (electric-field vector parallel to the grating grooves) and TM (electric-field vector perpendicular to the grating grooves). In the TE polarization direction, the field can be separated as $E_y(x,z)=X(x)Z(z)$ and applied into the Helmholtz wave equation:

$$\frac{d^2}{dx^2} X(x) + \left[k^2 \hat{\varepsilon}_r(x) - \gamma^2\right] X(x) = 0 \tag{6.3}$$

$$\frac{d^2}{dz^2} Z(z) + \gamma^2 Z(z) = 0 \tag{6.4}$$

where

$\hat{\varepsilon}_r(x)$ = complex relative permittivity;

γ^2 = separation constant.

The solutions of Equation (6.4) can be expressed as:

$$Z(z) = A \exp(i\gamma z) + B \exp\left[-i\gamma(z-h)\right] \tag{6.5}$$

The solution of Equation (6.3) is assumed to have a pseudo-periodic form:

$$X(x) = \sum_{m=-\infty}^{\infty} P_m \exp(i\alpha_m x) \tag{6.6}$$

The above expression is inserted into Equation (6.3) to arrive a set of linear equations that may be expressed in a matrix form **MP**=γ^2**P**. The electromagnetic field in Region II, in the TE polarization, can be expressed as:

$$E_y(x,z) = \sum_{m=-\infty}^{\infty} \sum_{n=1}^{\infty} P_{mn} \exp(i\alpha_m x)\left\{A_n \exp[i\gamma_n z] + B_n \exp[-i\gamma_n (z-h)]\right\} \tag{6.7}$$

where coefficients P_{nm} and γ_n are solved from the matrix **M** eigenvalue problem by standard numerical techniques. A similar expression can be obtained for the TM polarization field.

With the exact representations of the electromagnetic fields in all regions I-III, FMM solves the unknown parameters R_m, T_m, A_n and B_n from the electromagnetic boundary conditions.

6.2. BINARY LINEAR GRATING

In this section, FMM is used to analyze binary linear gratings with various grating period (S), depth (t) and duty-cycle (D). The linear gratings studied are chrome-on-glass gratings. The structure of the gratings is shown in Figure 6.2.

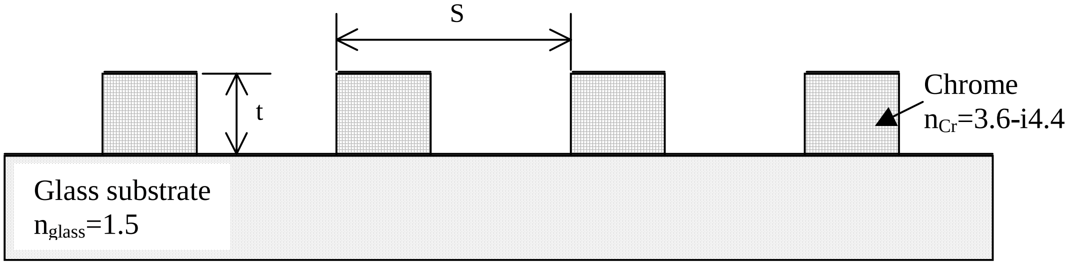

Figure 6.2. Schematic drawing of the geometry of a chrome-on-glass grating.

Lifeng Li's computer code, KAPPA, for rigorous diffraction analysis **[Li 1998]** is used here in our study. The algorithm of the computer program is based on the FMM described in the previous section. The program is capable of dealing with diffraction problems on dielectric and metallic linear gratings with arbitrary incident beam angle and state of polarization. The program computes the complex diffraction fields for both the reflected and the transmitted diffraction orders produced by the linear grating.

Complex diffraction field for the first Littrow reflection order of a linear grating is calculated for our analysis. In a Littrow configuration, the angle between the incident beam and the diffracted beam of the -1^{st} order is 180^o. Wavefront phase functions and diffraction efficiencies for both the TE and the TM polarization components of the reflected diffraction beams are studied as functions of grating period, grating depth and duty cycle. In the study, grating period is varied from 0.6λ to 5λ with 0.05λ increment; grating depth is varied from 0.1λ to 0.22λ; and grating duty-cycle is varied from 10% to 90%.

Figure 6.3 shows the calculated phase values of the TE and the TM polarization fields as a function of normalized grating period (S/λ). In this case, duty-cycle values and chrome thickness of the linear gratings are fixed at 50% and 0.15λ respectively. The phase differences between the two polarization components are minimal when grating spacing are greater than 2λ. A plot of the phase differences between the TE and the TM fields is given in Figure 6.4. A large phase deviation between the two fields occurs when the grating period is less than 1.5λ. Diffraction efficiency of the TE and the TM fields as functions of normalized grating spacing are shown in Figure 6.5.

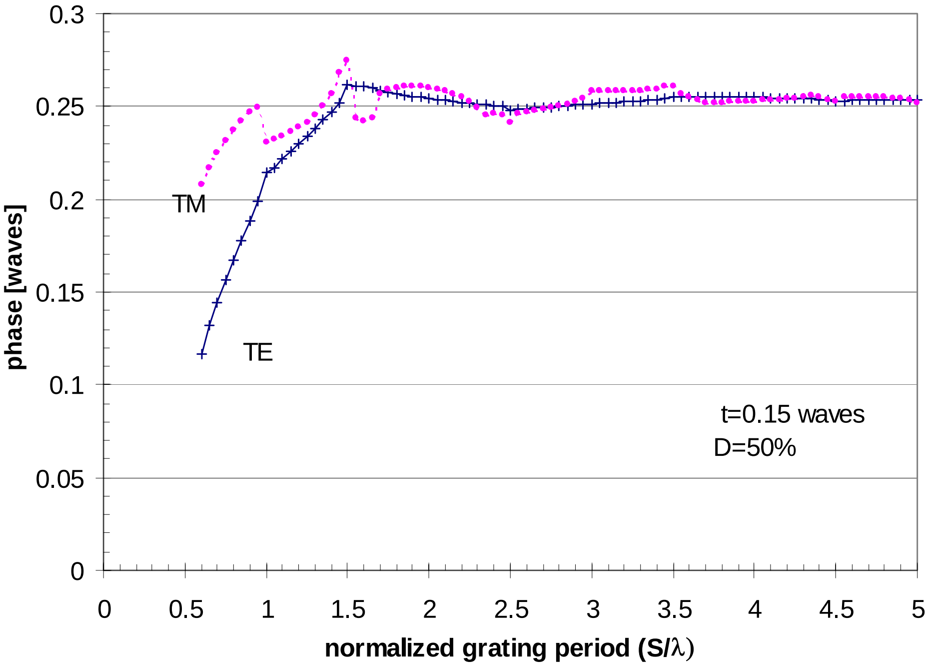

Figure 6.3. Phase values as a function of grating period for both the TE and the TM fields for a chrome-on-glass grating with 50% duty-cycle and 0.15λ chrome thickness.

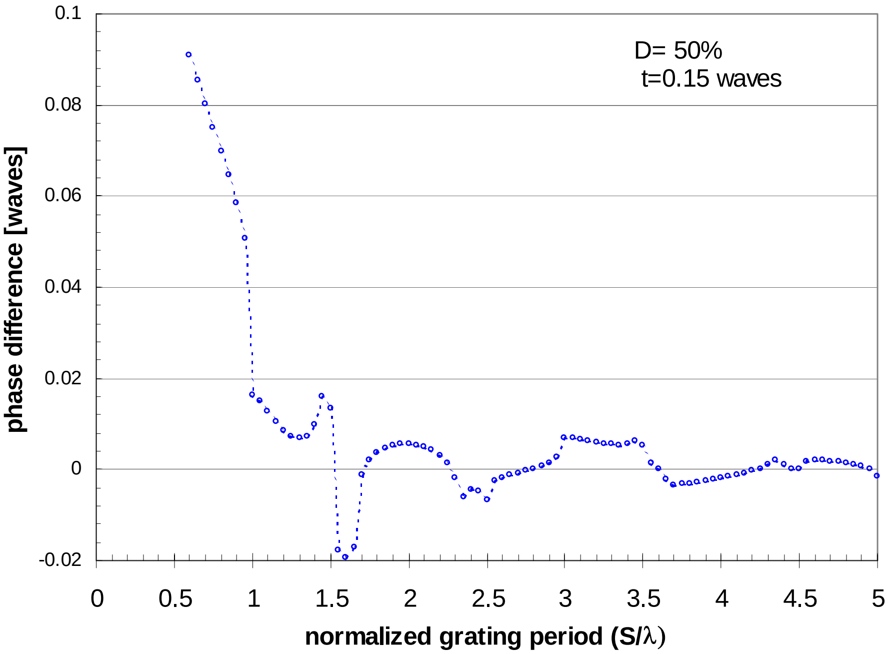

Figure 6.4. Phase differences between the TE and the TM fields as a function of grating period for a chrome-on-glass grating with 50% duty-cycle and 0.15λ chrome thickness.

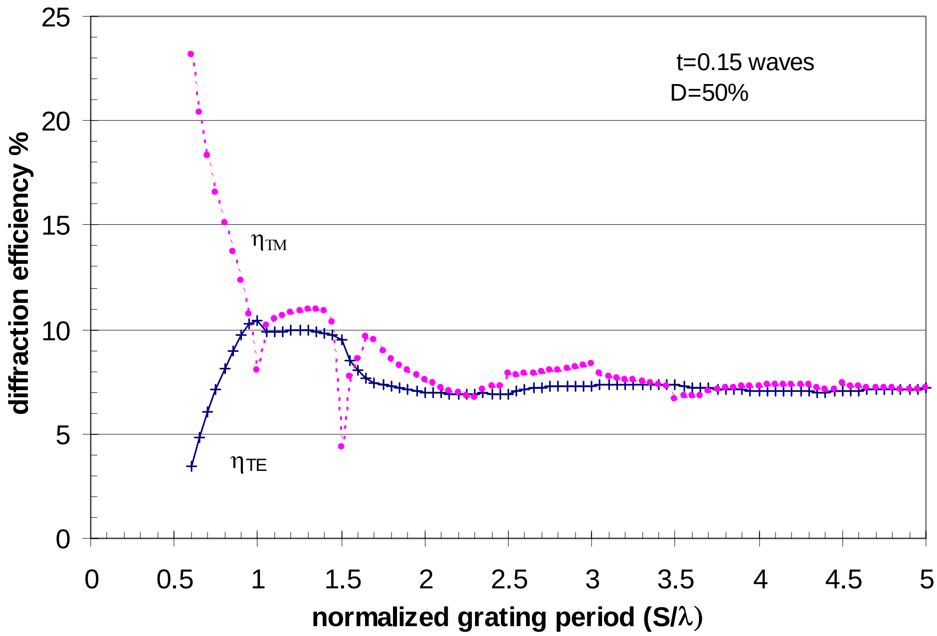

Figure 6.5. Diffraction efficiency as a function of grating period for both the TE and the TM fields for a chrome-on-glass grating with 50% duty-cycle and 0.15λ chrome thickness.

Figure 6.6 and Figure 6.7 show the phase differences between the TE and the TM polarization fields for chrome-on-glass gratings with different grating duty-cycle and chrome thickness.

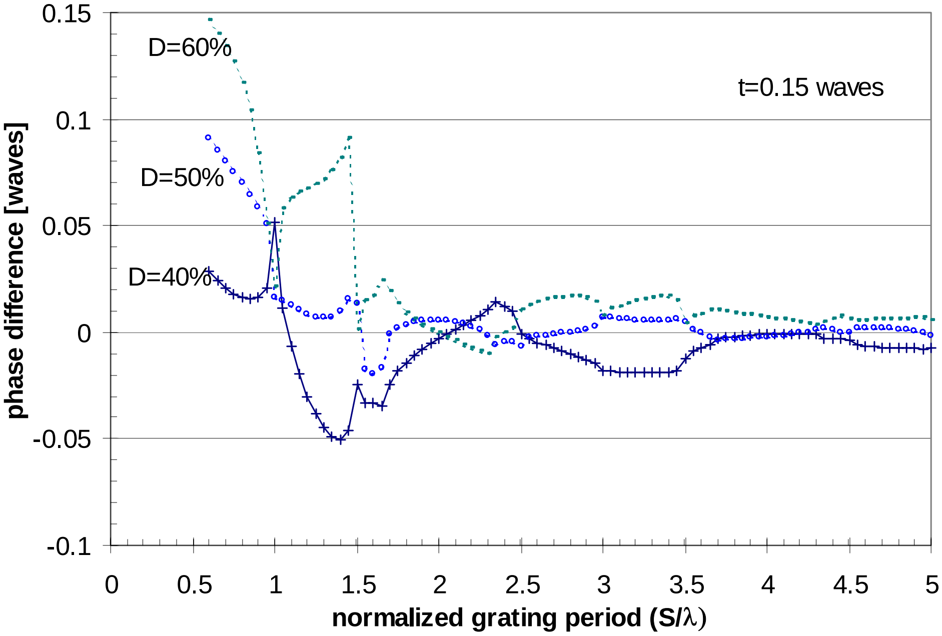

Figure 6.6. Phase differences between the TE and the TM fields as a function of grating period for a chrome-on-glass grating with 0.15λ chrome thickness at different duty-cycles.

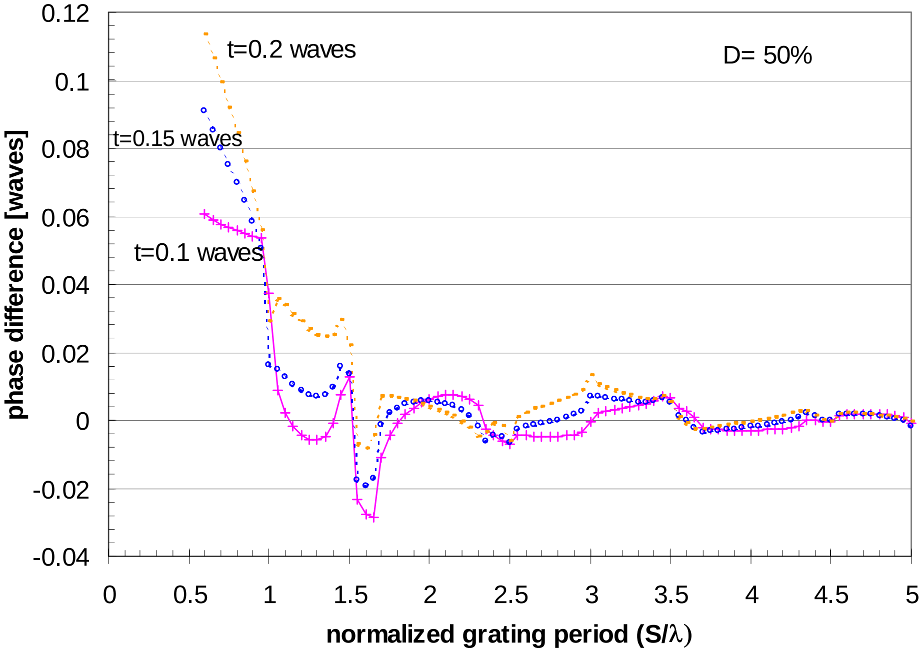

Figure 6.7. Phase differences between the TE and the TM fields as a function of grating period for a chrome-on-glass grating with 50% duty-cycle at different chrome thicknesses.

Scalar diffraction theory assumes no polarization sensitivities of the hologram to the incident wavefront. Wavefront phase difference between the TE and the TM polarization components is zero in scalar models. Rigorous diffraction models, on the other hand, take the coupling between the two polarization components in the electric field into account. Rigorous diffraction models predict different behaviors between the TE and the TM diffraction wavefronts.

The results of our analysis show that polarization sensitivity of the linear grating predicted by the rigorous theory is almost negligible when the grating period is greater than 2λ. This conclusion suggests that scalar diffraction theory may still be valid for diffraction analysis when the minimum features of the diffractive elements greater than 2λ.

6.3. BINARY ZONE PLATE

A CGH with annular ring pattern is commonly referred to as a zone plate. It is often used to test rotational symmetric optical elements in optical testing. There are several advantages associated with the use of zone plates in optical interferometry. Zone plates produce multiple diffraction orders along the optical axis. This characteristic of the zone plates simplifies the setup and the alignment procedure of the interferometry by allowing the CGH to be mounted on the same axis as the test parts **[Burge 1993]**. By preserving the axial symmetry, the design and the analysis of the hologram are also reduced from the 2-D to 1-D. Furthermore, the rotational symmetry allows a direct certification of the hologram through the verification of the positions of the rings fringes **[Burge 1993]**.

In this section, we will study binary zone plates with minimum diffraction feature size that is on the order of the wavelength of the incident wavefront using rigorous diffraction model. To simplify the analysis, the binary zone plate is modeled as a collection of linear gratings with variable grating period. The results of the rigorous diffraction analysis of the 1-D binary linear gratings from the previous section are used in our study.

6.3.1. Modeling Scheme

A zone plate consists of a collection of concentric rings, where the spacing between adjacent rings decreases as the ring radius increases (Figure 6.6). In our model, the zone plate is divided into two regions. In Region I ($r < r_0$), the smallest ring spacing is larger or equal to 5λ; and scalar diffraction analysis will be applied to this region. In Region II ($r_0 < r < R$) where the ring spacing are less than 5λ, rigorous diffraction analysis is used **[Sheng, Feng and Larochelle 1997]**.

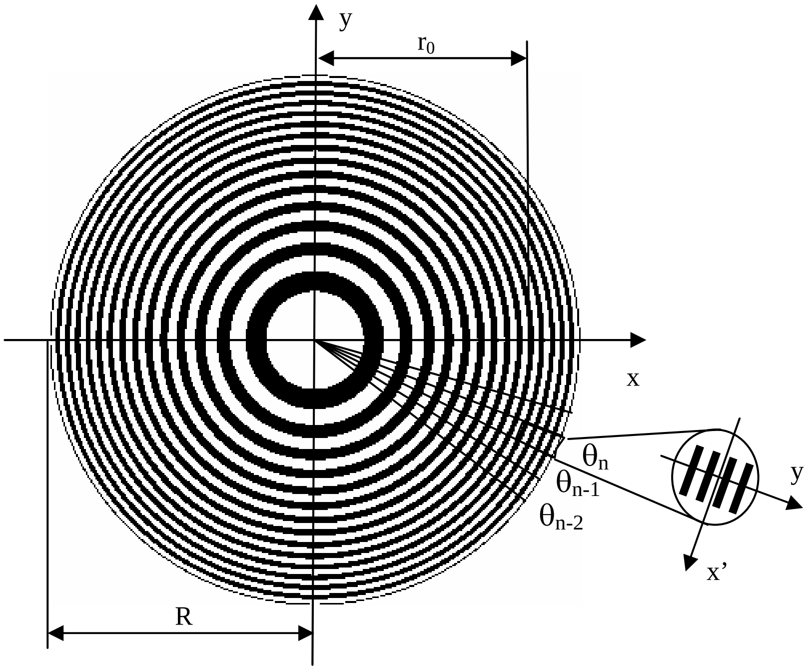

Figure 6.8. A binary zone plate.

Region II on the zone plate is further divided into N equal sections along its angular direction ($\theta_n = 2\pi i/N$, with n = 0, 1, …N-1), and M equal sections along its radial direction (r_m=mR/M, with m = 0, 1, …M). By doing so, each segment in Region II may be treated as a linear binary grating (see Figure 6.6).

A normally incident plane wavefront (E_i) is assumed to have a linear polarization. It can be mathematically expressed as:

$$E_i = \begin{bmatrix} E_x \\ E_y \end{bmatrix} \tag{6.5}$$

In order to reduce the complexity of our analysis, the incident wavefront is assumed to have a unit amplitude and a linear polarization that is parallel to either the x or the y-axis of the zone plate coordinate. A y-direction polarized incident wavefront can be expressed as:

$$E_i = \begin{bmatrix} 0 \\ 1 \end{bmatrix} \tag{6.6}$$

Separate Cartesian coordinate (x'-y') is assigned for each segment in Region II on the zone plate (see Figure 6.6). Depending on the position of the viewed grating segment on the zone plate, local coordinate defined for the segment may not align with the global coordinate of the zone plate. A y-direction polarized incident field is seen as TM polarization fields for grating segments on the zone plate where $\theta = \pi/2$ and $3\pi/2$. The same incident field is seen as TE polarization fields for grating segments on the zone plate where $\theta = 0$ and π.

The results from the rigorous analysis in Section 6.2 are given in the TE and the TM polarization directions. For grating segments on the zone plate where the orientation of the local coordinate is not aligned with either the x or the y-axis of the zone plate, results from Section 6.2 can not be applied directly. The incident electromagnetic field must be decomposed into a TE and a TM components respect to the local coordinate for each segment. The diffracted wavefront in both the TE and the TM polarization direction from these grating segments are then recombined and re-mapped back to the global coordinate of the zone plate. Mathematically, decomposition and composition process are completed with the help of the rotating matrix (**R**)

$$R(\theta) = \begin{bmatrix} \cos(\theta) & \sin(\theta) \\ -\sin(\theta) & \cos(\theta) \end{bmatrix} \tag{6.7}$$

Using the calculated diffraction efficiency and phase values from Section 6.2, complex diffraction wavefront function produced by a binary linear grating can be written as Equation 6.8 when the grating is aligned with the x or the y-axis of the zone plate.

$$T = \begin{bmatrix} \sqrt{\eta_x} e^{-i\phi_x} & 0 \\ 0 & \sqrt{\eta_y}\, e^{-i\phi_y} \end{bmatrix} \tag{6.8}$$

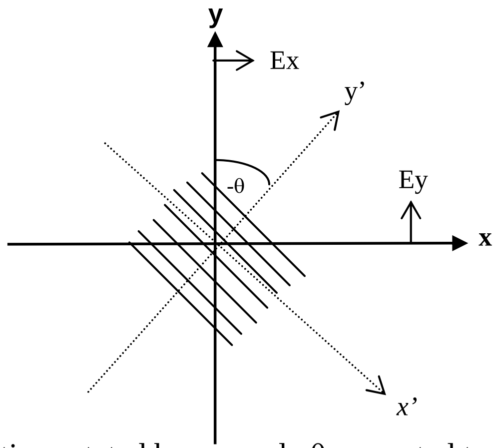

Figure 6.9. Linear grating rotated by an angle θ respected to the y-axis of the zone plate.

When the linear grating is rotated respect to the y-axis by an angle θ (see Figure 6.9), the incident field relative to the rotated coordinate system (x'-y') becomes $\mathbf{R}(\theta)\mathbf{E}^i$. The complex diffraction field from this tilted grating is simply the multiplication of the rotated field matrix and the matrix **T**. The new diffraction field matrix can then be re-mapped back to the original coordinate (x-y) using again the rotating matrix **R**(-θ). In a general form, complex diffraction field produced by a linear grating with arbitrary rotation angle respect to the y-axis of the zone plate coordinate can be written as:

$$E^{'} = \begin{bmatrix} E_x^{'} \\ E_y^{'} \end{bmatrix} = R(-\theta)TR(\theta)E_i \tag{6.9}$$

$$= \begin{bmatrix} \cos(-\theta) & \sin(-\theta) \\ -\sin(-\theta) & \cos(-\theta) \end{bmatrix} \begin{bmatrix} \sqrt{\eta_x} e^{-i\phi_x} & 0 \\ 0 & \sqrt{\eta_y}\, e^{-i\phi_y} \end{bmatrix} \begin{bmatrix} \cos(\theta) & \sin(\theta) \\ -\sin(\theta) & \cos(\theta) \end{bmatrix} \begin{bmatrix} E_x \\ E_y \end{bmatrix}$$

$$= \begin{bmatrix} E_x \cdot \left[\sqrt{\eta_x} e^{-i\phi_x} \cos^2(\theta) + \sqrt{\eta_y} e^{-i\phi_y} \sin^2(\theta)\right] \\ \qquad + E_y \cdot \left[\sqrt{\eta_x} e^{-i\phi_x} \sin(\theta)\cos(\theta) - \sqrt{\eta_y} e^{-i\phi_y} \sin(\theta)\cos(\theta)\right] \\ \\ E_x \cdot \left[\sqrt{\eta_x} e^{-i\phi_x} \sin(\theta)\cos(\theta) - \sqrt{\eta_y} e^{-i\phi_y} \sin(\theta)\cos(\theta)\right] \\ \qquad + E_y \cdot \left[\sqrt{\eta_x} e^{-i\phi_x} \sin^2(\theta) + \sqrt{\eta_y} e^{-i\phi_y} \cos^2(\theta)\right] \end{bmatrix}$$

Diffraction wavefront functions for all grating segments in Region II of the zone plate are calculated using the above relationships. The total diffraction wavefront produced by Region II of the zone plate is formed by combining the calculated wavefront functions from all grating segments. Furthermore, the complete far-field diffraction wavefront function of the entire zone plate is formed by combining the diffraction analysis results from both Region I and Region II.

6.3.2. Computer Simulation

A computer program was written in Interactive Data Language (IDL) to simulate the performance of a binary zone plate with a minimal ring spacing of 0.6λ. Relationship between the ring spacing and the ring radius on the zone plate is given in Figure 6.10.

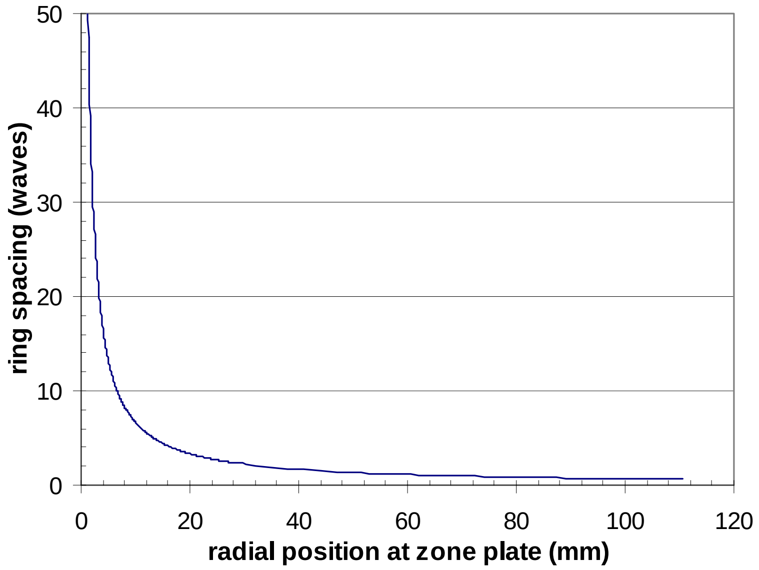

Figure 6.10. Ring spacing vs. radial position of zone plate used in the 1st-order.

The ring spacing varies in a non-linear fashion with the ring radius. The inverse ring spacing values increase linearly with the radius of the ring (see Figure 6.11). The modeled zone plate has a ring spacing of 5λ when the ring radius reaches 15 mm.

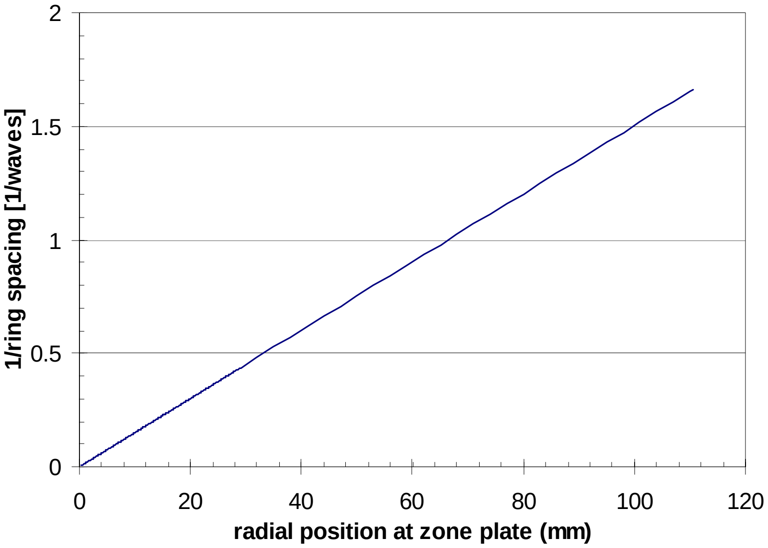

Figure 6.11. Inverse ring spacing vs. radial position of zone plate used in 1st-order.

In our computer simulation, Region II of the zone plate is divided into 360 sections in the angular direction and 89 sections along the radial direction. The incident wavefront is assumed to have a linear polarization that is parallel to the x-axis of the zone plate (*Ex* = 1 and *Ey* = 0). The results of the computer simulation are given in Figure 6.12 through Figure 6.16. The complex diffraction wavefront phase and efficiency functions for both the TE polarization and the TM polarization wavefront produced with a TE polarized incident field are given in Figure 6.13 and Figure 6.14 respectively.

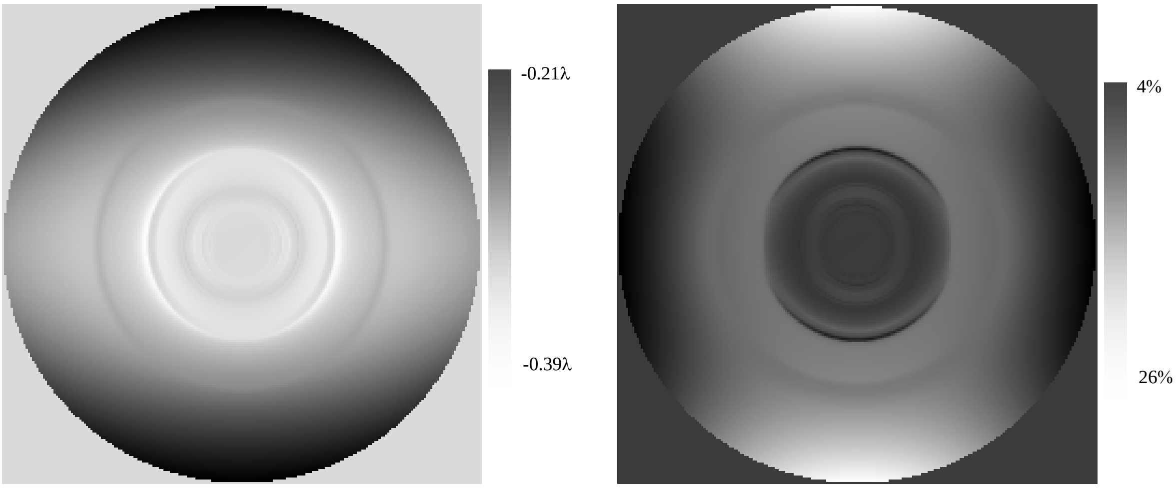

(a) wavefront phase **(b)** diffraction efficiency

Figure 6.12. Calculated wavefront phase and diffraction efficiency fucntion for the TE polarization wavefront with TE polarized incident field.

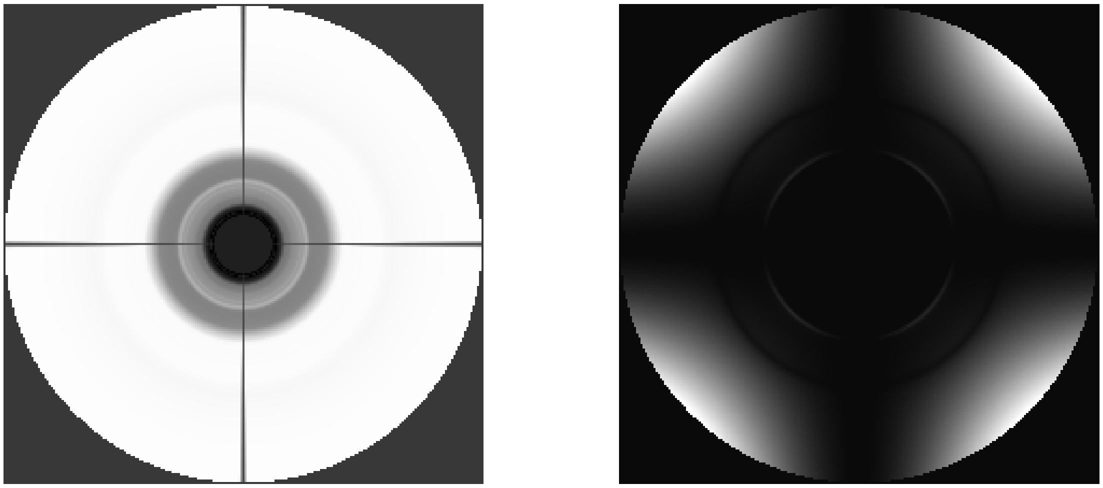

(a) wavefront phase **(b)** diffraction efficiency

Figure 6.13. Calculated wavefront phase and diffraction efficiency function for the TM polarization wavefront with TE polarized incident field.

Profile plots of the wavefront phase and diffraction efficiency functions shown in Figure 6.12 are given in Figure 6.14 and Figure 6.15.

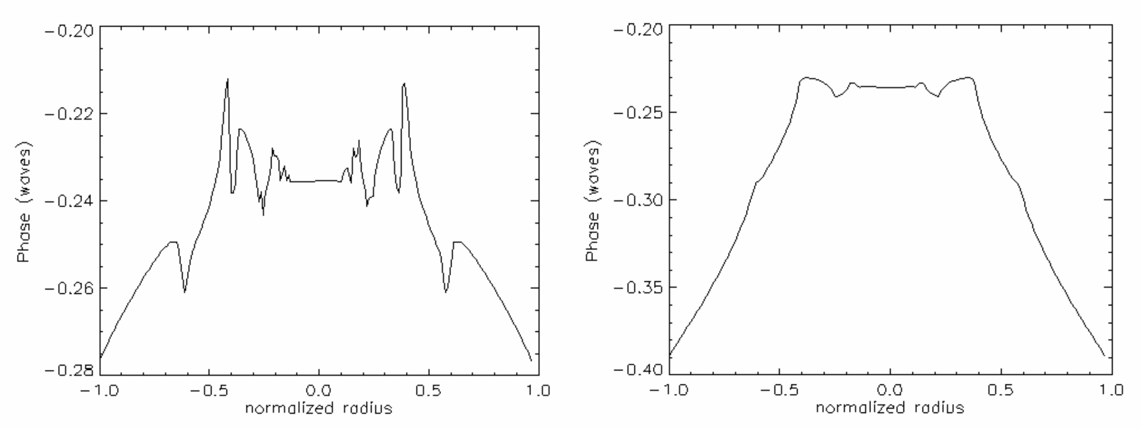

(a) x-axis profile **(b)** y-axis profile

Figure 6.14. Profile plots of the calculated wavefront phase function for the TE polarization wavefront with TE polarized incident field.

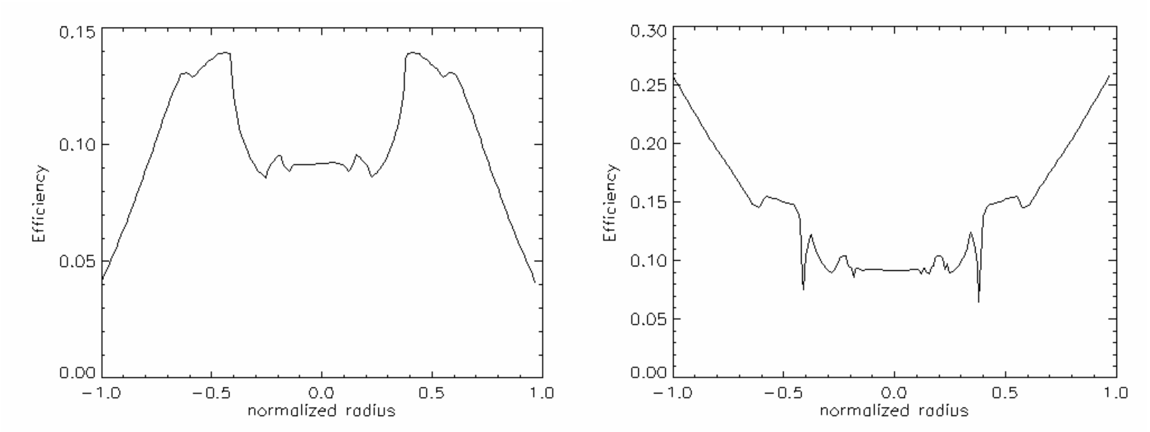

(a) x-axis profile **(b)** y-axis profile

Figure 6.15. Profile plots of the calculated diffraction efficiency function for the TE polarization wavefront with TE polarized incident field.

Because of the rotational symmetry of the zone plate, a TM polarized incident field produces a diffracted wavefront that is orthogonal to the wavefront produced by a TE polarized incident field. The phase and the diffraction efficiency functions for the TM polarization wavefront with a TM polarized field are shown in (Figure 6.16)

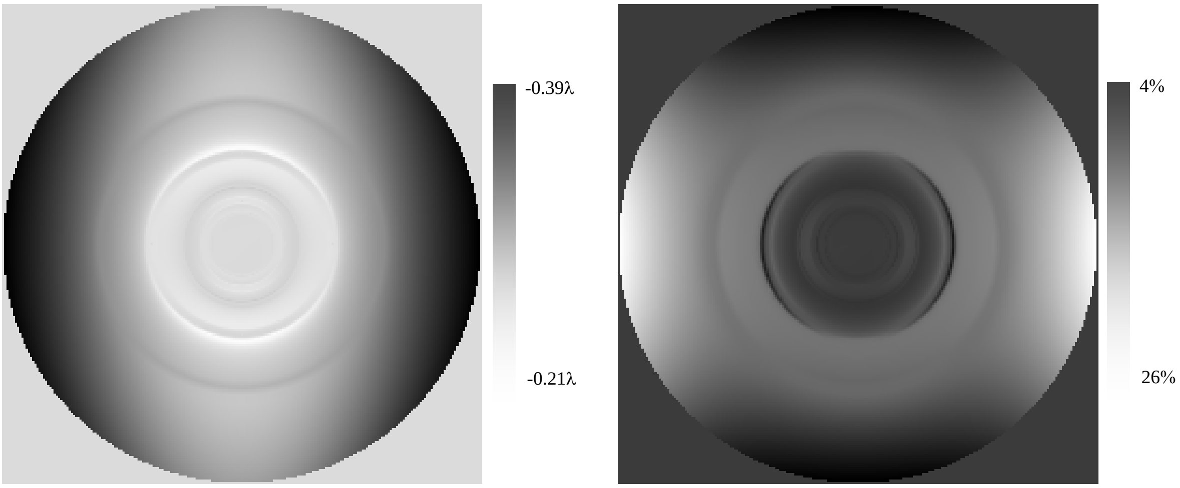

(a) wavefront phase **(b)** diffraction efficiency

Figure 6.16. Calculated wavefront phase and diffraction efficiency function for the TM polarization wavefront with TM polarized incident field.

Rigorous diffraction models predict that diffraction wavefront functions are sensitivity to the state of polarization of the incident field. Different diffractive wavefront functions are obtained by our model when the polarization direction of the incident field is varied from TE to TM direction. The phase differences between the TE and the TM polarization wavefronts are presented in Figure 6.17. Both x and y-direction profiles plots of the phase difference function is given in Figure 6.18.

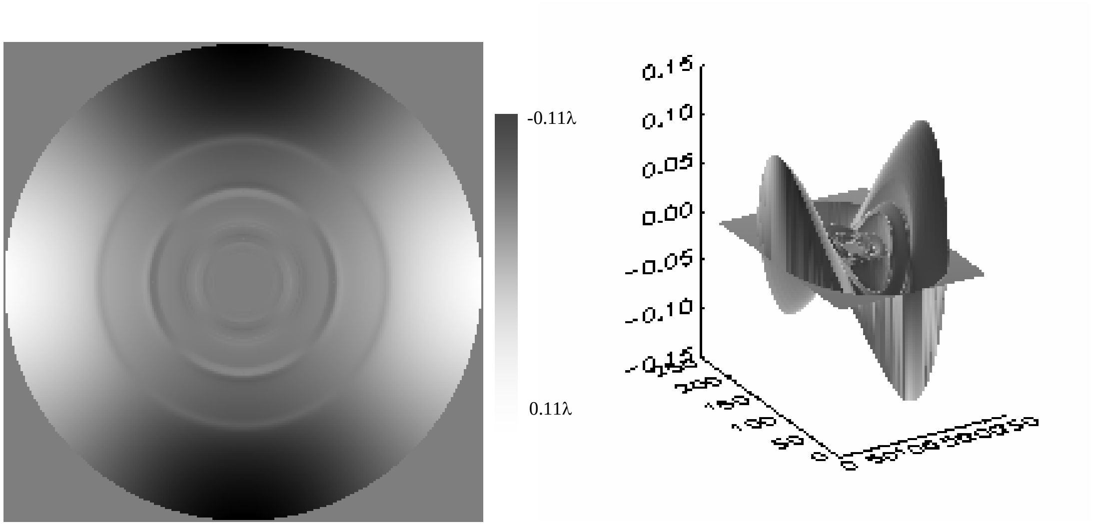

(a) phase difference map **(b)** 3-D plot of the phase difference map

Figure 6.17. Calculated wavefront phase difference between the TE and the TM polarization wavefronts.

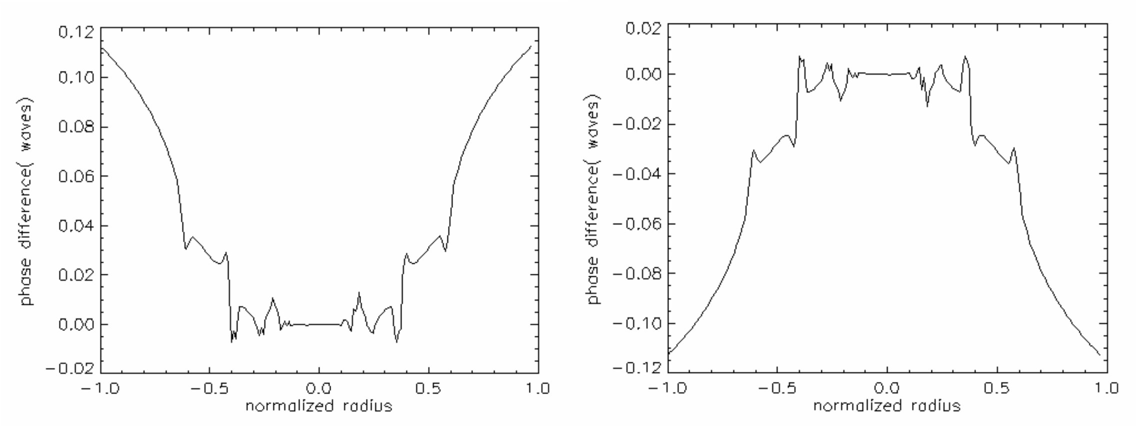

(a) x-axis profile **(b)** y-axis profile

Figure 6.18. Profile plots of the calculated phase difference between the TE and the TM polarization wavefronts.

In our simulation, the smallest ring spacing on the zone plate is 0.6λ. A 0.22λ peak-to-valley phase difference between the TE and the TM polarization wavefronts is observed at the edge of the zone plate. It is also indictated in Figure 6.18 that the phase differences between the TE and the TM polarization wavefronts are less than 0.02λ for zone plate regions where the ring spacings are greater than 2λ.

Scalar diffraction theory predicts no polarization sensitivity of diffractive elements. Rigorous diffraction models must be applied to holograms with wavelength-scaled diffraction features. The result of our simulation indicates, however, changes in the polarization state of the incident field has minimal effects on the diffraction wavefront phase functions for diffractive elements with minimum feature size that is greater than 2λ. In the following chapter, we will verify this conclusion with experimental data. A binary chrome-on-glass grating is fabricated and mesured using a phase-shifting interferometer with both TE and TM polarized incident fields.

CHAPTER 7

POLARIZATION SENSITIVITIES OF CGHS WITH ANNULAR RING PATTERN

The simulation results of the binary zone plate obtained from the previous chapter suggest that the scalar diffraction model may still provide reasonably accurate results for CGHs with feature size that is greater than 2λ. In this chapter, we will verify the theoretical analysis with experimental results. The polarization sensitivity for hologram with annular ring patterns will be studied using a phase shifting interferometer. Wavefront phase variations between different polarization fields are analyzed.

7.1. HOLOGRAM DESCRIPTION

The CGH used in our experiments has a binary ring-pattern. The hologram is constructed with a plane bare glass substrate and a thin chrome layer. The diffraction features of the hologram were generated using a direct laser beam writing method. This process relies on a thermo-chemical reaction of the chrome layer to generate desired patterns. The diffraction grating pattern is written directly onto the chrome layer; it eliminates difficulties in applying and controlling photo-resist in conventional manufacturing process **[Burge 1995]**.

Figure 7.1. demonstrates the four basic steps of the direct beam writing process. First, a thin chrome layer with a 50 to 100 nm thickness is coated onto the glass substrate. During the writing process, focused laser beam raises temperature at selected regions on the chrome surface where thermo-oxidation takes place. Local areas of the chrome layer become chrome-oxide (Cr_2O_3) that forms a latent image of the hologram pattern. The hologram may later be cleaned with NaOH + $K_3Fe(CN)_6$ solvent, where the un-oxidized chrome layer is dissolved. The remaining chrome-oxide image on the glass substrate forms the finished hologram.

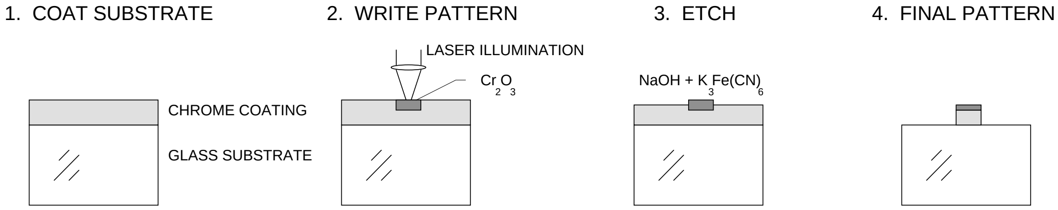

Figure 7.1. Direct beam writing process using thermo-chemical reaction.

A reflection CGH is used in the experiments. It was designed to generate a spherical wavefront with 132.96 mm radius of curvature at 632.8 nm wavelength in the first diffraction order. A 2-D surface height map of the hologram near its central area is shown in Figure 7.2. This surface map is captured using a microscope with a 10x magnification. A cross pattern seen in the center of the hologram is a test mark used to accurately locate the center of the hologram during the fabrication process.

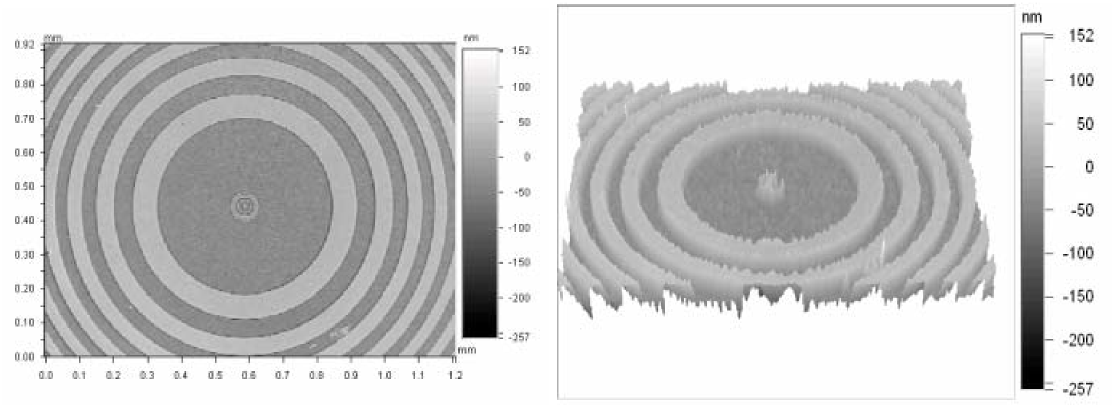

Figure 7.2. Surface profiles of the central area of the hologram.

The hologram has a circular aperture with a diameter of 58 mm. It contains 9879 rings where the spacing between adjacent rings in the hologram decreases with increasing ring radius. The largest ring spacing is 141 um (222.8 waves) at the center, and the smallest ring spacing is 1.484 um (2.35 waves) at the edge of the hologram. The ring pattern on the hologram has a 50% duty-cycle and the chrome thickness is 100 nm.

Figure 7.3 shows the relationship between the ring spacing and the ring radius in the zone plate. The ring spacing becomes less than 5λ when the ring radius exceeds 13 mm. Both TE and TM fields of the diffraction wavefront off the hologram will be measured using a phase shifting interferometer and compared with computer simulation results.

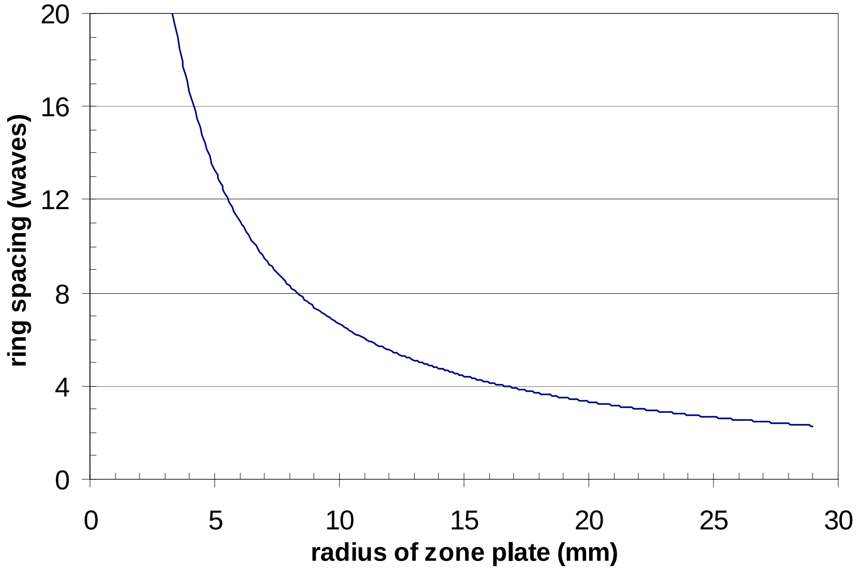

Figure 7.3. Ring spacing vs. ring radius of the hologram.

7.2. COMPUTER SIMULATION

The zone plate model derived in section 6.3 is used here for calculating both TE and TM polarized diffraction wavefronts from the binary-ring hologram. The parameter M is chosen to be 360 and the parameter N is set to be 70 in the computer model. A linear grating profile with 0.157 waves etched depth and 50% duty-cycle is applied to the model to match the parameters of the real hologram.

The calculated wavefront phase maps for both TE and TM components of the diffraction beam are presented in Figure 7.4 through Figure 7.7. The incident wavefront is assumed to be linearly polarized. Figure 7.4(a) and (b) show the calculated wavefront phase maps for both the TE and the TM polarized incident beams respectively.

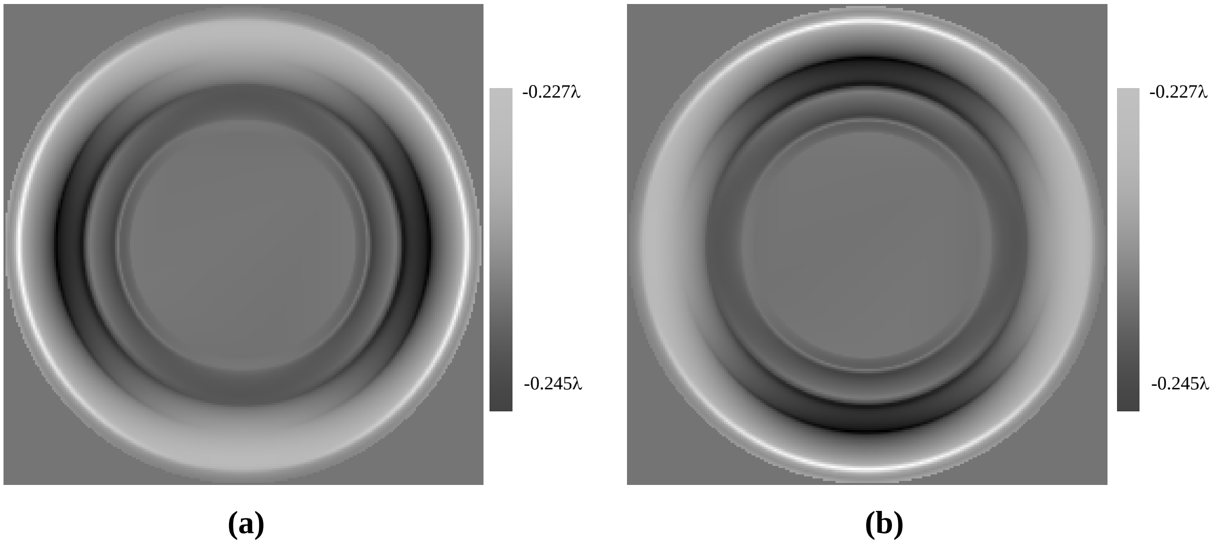

Figure 7.4. Calculated phase maps for incident beam in (a) TE mode and (b) TM mode.

As shown in the figures above, different diffraction wavefront phase functions are produces when the polarization state of incident wavefront is varied. Because of the rotational symmetry of the ring–patterned hologram, however, the phase functions for the TE and the TM polarized incident beams share essential the same mathematical form but orthogonal to each other. Profile plots of the phase maps in both horizontal and vertical directions are given in Figure 7.5(a) and (b).

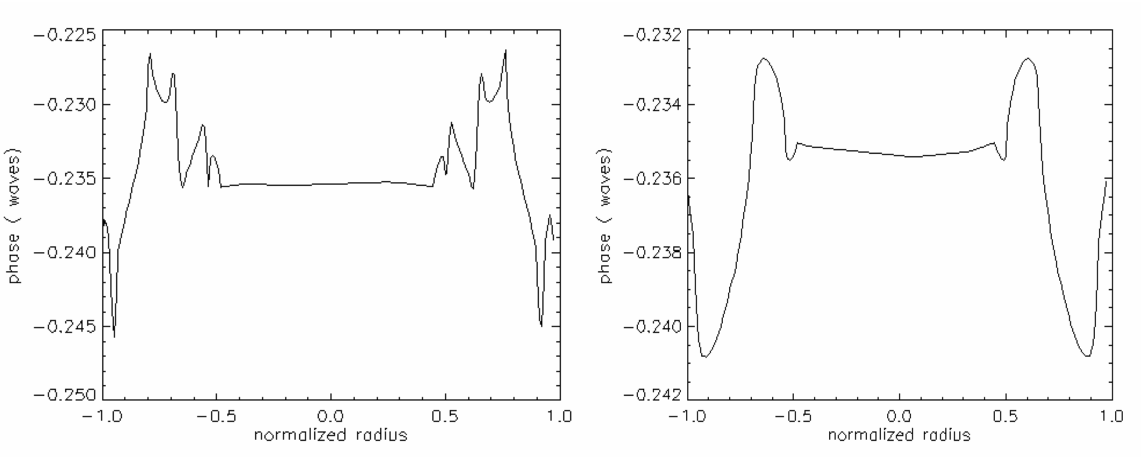

(a) horizontal profile **(b)** vertical profile

Figure 7.5. Profile plots of phase map produced by TE incident beam.

The wavefront phase difference between the TE and the TM fields is shown in Figure 7.6 and Figure 7.7.

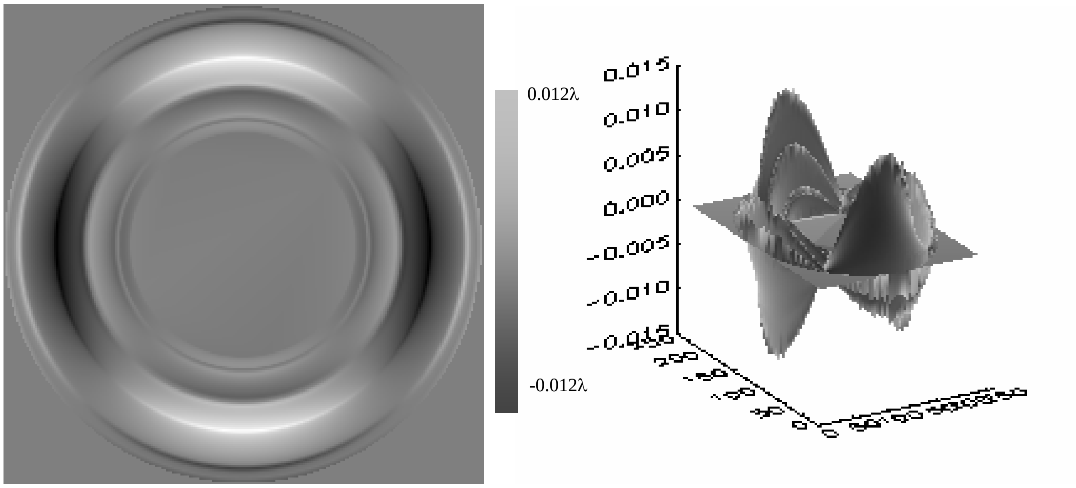

Figure 7.6. Phase difference between TE and TM fields.

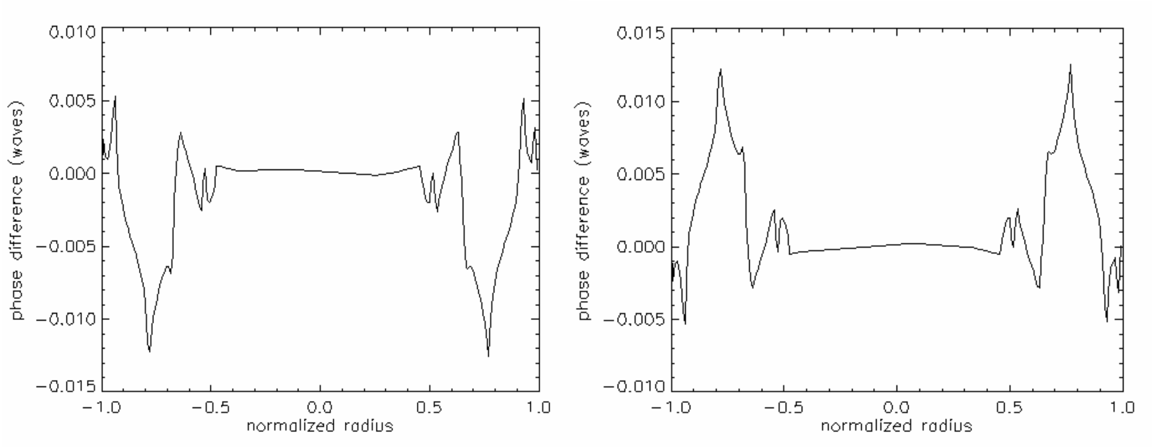

(a) x-axis plot **(b)** y-axis profile

Figure 7.7. Phase difference profiles

The maximum phase difference between the TE and the TM fields predicted by computer simulation is 0.024λ. In the following section, this conclusion will be compared with experimental data.

7.3. EXPERIMENTAL PROCEDURES AND RESULTS

7.3.1. Measurement Procedures

A phase-shifting Fizeau interferometer was used to measure the diffraction wavefront phase functions of the CGH. The experimental set-up is illustrated in Figure 7.8. The hologram was measured exactly as if it was a concave sphere and positioned 132.96 mm behind the focal spot of the test beam. The hologram has an equivalent f/# of

2.3; and a f/1.5 reference sphere was chosen for the experiments in order to have a complete coverage of the entire hologram.

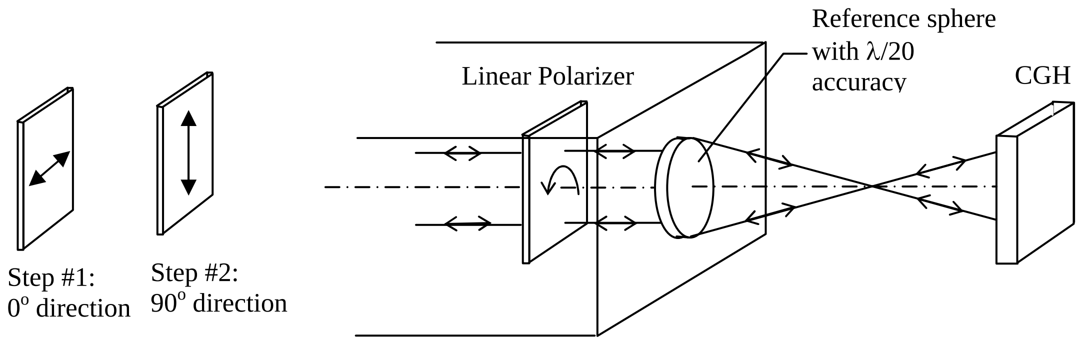

Figure 7.8. Experimental setup for CGH polarization sensitivity measurement.

In order to study the sensitivities of the diffraction wavefront as a function of the polarization states of the incident beam, the CGH was measured with linearly polarized test beams in both TE and TM modes. The original output beam from the interferometer was pre-examined to be circular polarized. A linear polarizer was placed inside the interferometer in a collimated beam path before the reference sphere. The polarization state of the modified test beam may therefore be controlled by adjusting the orientation of the linear polarizer (see Figure 7.8).

7.3.2. Experimental Results

In order to reduce random errors in the measured wavefront phase function, the sample hologram was measured eight times for each linear polarized incident fields (TE and TM). Figure 7.9 and Figure 7.10 show the averaged phase maps calculated from each set of the eight measurements for the TE and the TM polarization field respectively.

In order to reduce alignment errors, i.e., tilt and defocus of the sample hologram, during the interferometric measurements, wavefront tilt and power are removed from the raw phase maps.

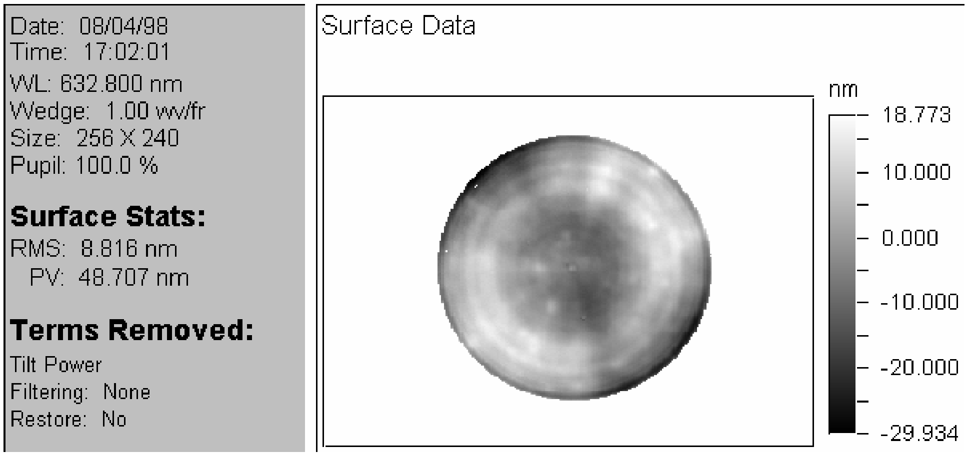

Date: 08/04/98
Time: 17:02:01
WL: 632.800 nm
Wedge: 1.00 wv/fr
Size: 256 X 240
Pupil: 100.0 %

Surface Stats:
RMS: 8.816 nm
PV: 48.707 nm

Terms Removed:
Tilt Power
Filtering: None
Restore: No

Figure 7.9. Contour plot of the diffracted wavefront for the sample CGH with TE polarized incident field.

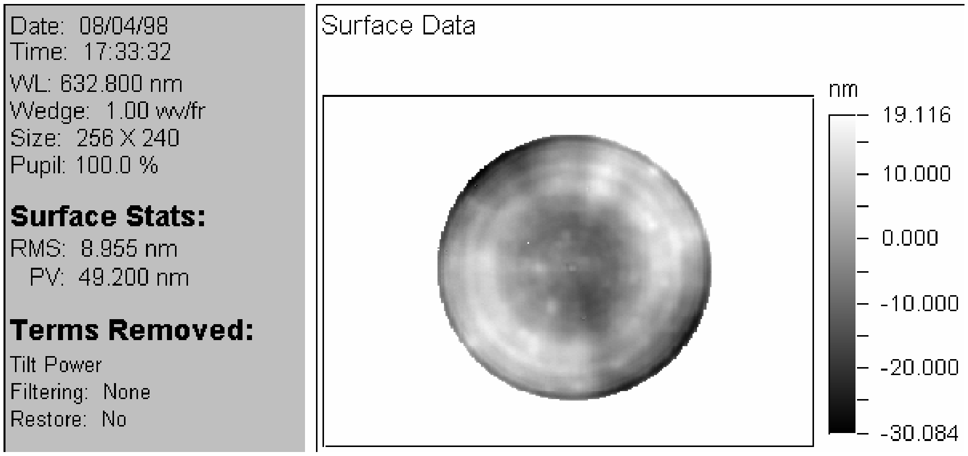

Date: 08/04/98
Time: 17:33:32
WL: 632.800 nm
Wedge: 1.00 wv/fr
Size: 256 X 240
Pupil: 100.0 %

Surface Stats:
RMS: 8.955 nm
PV: 49.200 nm

Terms Removed:
Tilt Power
Filtering: None
Restore: No

Figure 7.10. Contour plot of the diffracted wavefront for the sample CGH with TM polarized incident field.

Phase differences between the TE and the TM polarization fields were calculated by subtracting the two measured phase maps (see Figure 7.11).

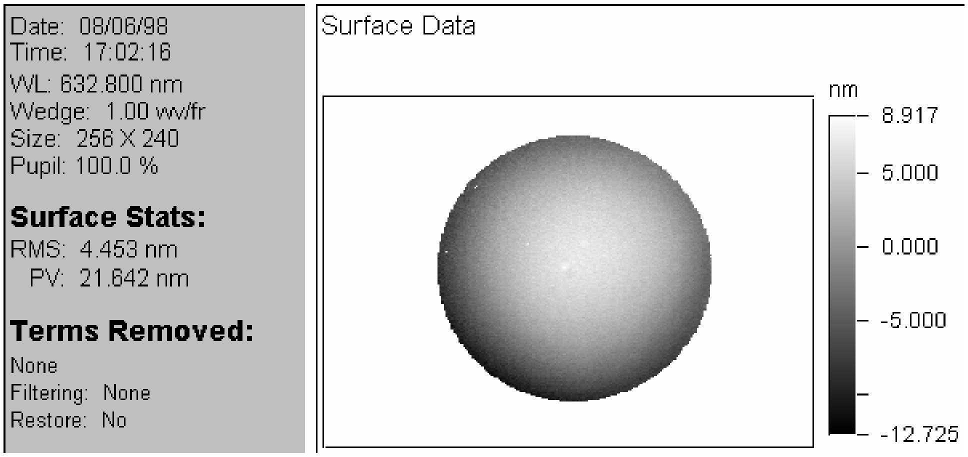
Date: 08/06/98
Time: 17:02:16
WL: 632.800 nm
Wedge: 1.00 wv/fr
Size: 256 X 240
Pupil: 100.0 %

Surface Stats:
RMS: 4.453 nm
PV: 21.642 nm

Terms Removed:
None
Filtering: None
Restore: No

Figure 7.11. Wavefront phase difference map between TE and TM polarization fields

Third-order Seidel aberration terms were removed from the raw phase difference map in order to eliminate noises in the measurement procedure and residual aberrations the interferometer. The processed phase difference map with tilt, power and third order spherical removed is shown in Figure 7.12. The data are then low pass filtered to reduce high frequency noise. The final phase difference map is shown in Figure 7.13.

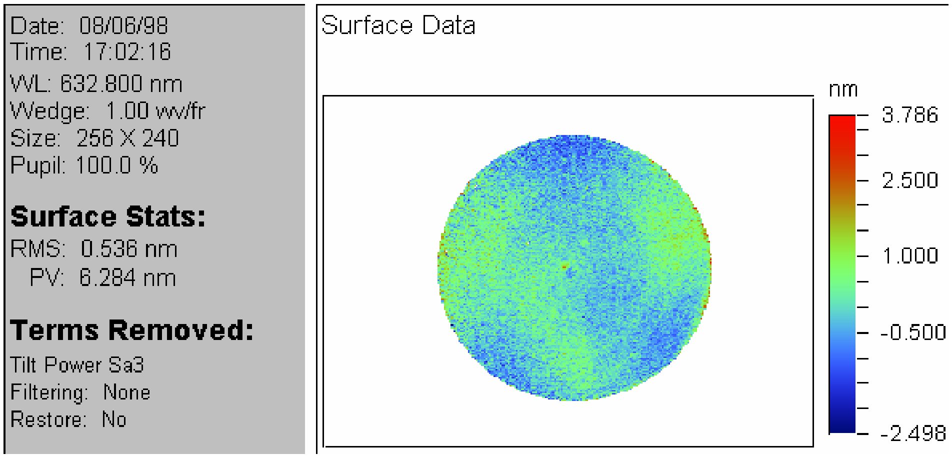
Date: 08/06/98
Time: 17:02:16
WL: 632.800 nm
Wedge: 1.00 wv/fr
Size: 256 X 240
Pupil: 100.0 %

Surface Stats:
RMS: 0.536 nm
PV: 6.284 nm

Terms Removed:
Tilt Power Sa3
Filtering: None
Restore: No

Figure 7.12. Phase difference map after removing tilt, power and 3rd order spherical.

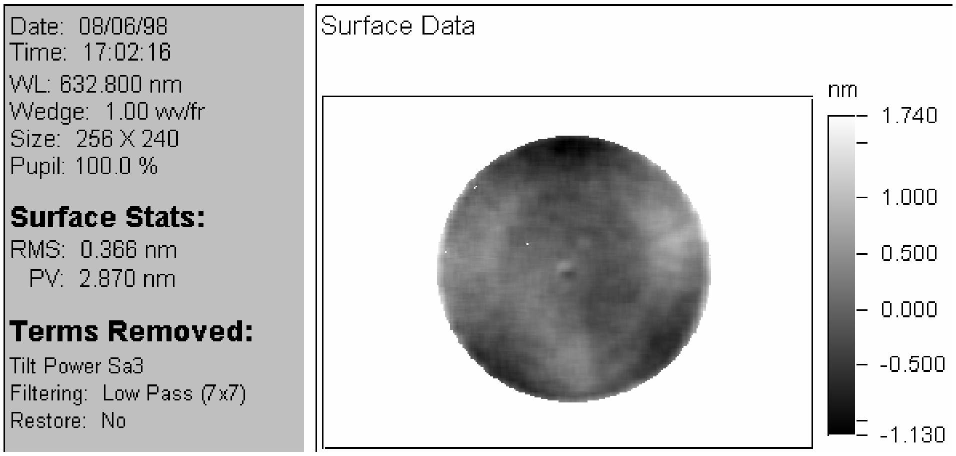

Date: 08/06/98
Time: 17:02:16
WL: 632.800 nm
Wedge: 1.00 wv/fr
Size: 256 X 240
Pupil: 100.0 %

Surface Stats:
RMS: 0.366 nm
PV: 2.870 nm

Terms Removed:
Tilt Power Sa3
Filtering: Low Pass (7x7)
Restore: No

Figure 7.13. Phase difference map after low pass filtering.

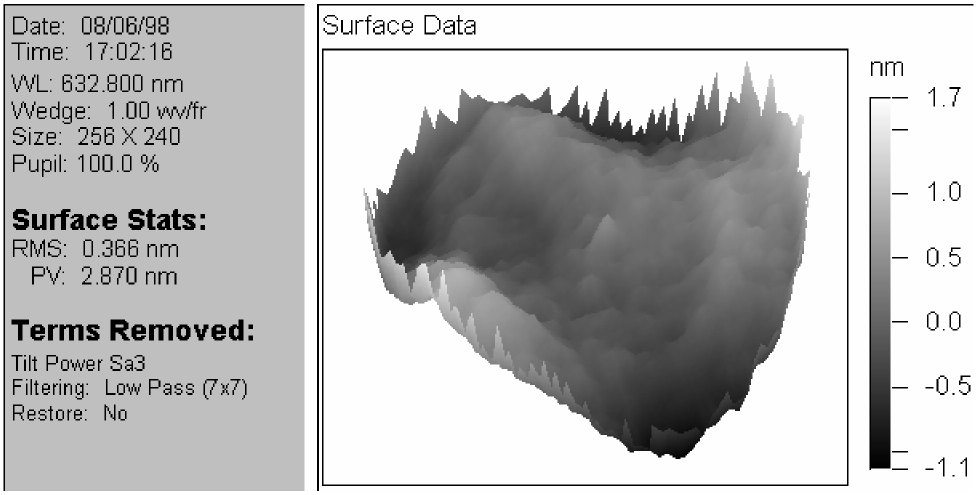

Date: 08/06/98
Time: 17:02:16
WL: 632.800 nm
Wedge: 1.00 wv/fr
Size: 256 X 240
Pupil: 100.0 %

Surface Stats:
RMS: 0.366 nm
PV: 2.870 nm

Terms Removed:
Tilt Power Sa3
Filtering: Low Pass (7x7)
Restore: No

Figure 7.14. 3-D plot of the final wavefront phase difference map.

Computer simulation results from the earlier section predicted a 2-fold symmetry of the phase difference function between the TE and the TM polarization fields. A peak-to-valley phase difference of 0.024λ was expected. Our experimental data show, on the other hand, a peak-to-valley phase difference of 2.87 nm or 0.005λ. The measured RMS wavefront phase difference is only 0.0006λ. Despite the differences in the phase values, the basic saddle shape of the phase difference function predicted by the computer model is noticed from the experimental result. The differences between the experimental data and the computer simulation results are likely due to the hologram manufacture errors. Due to the limited resource, we didn’t verify the precision of the hologram. This should be included in the future work.

In conclusion, our study shows that CGHs with wavelength-scaled diffraction features are sensitivity to the state of polarization changes of the incident wavefront. This polarization sensitivity is not modeled by the scalar diffraction theory. Rigorous diffraction analysis must be applied in order to accurately determine the diffraction wavefront functions produced by such holograms. However, our measurements show less than $\lambda/200$ PV and $\lambda/1600$ RMS phase deviations in the diffraction wavefront when the polarization direction of the incident beam was varied from TE to TM model. This result indicates that the effects of polarization changes in the incident beam on diffraction wavefront phase values are negligible when the minimum diffraction structure size is greater than 2 waves. Scalar diffraction theory is sufficient for CGH analysis under such circumstance.

CHAPTER 8

DISCUSSIONS AND CONCLUSIONS

In this dissertation, we have studied both design and fabrication issues for CGHs. The binary linear grating model was introduced to study wavefront phase and efficiency sensitivities to duty-cycle and groove depth variations due to CGH fabrication uncertainties. To validate the diffraction model, experimental studies for both phase and chrome-on-glass CGHs were conducted. The diffracted wavefronts generated by these samples were measured using a phase shifting interferometer. The experimental results were then compared with the theoretical models. In general, good agreements between the experimental and the theoretical data were obtained. The results of our experiments demonstrated the effects of CGH fabrication errors on diffraction wavefront phase and amplitude functions for both phase and chrome-on-glass holograms.

Examples of CGH errors analysis for optical testing were provided in this dissertation. The examples showed how to estimate CGH errors from fabrication tolerance and uncertainties using the wavefront sensitivity functions presented. Using the wavefront sensitivity functions, we were able to identify hologram structures that are the most sensitive, as well as, the least sensitive to fabrication uncertainties. This information may also be used to direct CGH designs that will reduce or eliminate effects from fabrication errors. This information is extremely valuable to the design and fabrication practices for computer-generated holograms.

The graphical presentation of diffraction fields was also introduced in this dissertation. This complex field representation provides an intuitive view of the diffraction wavefront function. Both diffraction efficiency and wavefront phase functions may be retrieved from the plot easily. The plot also shows changes in wavefront functions as result of variations in grating duty-cycle and groove depth. Using the complex field plot, we were able to explain the observed anomalous phase discontinuities.

A discussion on the design and the modeling of CGH was also given in this dissertation. Both scalar and rigorous models were studied. Fourier modal method derived from the rigorous diffraction model was used to analyze a zone plate hologram with a minimum fringe spacing of 0.6 λ. A chrome-on-glass sample zone plate was fabricated and measured using a phase-shifting interferometer. The experimental data were compared against the theoretical model. The results from experimental measurement showed that polarization sensitivities of the hologram were almost negligible for the chrome-on-glass zone plate sample with a minimum ring spacing of 2λ. A peak-to-valley phase difference of 0.005λ between the TE and the TM polarization wavefronts was observed for the sample zone plate. This conclusion implies that the scalar diffraction model may be sufficient for modeling holograms with wavelength-scaled diffraction features for the case studied in this dissertation.

It is technically challenging to control the chrome layer thickness of a chrome-on-glass grating. Our limited resources prevented us from obtaining grating samples with various chrome thickness. Although analytical studies of wavefront sensitivities to hologram phase depth variations for chrome-on-glass gratings were provided, no grating samples were made and measured to verify the theoretical results. This analysis should be included as part of future study on this topic.

During our study, we also observed disagreements among the measured phase value for the chrome-on-glass grating sample. Phase values obtained from the Fizeau interferometer differed from the values obtained from the microscope interferometer and the calculation using the chrome thickness and the index of refraction of the chrome coating (see Section 4.2.3). This discrepancy is not understood or explained and requires further investigation as part of a future study. In addition, a large number of CGH substrate errors were seen on our sample holograms. The sample grating substrates were not certified before the hologram patterns were applied. These substrate errors produced wavefront aberrations that interfered with the diffraction wavefront functions produced by the diffraction gratings. As a result, the sensitivities of our wavefront phase measurements were compromised. We suggest a pre-measurement of the hologram substrate before the grating pattern is written. The measured substrate figure errors can then be eliminated from the measured diffraction wavefront functions in future experiments.

In conclusion, this research work provides a thorough analysis of both the fabrication and modeling aspects of computer-generated holograms. The results of our studies have been proven both theoretically and experimentally. The wavefront sensitivity analysis provides insights of CGH fabrication errors; it becomes a powerful tool for CGH error analysis and error budgeting. The graphical representation of diffraction fields gives an intuitive view of diffraction wavefronts. Our conclusion from the studies on CGH modeling methods validates broader implementations of the scalar diffraction models in practical applications.

REFERENCES

Arnold, S. M., “How to test an asphere with a computer generated hologram,” Proc. SPIE, **1052**, 191-197 (1989).

Baber, S. C., “Application of high resolution laser writers to computer generated holograms and binary diffractive optics,” Proc. SPIE, **1052**, 66-76 (1989).

Bartelt, H. O. and K. D. Forster, “Computer generated holograms with reduced phase errors,” Opt. Commun., **26**, 12-16, (1978).

Bowen, J. P., R. L. Michaels, and C. G. Blough, “Generation of large-diameter diffractive elements with laser pattern generation,” Appl. Opt., **36**, 8970-8975 (1997).

Born, M. and E. Wolf, *Principles of Optics 6th Edition*, Cambridge University Press, N.Y., 1980.

Brewer, G. R., *Electron-Beam Technology in Microelectronic Fabrication*, Academic Press, N.Y., 1980.

Brown, B. R. and A. W. Lohmann, “Complex spatial filtering with binary masks,” Appl. Opt., **5**, 967-969 (1966).

Brown, B. R. and A. W. Lohmann, “Computer-generated binary images,” IBM J. Res. Development, **13,** 160-168 (1969).

Bryngdahl, O. and F. Wyrowski, “Digital holography-computer-generated holograms,” in *Progress in Optics* **XXVIII**, E. Wolf, ed, (Elsevier Science Publishers, B.V. 1990), pp.1-86

Burckhardt, C. B., “A simplification of Lee’s method of generating holograms by computer,” Appl. Opt., **9**, 1949 (1970).

Burge, J. H., “Advanced techniques for measuring primary mirrors for astronomical telescopes,” Ph.D. dissertation, Optical Sciences Center, University of Arizona, 1993.

REFERENCES-*Continue*d

Burge, J. H., “Applications of computer-generated holograms for interferometric measurement of large aspheric optics,” Proc. SPIE, **2576**, 258-269 (1995).

Creath, K. and J. C. Wyant, “Holographic and speckle tests,” in *Optical Shop Testing 2nd Edition,* D. Malacara, ed (John Wiley & Sons, Inc., N.Y. 1992), pp.599-651.

Creath, K. and J. C. Wyant, “Moir■ and fringe projection techniques,” in *Optical Shop Testing 2nd Edition,* D. Malacara, ed (John Wiley & Sons, Inc., N.Y. 1992), pp.653-685.

Elliott, D. J., *Integrated Circuit Fabrication Technology 2nd Ed.*, McGraw-Hill, Inc., N.Y., 1989.

Fercher, A. F., “Computer-generated holograms for testing optical elements: error analysis and error compensation,” Opitca Acta, **23**, 347-365 (1976).

Gaskill, J., *Linear System, Fourier Transforms, and Optics*, John Wiley & Son, Inc., N.Y., 1978.

Goodman, J. W., *Introduction to Fourier Optics 2nd Ed.*, McGraw-Hill, Inc., N.Y., 1996.

Haruna, M., M. Takahash, K. Wakahayashi, and H. Nishihara, “Laser beam lithographed micro-Fresnel lenses,” Appl. Opt., **29**, 5120-5126 (1990).

Hecht, E., *Optics 2nd Edition*, Addison-Wesley, Inc., M.A., 1987.

Herzig, H. P., *Micro-Optics: Elements, Systems and Applications,* Taylor & Francis Ltd 1997.

Hessler, T., “Continuous-Relief Diffractive Optical Elements: *Design, Fabrication and Applications,”* Ph.D. thesis, Institut de Microtechnique, Universit■ de Neuch•tel, 1997.

Hsueh, C. K. and A. A. Sawchuck, “Computer generated double phase holograms,” Appl. Opt., **17**, 3874 (1978).

Hugonin, J. P. and P. Chavel, “A compement to the theory of Lohmann-type computer holograms,” Opt. Commun., **16**, 342-346 (1976).

Huntley, M. C., *Diffraction Gratings*, Academic, New York, 1982.

REFERENCES-*Continued*

Lee, W. H., “Sampled Fourier transform holograms generated by computer,” App. Opt., **9**, 639 (1970).

Lee, W. H., “Binary synthetic holograms,” Appl. Opt., **13**, 1677-1682 (1974).

Lee, W. H., “Computer-generated Hologram: Techniques and applications,” in *Progress in Optics*, **XVI**, E. Wolf, ed, (North-Holland, Amsterdam, 1978), pp.121-232.

Lee, W. H., “Binary computer-generated holograms,” Appl. Opt., **18**, 3661-3669 (1979).

Li, Lifeng, “Application of the method of reduction in the Fourier modal method,” Diffractive Optics and Micro-optics 1998 technical digest series vol 10, 1998 OSA

Li, Lifeng, “*KAPPA*,” computer code for rigorous diffraction analysis, Optical Sciences Center, University of Arizona, 1998.

Li, L, “Use of Fourier series in the analysis of discontinuous periodic structures,” J. Opt. Soc. Am. A, **13**, 1870-1876 (1996).

Lohmann, A.W. and D. P. Paris, “Binary Fraunhofer holograms, generated by computer,” Appl. Opt., **6**, 1739-1748 (1967).

Loomis, J. S., “Applications of computer-generated holograms in optical testing,” Ph.D. dissertation, Optical Sciences Center, University of Arizona, 1980.

Lynch, D. W. and W. R. Hunter, “An introduction to the data for several metals,” in *Handbook Of Optical Constants Of Solids II*, Z. D. Palik, ed (Academic Press, San Diego, 1991), pp.341-419.

MacGovern, A. J. and J. C. Wyant, “Computer generated holograms for testing optical elements,” Appl. Opt., **10**, 619-624 (1971).

Mayster, D., “Rigorous vector theories of diffraction grating,” in *Progress in Optics*, **XXI**, E. Wolf, ed (North-Holland, Amsterdam, 1984), pp.1-67.

Moharam, M. G. and T. K. Gaylord, “Rigorous coupled-wave analysis of metallic surface-relief grating,” J. Opt. Soc. Am. A, **3**, 1780-1787 (1986).

REFERENCES-*Continued*

Noponen, E. and J. Saarinen, “Rigorous synthesis of diffractive optical elements,” Proc. SPIE, **2689**, 54-65 (1996).

Offner, A., and D. Malacara, “Null tests using compensators,” in *Optical Shop Testing* 2nd edition, D. Malacara, ed, (John Wiley & Sons, Inc. 1992), pp.427-454

Ono, A. and J. C. Wyant, “Plotting errors measurement of CGH using an improved interferometric method,” Appl. Opt., **23**, 3905-3910 (1984).

Peng, S. T., T. Tamir, and H. L. Bertoni, “Theory of periodic dielectric waveguides,” IEEE Trans. Microwave Theory Tech., **23**, 123-133 (1975).

Peterson, T., ‘Atomic force microscope’ measurement, Optical Sciences Center, University of Arizona, 1999.

Petit, R., *Electromagnetic Theory of Gratings*, Springer-Verlag, Berlin, 1980.

Sheng, Y., D. Feng, and S. Larochelle, “Analysis and synthesis of circular diffractive lens with local linear grating model and rigorous coupled-wave theory,” J. Opt. Soc. Am. A, **14**, 1562-1568 (1997).

Tricoles, G., “Computer generated holograms: an historical review,” Appl. Opt., **26**, 4351-4360 (1987).